

FINAL TECHNICAL REPORT

For research supported by
AFOSR Contract No. F49620-95-1-0331
for period 4/15/95 to 9/30/97

SPACECRAFT INTERACTIONS STUDIES WITH A 1 KW CLASS CLOSED-DRIFT HALL THRUSTER

Prepared by

Alec D. Gallimore⁽¹⁾, Brian E. Gilchrist⁽²⁾,
Lyon B. King⁽³⁾, and Shawn G. Ohler⁽⁴⁾

Department of Aerospace Engineering
Department of Electrical Engineering and Computer Science
University of Michigan
Ann Arbor, MI 48109

Work Supported by

Air Force Office of Scientific Research
Program Monitor: Dr. Mitat Birkan

19980430 108

⁽¹⁾ Assistant Professor, Co-Principal Investigator, Department of Aerospace Engineering

⁽²⁾ Associate Professor, Co-Principal Investigator, Department of Electrical Engineering and Computer Science

⁽³⁾ Graduate Research Assistant, Department of Aerospace Engineering

⁽⁴⁾ Graduate Research Assistant, Department of Electrical Engineering and Computer Science

APPROVED FOR PUBLIC RELEASE; DISTRIBUTION UNLIMITED

January 1998

DTIC QUALITY INSPECTED 3

REPORT DOCUMENTATION PAGE

FORM APPROVED
OMB No. 0704-0188

Public reporting burden for this collection of information is estimated to average 1 hour per response, including the time for reviewing instructions, searching existing data sources, gathering and maintaining the data needed and completing and reviewing the collection of information. Send comments regarding this burden estimate or any other aspect of the collection of information, including suggestions for reducing the burden to: Washington Headquarters Services, Directorate for Information Operations and Reports, 1215 Jefferson Davis highway, Suite 1204, Arlington, VA 22202-4302 and to the Office of Management and Budget, Paperwork Reduction Project (0704-0188), Washington, DC 20503

1. AGENCY USE ONLY (Leave Blank)		Report Date: January 31, 1998	3. REPORT TYPE AND DATES COVERED Final Technical Report 4/15/95-9/30/97	
4. TITLE AND SUBTITLE OF REPORT Spacecraft Interaction Studies with a 1 KW Class Closed-Drift Hall Thruster			5. FUNDING NUMBERS AFOSR; F49620-95-1-0331	
6. AUTHOR(S) A. Gallimore, B. Gilchrist, L. King, and S. Ohler				
7. PERFORMING ORGANIZATION NAME(S) AND ADDRESS(ES) University of Michigan Attn: Dr. Neil Gerl DRDA, 3003 South State Street Wolverine Towers, Room 1053 Ann Arbor MI 48109-1274			8. PERFORMING ORGANIZATION REPORT NUMBER	
9. SPONSORING/MONITORING AGENCY NAME(S) AND ADDRESS(ES) AFOSR/NA 110 Duncan Avenue; Suite B115 Bolling AFB, DC 20332-0001			10. SPONSORING/MONITORING ORGANIZATION REPORT NUMBER	
11. SUPPLEMENTARY NOTES:				
12a. DISTRIBUTION AVAILABILITY STATEMENT Approved for Public Release; Distribution Unlimited			12b. DISTRIBUTION CODE	
13. ABSTRACT (Maximum 200 words) This final technical report summarizes work performed at the Plasmadynamics and Electric Propulsion Laboratory (PEPL) to study the interaction of the Closed-Drift Hall thruster plume with spacecraft surfaces and systems. Two basic interaction modes were investigated: 1) the influence of the plume on spacecraft surfaces in terms of erosion, contamination, and heating; and 2) the impact of the plume plasma on communication signals. An extensive spatial mapping of plasma and neutral properties to quantify particle and energy transport properties within the plume was completed (Section I), as well as a broad survey of signal attenuation and phase shift of L- and Ku-band radio signals (Sections II and III). This work culminated with the development of a Molecular Beam Mass Spectrometer (MBMS) capable of discerning both the mass and energy of Hall thruster plume species (Section IV), and the ion acoustic wave probe to measure the drift velocity of the plume plasma (Section V).				
14. SUBJECT TERMS Hall Thruster (Electric) Propulsion; Probe Diagnostics; Plasmadynamics; Microwave; RF Communications			15. NUMBER OF PAGES: 104	
			16. PRICE CODE	
17. SECURITY CLASSIFICATION OF REPORT: UNCLASSIFIED/UNLIMITED	18. SECURITY CLASSIFICATION OF THIS PAGE UNCLASSIFIED	19. SECURITY CLASSIFICATION OF ABSTRACT UNCLASSIFIED	20. LIMITATION OF ABSTRACT NONE	

FINAL TECHNICAL REPORT

For research supported by
AFOSR Contract No. F49620-95-1-0331
for period 4/15/95 to 9/30/97

SPACECRAFT INTERACTIONS STUDIES WITH A 1 KW CLASS CLOSED-DRIFT HALL THRUSTER

Prepared by

Alec D. Gallimore⁽¹⁾, Brian E. Gilchrist⁽²⁾,
Lyon B. King⁽³⁾, and Shawn G. Ohler⁽⁴⁾

Department of Aerospace Engineering
Department of Electrical Engineering and Computer Science
University of Michigan
Ann Arbor, MI 48109

Work Supported by

Air Force Office of Scientific Research
Program Monitor: Dr. Mitat Birkan

-
- ⁽¹⁾ Assistant Professor, Co-Principal Investigator, Department of Aerospace Engineering
⁽²⁾ Associate Professor, Co-Principal Investigator, Department of Electrical Engineering and Computer Science
⁽³⁾ Graduate Research Assistant, Department of Aerospace Engineering
⁽⁴⁾ Graduate Research Assistant, Department of Electrical Engineering and Computer Science

APPROVED FOR PUBLIC RELEASE; DISTRIBUTION UNLIMITED

January 1998

TABLE OF CONTENTS

	<u>Page</u>
Form DD298	i
Abstract	1
Introduction	2
Overview of Format of Report Document	8
Section I	13
Section II	34
Section III	50
Section IV	66
Section V	81

ABSTRACT

While the closed-drift Hall thruster (CDT) offers significant improvement in performance over other electric propulsion (EP) systems such as the arcjet and resistojet, its potential impact on other spacecraft systems must be carefully assessed before widespread implementation of it can take place. To this end, many of the potentially unique issues that are associated with these thrusters center on their plume characteristics. Possible impacts include momentum losses due to plume impingement upon spacecraft systems; thermal loading of spacecraft surfaces; induced environmental effects on electrical, communications, and navigation systems; and possibly electromagnetic contamination due to radiated or near-field plume emissions.

With this in mind, a proposal for an experimental program to access the potential of CDTs to interfere adversely with earth-orbiting spacecraft operations and communications was presented to the Air Force Offices of Scientific Research (AFOSR). We proposed to make careful CDT plume plasma parameter measurements and to assess their impact on communication and navigation systems by making electromagnetic interactions measurements. This study was deemed necessary to enable CDTs to be used on future Air Force spacecraft for station-keeping, orbit repositioning, and orbit raising.

The program utilized the experimental facilities at the University of Michigan's Plasmadynamics and Electric Propulsion Laboratory (PEPL), the centerpiece of which is a 9-m-long by 6-m-diameter diffusion pumped vacuum chamber that is the largest tank devoted solely to propulsion research at any university in the country.

The main features of the proposed effort are:

- To use a variety of probe diagnostics throughout the CDT plume to measure plasma properties, ion energy distribution, current density, plasma potential, pressure, and heat flux; and
- To use a modern microwave propagation system to characterize the influence that the thruster plume has on communication signals.
- To collaborate with and provide plume plasma transport parameters to plume modelers such as Professor Daniel Hastings of MIT.

This work represents a three year multidisciplinary effort that included two students and two professors, one pair each, from the University of Michigan's Aerospace Engineering, and Electrical Engineering and Computer Science Departments.

In addition to the knowledge obtained from fundamental research, an important outcome of this effort was expected to be the development of diagnostic tools/capabilities that can afford an impact assessment of EP devices on spacecraft systems. Early assessment of system impact is critical to achieving acceptance of new EP technologies and to efficiently direct development efforts.

INTRODUCTION

Propulsion systems having high exhaust velocities ($I_{sp} > 1000$ seconds) are desirable for a variety of space missions. In order for a propulsive system not to require an inordinate amount of propellant, its exhaust velocity should be of the same order as the characteristic velocity increment (ΔV) required for a given space mission. Studies have shown that for orbit transfer missions of interest by NASA and the DOD, a characteristic velocity increment of over six kilometers per second may be necessary[1]. Furthermore, experience gleaned from operation Desert Storm shows the need for military space assets to be rapidly repositioned without excessive use of onboard propellant.

Cryogenically fueled chemical rockets which rely on the intrinsic energy available from the chemical reactions of their constituent propellants are inherently limited to specific impulses of 500 seconds. Chemical rockets which use space-storable fuels such as hydrazine with nitrogen tetroxide are limited to specific impulses of 300 seconds. Thus, propulsion systems which produce specific impulses considerably higher than those obtained with chemical systems would benefit a variety of orbital space missions.

Ideally, an engine which would be used as the primary source of propulsion for satellite station-keeping and orbit repositioning in modern spacecraft should have an I_{sp} between 1000 and 2500 seconds[2]. To achieve this performance, a propulsion system must accelerate its propellant gas without relying on energy addition through chemical reactions. One approach is the application of electrical energy to a gas stream in the form of electrical heating and/or electric and magnetic body forces. This type of propulsion system is commonly known as electric propulsion.

Electric propulsion can be categorized into three groups[3]:

1. Electrothermal Propulsion Systems in which a gas is electrically heated, either with resistive elements or through the use of an electric arc, and is subsequently expanding through a supersonic nozzle to produce thrust;
2. Electromagnetic Propulsion Systems which use electromagnetic body forces to accelerate a highly ionized plasma; and
3. Electrostatic Propulsion Systems which use electrostatic forces to accelerate ions.

In addition to possessing suitable exhaust velocity, an electric propulsion system must also be able to convert onboard spacecraft power into directed kinetic power of the exhaust stream efficiently (i.e., possess high thrust efficiency) and must generate suitable thrust to ensure reasonably short deployment times.

Electrothermal systems have limited utility for this role because of performance constraints placed on them by excessive frozen flow and electrode losses[4-6]. The specific impulse and thrust efficiency of arcjets operating on space-storable propellants is limited to less than 700 seconds and 41%, respectively. Steady-state electromagnetic systems have demonstrated high thrust efficiencies only at power levels that far exceed those generated onboard current spacecraft[7-8]. However, researchers at the NASA Lewis Research Center (LeRC) and the University of Michigan have been evaluating pulsed magnetoplasmadynamic (MPD) thrusters as a means of propelling orbit transfer vehicles with moderate solar power supplies (10 kW).

Gridded electrostatic (ion) engines, which can achieve large specific impulses (>5000 seconds) at high thrust efficiencies ($>65\%$), have traditionally demonstrated efficient performance at exhaust velocities above 3000 m/s[2,9,10]; beyond the desired range for orbit transfer missions. The high specific impulse of the ion thruster means that for a given spacecraft power level, it will generate less thrust than a lower Isp counterpart, resulting in larger trip times. Furthermore, ion engines pay a penalty for its high power processing specific mass due to its large operating voltages (e.g., 1200 V) and are limited in thrust density by space-charge effects[2].

Therefore, the ideal propulsion system for orbit transfer missions and for satellite station-keeping is one that efficiently accelerates propellant (e.g., through electrostatic means) to modest exhaust velocities while requiring discharge voltages of less than 1000 V. As is shown below, the Hall thruster is a device which fulfills these requirements.

THE HALL THRUSTER

The Hall thruster is an electrostatic engine that was developed in the 1960's to alleviate the thrust density limitation of ion engines that results from space-charge effects within the acceleration volume between grids. Hall thrusters were also attractive from the standpoint that since grids are not required to accelerate ions, they do not suffer from the large grid erosion rates of the ion engines. Interest in the Hall thruster waned in the early 1970's, however, because of budgetary cuts and because American researchers were never able to demonstrate that these engines could operate at thrust efficiencies near those achieved with ion thrusters[11-13]. As such, Hall thruster research essentially disappeared in the U.S. between 1972 and 1985. From 1985 to 1990, Ford Aerospace (now Space Systems/Loral), in conjunction with NASA, funded a small research effort to determine if Hall thrusters could be used for North-South station-keeping (NSSK)[14]. This program proved to be unsuccessful and was abandoned.

Throughout this period, however, Hall thruster research flourished in the Soviet Union. Hall thrusters were first tested in space in 1971 with immediate success[15,16]. Since then, over fifty Hall thrusters are claimed to have been used onboard Soviet spacecraft, mostly as plasma contactors and for East-West station-keeping. Because of experiments which show that Russian Hall thrusters are capable of generating specific impulses of 1650 seconds at thrust efficiencies of 50% [17,18], there has been a great deal of interest in using them on American spacecraft for NSSK and for orbit repositioning. Clearly this device, with performance far superior to that of arcjets, which is the most advanced propulsion system currently in use on American spacecraft, would not only serve as an excellent thruster for orbit station-keeping and repositioning roles, but potentially could be scaled in power to propel orbit transfer vehicles and future planetary probes.

THE CLOSED-DRIFT HALL THRUSTER

There are two types of Hall thrusters that have been studied at great lengths, the end-Hall thruster and the closed-drift thruster (CDT). Both engines, in principle, are capable of producing specific impulses in excess of 1500 seconds with xenon at a thrust efficiency of approximately 50% . However, it is the CDT, which has been developed and used in the former Soviet Union over the past twenty years, that is of the most interest to the Western space technology community.

The CDT is a coaxial device in which a magnetic field that is produced by an electromagnet is channeled between an inner ferromagnetic core (pole piece) and outer ferromagnetic

ring. This configuration results in an essentially radial magnetic field with a peak strength of a few hundred gauss. This field strength is such that only the electrons are magnetized. In addition, an axial electric field is provided by applying a voltage between the anode and the downstream cathode. As the electrons stream upstream from the cathode to the anode, the \mathbf{ExB} action on the electrons causes them to drift in the azimuthal direction, forming a Hall current. Through collisions, these electrons ionize propellant molecules which are injected through the anode and that are subsequently accelerated by the axial electric field. The mixture of electrons and ions in the acceleration zone means that the plasma is electrically neutral, and as such, is not space charge limited in ion current (thrust) density. Since the magnetic field suppresses the axial mobility of the electrons while exerting essentially no effect on the ion dynamics, the plasma can support an axial electric field with a potential difference close to the applied voltage between the electrodes. Thus, the bulk of the ions are accelerated to kinetic energies to within 80% of the applied discharge voltage. This combination of processes accounts for the CDT's high thrust efficiency.

Russian CDTs come in two variants; the stationary plasma thruster (SPT) (also known as the magnet layer thruster) such as the SPT-100 and the thruster with anode layer (TAL) such as the D55. The main difference between these two devices is that the SPT uses a dielectric coating to electrically insulate its acceleration channel while the TAL uses a much shallower channel enclosed within metal walls. Performance characteristics of both engines are virtually identical. Although they vary in size and input power (e.g., 7-cm-in-diameter at 660 W to 20-cm-in-diameter at 6 kW), CDTs that are currently being considered for satellite NSSK, LEO satellite orbit transfer, and end-of-life disposal roles typically operate at discharge voltages of 300 - 400 V, thruster currents of 3 - 6 A, and xenon mass flow rates of 4 - 7 mg/s.

Even though CDTs have characteristics that make them ideal for orbit repositioning and orbit transfer applications, these devices have specific problems which make the integration of them with spacecraft a challenge. It was understood at the time that before CDTs were to be used in the West, these problems would have to be addressed. This was the primary motivation for this work.

MOTIVATION FOR RESEARCH

Although CDTs have performance characteristics that make them attractive for earth orbiting missions, the complex nature of their operation is a source of concern from a spacecraft integration point-of-view. For example, CDTs that use dielectric channel coatings suffer from excessive insulator erosion. Much of this erosion is due to sputtering from energetic ions near the exit of the discharge chamber[19]. Such erosion poses a potential hazard to spacecraft operation since ablated insulated material could coat vital spacecraft surfaces like solar arrays and communications antennas.

In addition, there is further concern that the spacecraft could be damaged by side or back-scattered exhaust ions. The ions accelerated by the thruster travel at kinetic energies in excess of 200 eV[20]. Since a significant fraction of the exhausted particles travel at angles in excess of 45 degrees from the thruster axis, plume divergence not only detracts from engine performance due to cosine losses, but also results in damage to the spacecraft due to sputtering.

The erosion/deposition characteristics in the plume of CDTs are quite complex. Experiments have shown that in the central region (<45 degrees) of the plume, the energetic ions tend to remove deposited materials from structures in such a way that the net erosion rate overwhelms the surface deposition rate of thruster effluent material[21]. At higher angles with respect to the thruster axis of symmetry, however, the opposite is true: That is,

the plume tends to remove material from objects placed near its axis of symmetry, and deposits matter on objects at higher angles. The exact location where this transition occurs (and what parameters it may depend on) remains unknown.

Furthermore, the exhaust of a highly ionized plasma from a spacecraft in low earth orbit may affect the electrodynamics of the spacecraft and its communication systems. Russian researchers have claimed that the operation of the engine yields "subtle changes" of the spacecraft's potential with respect to the ambient plasma[15]. This phenomenon may affect the electronics of the satellite by causing excessive spacecraft charging or coupling of plasma noise into the spacecraft structure[22]. This is of particular concern to developers of LEO satellite constellations (e.g., Teledesic) who may wish to use CDTs for a variety of roles.

There is also concern that the highly ionized plume might interfere with the transmission of radio waves. The impact of thruster plasma plumes on electromagnetic signals in the near-field of onboard antennas and receiving systems is of concern to spacecraft designers. Air Force spacecraft radio frequency (RF) systems can include: communications, radar, surveillance, and navigation (Global Positioning System). The spacecraft designer must know whether these RF systems will be degraded and whether the impact of compensating for the degradation outweighs electric propulsion's inherent advantages. Typical radio wave-plasma interactions of concern include: reflection or refraction of a transmitted/received signal, attenuation and phase shift (scintillation), and generated noise on both signal amplitude and phase. Possible system impacts include: signal-to-noise degradation (amplitude degradation, phase noise), degradation of the antenna main beam and side lobe, and reduced cross polarization isolation (linearly polarized systems only). This could result in increased bit-error-rates (BER) for communication systems, degraded radar images/signatures for radar systems, higher threshold for surveillance systems, and increased range and location errors for RF navigation systems.

Studies to-date of low to moderate power arcjets (1 - 2 kW) have generally concluded that minimal impact to communication systems is expected [23-25]. This conclusion, however, although somewhat intuitive for the weakly ionized low-power arcjet plumes with relatively low plasma densities and collision frequencies, cannot be generalized to higher power arcjets or CDT systems. Electron number densities associated with CDTs are at least one order of magnitude higher than arcjets of comparable power[20,25] achieving levels on the order of 10^{17} m^{-3} at 0.3 m from the thruster and 10^{14} m^{-3} out to 2-4 m. This corresponds to plasma frequencies of 2.8 GHz and 90 MHz, respectively. Above the plasma frequency the plasma mostly appears like a low-loss dielectric while below the plasma frequency the plasma plume is totally reflecting. Although several military space frequency bands are above these plasma frequencies, some space based radar bands and the Global Positioning System (GPS) navigation signals are in the 1 to 2 GHz range and thus are highly susceptible to the thruster plume plasma. Knowledge of the far-field plasma distribution is therefore critical to proper spacecraft systems design. In addition, it is possible for signals operating above the plume plasma frequency to suffer degradation due to scintillation effects, or density irregularities in the plume[26]. Thus, critical for understanding the potential impact to spacecraft RF systems will be a full spatial characterization of the CDT plume plasma.

PROPOSED RESEARCH PROGRAM

This research represents an attempt to combine experienced researchers in the field of electric propulsion and RF systems in an experimental program using state-of-the-art diagnostics in a world-class vacuum facility. The research program was composed of two

principal activities: i) a detailed survey of plume plasma and transport properties in the far-field of the thruster; and ii) a detailed assessment of the impact thruster operation may have on RF signals for spacecraft communications, radar, surveillance, and navigation systems. All measurements were performed on a 1.5-kW-class CDT with xenon as propellant.

PLUME CHARACTERIZATION

The focus of these measurements was to investigate the local plasma properties of these engines to try to gain a better understanding of the local plasma environment for future spacecraft integration activities. The following experiments were performed to characterize the plume of CDTs, many of which were also performed on arcjets and end-Hall thruster plumes[27-29]. To characterize the plume we:

1. Used Langmuir probes to measure electron temperatures, electron and ion number densities, and plasma potentials. This information is needed for theoretical and experimental electromagnetic interference (EMI) and RF systems impact assessment studies.
2. Used emissive probe measurements to map the plasma potentials throughout the plume. This information was used in plume modeling activities.
3. Used water-cooled enthalpy probes to measure heat flux at various locations within the plume. This study determined the potential of the plume to heat spacecraft structures and was used in characterizing energy transport throughout the plume.
4. Used a microwave interferometer to measure electron number density. Since microwave interferometry is the standard means of measuring the electron number density, against which other techniques are compared, these experiments represented the most accurate CDT plasma density measurements to date.
5. Used Faraday cups to measure ion current density through the plume, particularly at high flow angles. This information is of interest from a general spacecraft integration point of view since CDT plume properties data at high angles (>80 degrees) is lacking.
6. Used a retarding potential energy analyzer (RPA) to measure ion energy distribution. This information is crucial for developing accurate surface erosion models since material sputtering yields are energy-dependent.
7. Used free molecular probes (FMP) and impact pressure probes to measure the stagnation pressure throughout the plume. These data were useful in estimating the forces that other spacecraft components (e.g., solar arrays) may experience due to plume impact. These forces, if not accounted for, could impart unwanted torques to the spacecraft which could result in additional (and unanticipated) propellant use.
8. Used various emission spectroscopic techniques to measure electron temperatures and qualitatively identify species throughout the plume.
9. Developed and used a Molecular Beam Mass Spectrometer (MBMS) to identify, and determine the density and energy distribution of a variety of species in the CDT plume.

RF SIGNALS IMPACT STUDIES

The goals for this aspect of our research were to characterize the local plasma environment of these engines for their potential impact on RF signals for communication, radar, and navigation systems. It was expected that this information would be used to help address future integration activities of spacecraft RF systems.

We planned on performing the following experiments based primarily on the proven microwave interferometric system developed by us to make highly accurate plasma density measurements[29]. The design of this interferometer, using a network analyzer with up/down frequency conversion, is highly flexible and cost effective for covering a broad frequency range. With straight forward modifications to the up/down converter circuit and antennas it is possible to conduct measurements from below 1 GHz up to at least 35 GHz. We selected L- (1.6 GHz) and Ku-band (17 GHz) for conducting the following detailed measurements.

1. RF signal induced phase shift as a function of location and angle in the thruster plume. This is a direct measure of the plume impact on the signal and its potential for scattering electromagnetic waves as well as range or group delays of importance to radio navigation systems. Details of the response will depend both on plasma density levels and their gradients.
2. RF signal attenuation as a function of location. Line-of-sight signal attenuation will become significant for signals near the plasma frequency of the local plasma primarily due to scattering.
3. Induced phase noise (scintillation) on RF signals. Time varying inhomogeneities in the plasma plume can result in phase and amplitude variations (scintillation), Doppler frequency fluctuations, spectral broadening, and angular broadening. A measure of induced phase noise in the plume provides a direct measure of the extent of impact on phase sensitive systems.
4. Antenna pattern modification. It has been noted by others that a likely impact due to thruster plumes is some level of refraction or modification of antenna main and side lobes[23,25]. Because the metal surfaces of the vacuum chamber can create unwanted artificial reflections, measurements were based primarily on comparison between responses with and without the plasma plume.

VACUUM FACILITIES

All experimental work was performed at the Plasmadynamics and Electric Propulsion Laboratory (PEPL). The cornerstone of this laboratory is the Michigan Large Chamber Plasma Facility (MLCPF). The MLCPF is a large oil diffusion-pumped vacuum chamber (9-m-long by 6-m-diameter) with a pumping speed of 27,000 l/s on xenon. The chamber has recently been upgraded with cryopumps to achieve a xenon pumping speed of 140,000 l/s.

The large size of this chamber allows us to make these measurements within an extensive volume of the plume that spans from a few millimeters to more than 7 meters from the thruster exit plane. Because of the flexibility of our test facility, we were also able to make many of these measurements at extreme angles with respect to the thruster axis. These capabilities enabled us to make among the most comprehensive characterizations of the CDT plume ever.

THRUSTER SOURCES

Only a handful of Russian CDTs such as the SPT-100 and the D55 are available in the United States and all of them are in great demand. By far, the largest purchaser of CDTs up to now has been the Ballistic Missile Defense Organization (BMDO), which contracts NASA LeRC and the Jet Propulsion Laboratory (JPL) to test them. In addition, Space System/Loral (SS/L) has purchased several SPT-100s for use in developing a flight-qualified PPU, and Teledesic, Inc. will issue a contract to purchase more than 1000 CDTs.

Most of our measurements were taken with the FAKEL SPT-100, a laboratory SPT developed by the Moscow Aviation Institute (MAI) that is roughly equivalent to the FAKEL SPT-100, and the TsNIIMASH D55 TAL. Most of the results presented below were taken with the SPT-100.

COLLABORATION WITH COMPUTER CODE DEVELOPERS

In order to obtain a better understanding of CDT plume physics, careful experimentation coupled with sophisticated numerical modeling would be highly beneficial. To this end, our activities included collaborating with a group of researchers at MIT, headed by Professor Daniel Hastings, who are developing a 3-D particle-in-cell (PIC)/direct-simulation Monte Carlo (DSMC) code to model the plume of CDTs. Specifically, we provided plume parameters (e.g., current density and ion energy distribution) for them to incorporate into their codes. They then used this code to model the expansion process of low-energy charge-exchange ions and contaminants and to study the interaction of these particles with dielectric surfaces in free space.

OVERVIEW OF FORMAT OF REPORT DOCUMENT

The remaining sections of this report contain stand-alone documents which highlight key contributions of our work. Section I presents our work in measuring transport properties in the plume of the SPT-100. Section II highlights work done to measure the impact the plasma plumes of the SPT-100 and the MAI SPT have on communication signals. Section III presents microwave interferometry data taken with the SPT-100 and the MAI SPT. Section IV describes our efforts to develop a molecular beam mass spectrometer to characterize the plume of the D55 thruster. Section V describes the ion acoustic wave technique for measuring ion drift velocities in the plume of the SPT-100.

SECTION I: TRANSPORT-PROPERTY MEASUREMENTS IN THE PLUME OF AN SPT-100 HALL THRUSTER

Abstract

In order to understand the interaction between the SPT-100 thruster and the spacecraft, accurate knowledge of exhaust plume properties must be obtained. This investigation utilized a suite of inter-related diagnostic probes in an effort to provide detailed knowledge of the exhaust plume on a molecular kinetic level. Probes used for the investigation included a Retarding Potential Analyzer (RPA), a planar Faraday probe, an emissive probe, both total- and radiant-heat-flux probes, as well as a newly developed Neutral Particle Flux probe. Combining knowledge gained from these probes, it was possible to quantify the transport of mass, energy, and charge within the plume at 0.5-m and 1.0-m radius from the thruster exit. Among the phenomena uncovered were a high-energy ionic annulus surrounding a narrow low-energy core within the plume at 0.5-m radius from the thruster exit. This core structure was filled in at 1.0-m radius.

Additionally, a population of energetic charge exchange neutrals was found within 25 deg. of the thruster centerline along with the corresponding low-energy charge exchange ions attributed to plume/background gas interactions.

SECTION II: ELECTROMAGNETIC SIGNAL MODIFICATION IN A LOCALIZED HIGH SPEED PLASMA FLOW: SIMULATIONS AND EXPERIMENTAL VALIDATION OF A STATIONARY PLASMA THRUSTER (SPT)

Abstract

High frequency electromagnetic signals are modified by plasmas primarily through strong density gradients or by densities approaching the critical plasma density. A plasma can potentially degrade an electromagnetic based system through signal attenuation as well as added amplitude or phase noise. This paper reviews the physical mechanism and applies a general ray tracing modeling method to understand the possible phase shift, attenuation, phase modulation, and amplitude modulation produced by the localized, high speed plasma flow of a stationary plasma thruster (SPT). The SPT is currently being tested and considered for use aboard next generation spacecraft where careful consideration must be given to possible interactions with satellite electromagnetic systems such as for communication, navigation, and remote-sensing. The study also models the rather significant plume impact to phase and amplitude for lower frequencies. A summary is provided of ray tracing simulations characterizing both phase and amplitude effects at frequencies from 0.5 to 17 GHz and axial positions from 0.25 m to 1.5 m. The results correlate well with known data.

SECTION III: MICROWAVE PLUME MEASUREMENTS OF A CLOSED DRIFT HALL THRUSTER

Abstract

The plasma plume from a closed drift hall thruster has been characterized using a 17-GHz microwave diagnostic system. Electron number density profiles are obtained throughout the thruster plume via differential phase measurements. A functional model of plasma density has been developed combining a near-field Gaussian beam term and a far-field point source expansion term. An outcome of this work is a mapping of the transition region between the near- and far-field plume. An indication of slight plume asymmetry is obtained by evaluating total integrated density measurements along rays emanating from the thruster. Additional have determined the plasma plume effect on attenuation and spectral characteristics of a wave transmitted through the plume. The attenuation was small, with slightly over 2 dB loss at 0.09 m along the thruster axis. However, ray tracing attenuation modeling based on plasma density profiles indicates a greater effect for lower frequency operation. The spectral data of the signal transmitted through the plume exhibited clear 26-kHz harmonic sidebands and added broadband noise. Estimates of potential impact to communication and other electromagnetic satellite systems can be obtained directly from the measurements and from the electron number density distribution models derived from the measurements.

SECTION IV: A MOLECULAR BEAM MASS SPECTROMETER FOR HALL THRUSTER PLUME STUDIES

Abstract

To assess the interaction due to the direct impingement of the ions on spacecraft surfaces it is necessary to accurately quantify the ionic transport properties as a function of spatial coordinates around the thruster. These data can be combined with surface interaction models to predict surface erosion, contamination, and heating rates. Previous studies have used probe-based techniques to obtain the transport of mass, energy, and charge on a global (species-independent) scale within an extensive volume of the plume. This paper

presents preliminary data from an effort to further improve the probe-based quantities by extending the data to species-dependent measurements of transport properties. The construction of the Molecular Beam Mass Spectrometer (MBMS) reported herein was motivated by the shortcomings discovered in the previous probe-based techniques. The probe data has proven very useful, however, like any diagnostic technique they are subject to limitations. Although the MBMS system is subject to its own inherent imperfections, these limitations are different from and complimentary to the probe-based techniques.

SECTION V: PROPAGATION CHARACTERISTICS OF AN ION ACOUSTIC WAVE IN A FLOWING PLASMA

Shawn G. Ohler, Brian E. Gilchrist, Alec D. Gallimore
University of Michigan, Ann Arbor, MI

Abstract

Ion acoustic wave propagation is characterized for excitation by a cylindrical wire probe in a flowing. The characterization provides the understanding necessary to develop a new diagnostic technique to estimate the flow velocity and the sum of electron and ion temperature. These quantities are important in understanding general plasma physics and specifically for characterizes electric propulsion thrusters. General propagation and excitation characteristics are explored by varying the probe size and stimulus potential in order to determine a reasonable experimental situation. The propagation characteristics are interpreted and compared with previous results which indicate a dependence on the probe wake in addition to the basic ion acoustic wave dispersion relation. The results have potential implication to wave-wake phenomena for spacecraft applications

References

1. Patterson, M. J., Robinson, T. D., Schemmel, T. D., and Burgess, D. R., "Experimental Investigation of a Closed-Drift Thruster," AIAA-85-2060, 18th International Electric Propulsion Conference, Alexandria, Virginia, September 30-October 2, 1985.
2. Deininger, W. D., "Advanced Propulsion System Options for Geostationary Satellites," AIAA-94-3001, 30th Joint Propulsion Conference, Indianapolis, IN, June 27- 29, 1994.
3. Jahn, R. G., **Physics of Electric Propulsion**, McGraw Hill Book Company, NY, 1968.
4. Pivrotto, T., King, D., Deninger, W., and Brophy, J., "The Design and Operating Characteristics of a 30 kW Thermal Arcjet Engine for Space Propulsion," AIAA-86-1508, 22nd Joint Propulsion Conference, Huntsville, Alabama, June 16-18, 1986.
5. Carney, L. M., and Sankovic, J. M., "The Effects of Arcjet Thruster Operating Conditions and Constrictor Geometry on the Plasma Plume," AIAA-89-2723, (NASA TM-102285) 1989.
6. Curran F. M., Bullock, S. R., Haag T. W., Sarmiento, C., and Sankovic J. M., "Medium Power Hydrogen Arcjet Performance," AIAA-91-2343, 27th Joint Propulsion Conference, Sacramento, California, June 24--27, 1991.
7. Gallimore, A. D., Myers, R. M., Kelly, A. J., and Jahn, R. G., "Anode Power Deposition in an Applied-Field Segmented Anode MPD Thruster," Journal of Propulsion and Power (AIAA) Vol. 10, No. 2 March-April, 1994, pp. 262-268.

8. Sovey, J. S., and Mantenieks, M. M., "Performance and Lifetime Assessment of Magnetoplasmadynamic Arc Thruster Technology," J. Propulsion, Vol. 7, No. 1 Jan-Feb, 1991, pp. 71-83.
9. Patterson, M. J., "Performance Characteristics of Ring-Cusp Thrusters with Xenon Propellant," AIAA-86-90, 22nd Joint Propulsion Conference, Huntsville, Alabama, July 16-18, 1986.
10. Aston, G., Brophy, J., Garner, C., and Pless, L., "A Xenon Ion Propulsion Module for Enhanced Spacecraft Capability," AIAA-86-1393 22nd Joint Propulsion Conference, Huntsville, Alabama, July 16-18, 1986.
11. Kaufman, H. R., "Technology of Closed-Drift Thrusters," AIAA-83-1398, 19th Joint Propulsion Conference, Seattle, Washington, June 27-29, 1983.
12. Brown, C. O., and Pinsley, E. A., "Further Experimental Investigations of a Cesium Hall-Current Accelerator," AIAA Journal, Vol. 3, No. 5, May, 1965, pp. 853-859.
13. Chubb, D. L. and Seikel, G. R., "Basic Studies of a Low Density Hall Current Ion Accelerator," (NASA TN D-3250), Feb., 1966.
14. Kaufman, H. R., Robinson, R. S., Day, M. S., and Haag, T. W., "End-Hall Thrusters," AIAA-90-2595, 21st International Electric Propulsion Conference, Orlando, FL, July 18-20, 1990.
15. Morozov, A. I., Shubin, A. P., and Elizarov, L. I., "Modern State and Future of Electric Propulsion Thrusters," presented at the Anniversary Specialist Conference on Nuclear Power Engineering in Space, Institute of Physics and Power Engineering, Obninsk, May 15-19, 1990.
16. Burgrova, A. I., Yermakov, Y. A., Morozov, A. I., and Yakunin, S. A., "A New Stage of Stationary Plasma Engine (SPE) Development," presented at the Anniversary Specialist Conference on Nuclear Power Engineering in Space, Institute of Physics and Power Engineering, Obninsk, May-15-19, 1990.
17. Sankovic, J., Hamley, J., and Haag, T., "Performance Evaluation of the Russian SPT-100 Thruster," AIAA-IEPC-93-094, 23rd International Electric Propulsion Conference, Seattle, WA, September 13-16, 1993.
18. Garner, C. E., Polk, J. E., Goodfellow, K. D., and Brophy, J., "Performance Evaluation and Life Testing of the SPT-100," AIAA-IEPC-93-091, 23rd International Electric Propulsion Conference, Seattle, WA, September 13-16, 1993.
19. Absalamov, S. K., et al., "Measurement of Plasma Parameters in the Stationary Plasma Thruster (SPT-100) Plume and its Effect on Spacecraft Components," AIAA-93-3156, 28th Joint Propulsion Conference, Nashville, TN, July 6-8, 1992.
20. Myers, R. M. and Manzella, D. H., "Stationary Plasma Thruster Plume Characteristics," AIAA-IEPC-93-096, 23rd International Electric Propulsion Conference, Seattle, WA, September 13-16, 1993.
21. Pencil, E. J., "Preliminary Far-field Plume Sputtering of the Stationary Plasma Thruster (SPT-100)," AIAA-IEPC-93-098, 23rd International Electric Propulsion Conference, Seattle, WA, September 13-16, 1993.
22. Donatelli, D. E., Cohen, H., Burke, W., Koons, H., "EMI Characteristics of a Potential Control System," Spacecraft Environmental Interactions Technology 1983, Colorado Springs, CO, Oct. 4-6, 1983, AFGL-TR-85-0018, NASA Conf. Pub. 2359.

23. Ling, H., Kim, H., Hallock, G. A., Birkner, B. W., and Zaman, A., "Effect of Arcjet Plume on Satellite Reflector Performance," IEEE Trans Ant. Prop., 39, 1412-20, 1991.
24. Ling, H., Hallock, G. A., Kim, H., and Birkner, B. W., "Near Field Interaction of Microwave Signals with a Bounded Plasma Plume," Final Report to NASA Lewis Research Center, Grant - NCC3-127, January, 1991.
25. Carney, L. M., "Evaluation of the Communications Impact of a Low Power Arcjet Thruster," AIAA-88-3105, 24th Joint Propulsion Conference, Boston, July 1988.
26. Flock, W. L., "Telecommunications in Cometary Environments," JPL Pub. 81-84, July 1, 1981.
27. Gallimore A. D., Reichenbacher, M. L., Marrese, C., Kim, S. W., and Foster, J. E., "Preliminary Characterization of a Low Power End-Hall Thruster," (AIAA-94-3012): presented at the Joint Propulsion Conference, Indianapolis, IN, June 27--29 1994.
28. Gallimore A. D., Kim, S. W., King, L. B., Foster, J. E., and Gulczinski III, F. S., "Near and Far-Field Plume Studies of a 1 kW Arcjet," Journal of Propulsion and Power (AIAA), Vol. 12, No. 1, Jan.--Feb., 1996, 105-111.
29. Ohler, S. G., Gilchrist, B. E., and Gallimore, A. D., "Non-intrusive Electron Number Density Measurements in the Plume of a 1 kW Arcjet Using a Modern Microwave Interferometer," IEEE Transactions on Plasma Science, Vol. 23, No. 3, June, 1995, 428-435.

SECTION I: TRANSPORT-PROPERTY MEASUREMENTS IN THE PLUME OF AN SPT-100 HALL THRUSTER

Lyon B. King^{*}, Alec D. Gallimore[†], and Colleen M. Marrese^{*}
Plasmadynamics and Electric Propulsion Laboratory
Department of Aerospace Engineering
University of Michigan, Ann Arbor, MI USA

Abstract

In order to understand the interaction between the SPT-100 thruster and the spacecraft, accurate knowledge of exhaust plume properties must be obtained. This investigation utilized a suite of inter-related diagnostic probes in an effort to provide detailed knowledge of the exhaust plume on a molecular kinetic level. Probes used for the investigation included a Retarding Potential Analyzer (RPA), a planar Faraday probe, an emissive probe, both total- and radiant-heat-flux probes, as well as a newly developed Neutral Particle Flux probe. Combining knowledge gained from these probes, it was possible to quantify the transport of mass, energy, and charge within the plume at 0.5-m and 1.0-m radius from the thruster exit. Among the phenomena uncovered were a high-energy ionic annulus surrounding a narrow low-energy core within the plume at 0.5-m radius from the thruster exit. This core structure was filled in a 1.0-m radius. Additionally, a population of energetic charge exchange neutrals was found within 25 deg. of the thruster centerline along with the corresponding low-energy charge exchange ions attributed to plume/background gas interactions.

Nomenclature

A_{probe}	= Area of RPA collector (m^2)
C_r	= Relative interparticle speed (m/s)
e	= Elementary charge (coulomb)
$F(V)$	= Ion energy distribution function (s/m)
$f(u_i)$	= Ion velocity distribution function (s/m)
I	= Current (A)
j_i	= Ion current density (A/m^2)
K_1	= Constant for calculating cross section (Eqn. 8)
K_2	= Constant for calculating cross section (Eqn. 8)
k	= Boltzmann Constant
m_i	= Mass of ion (kg)
m_n	= Mass of neutral (kg)
n_i	= Density of ions (m^{-3})
n_n	= Density of fast neutrals (m^{-3})

^{*} Graduate Student Researcher, Student member AIAA

[†] Assistant Professor, Senior Member AIAA

Plasmadynamics and Electric Propulsion Laboratory
1919 Green Rd. Rm. B107
Ann Arbor, MI 48105

n_m	= Measured den. of neutrals (m^{-3})
P_{coll}	= Collision probability
P_m	= Measured pressure (Pa)
q_{conv}	= Convective heat flux (W/m^2)
s	= Path length traveled by particle (m)
T_m	= Measured temperature of neutrals (K)
T_0	= Temperature of slow neutrals (K)
T_p	= Temperature of probe surface (K)
u_i	= Velocity of ions (m/s)
u_m	= Velocity of measured neutrals (m/s)
u_n	= Velocity of plume neutrals (m/s)
V	= Probe voltage (V)
λ	= Mean free path (m)
σ_c	= Total cross section for charge exchange (m^2)
$\langle x \rangle$	= Average value of quantity "x"

Introduction

In an effort to fully flight-qualify the SPT-100 for use in satellite missions, a great deal of research has focused on lifetime and performance issues of the thruster. As a result, the baseline operating conditions of the SPT-100 are now well-established.¹ The next hurdle to widespread use of these devices is to develop an understanding of thruster/spacecraft interaction phenomena. The thruster may interact with the spacecraft through three fundamental processes: thruster-generated electromagnetic interference (EMI), particle impingement from the exhaust plume, and radiant heating of spacecraft components. EMI may interfere with communication signals and instrument performance,² while particle impingement and radiant heating may cause physical damage to spacecraft hardware. This paper presents the results of a study to characterize the particle transport properties as well as the radiant heat environment produced by an SPT-100 plume.

The exhaust plume of an SPT-100 consists mainly of high-energy (200-300 eV) xenon ions produced and accelerated within the thruster. However, there are additional plume components owing to parasitic facility effects (during ground testing) and secondary ion processes occurring in the acceleration zone of the thruster. These additional components include slow propellant ions as well as both slow and fast neutral atoms.

The neutral and ionic portions of the plasma flow are linked through the process of resonant charge exchange (CEX). This process can occur within the thruster acceleration region due to entrained ambient background gas or un-ionized propellant, or it can occur downstream of the acceleration zone due to the ambient background gas. There are two approaches that can be used to detect CEX: one can either look for the slow ion products, or detect the fast neutral products since their production rates are one-to-one.

The ionic portion of the plume, both high- and low-energy, can be detected in a straightforward manner through the use of classical electrostatic plasma probes. Previous studies have used such traditional techniques as Faraday probes, Langmuir probes, and retarding potential analyzers (RPA's)^{3,4,5} to provide point measurements of the SPT-100 plume over a limited volume. The objective of this paper is to utilize the basic probes outlined above in addition to new techniques over a larger volume of the SPT-100 plume than previously investigated. This paper reports the results of a study involving a broad array of traditional and innovative plasma probes. Emphasis has been placed on the inter-relation of the probe data and the ability to derive secondary information regarding detailed plasma transport

properties. In addition, results of a new probe developed to diagnose the neutral particle flux within the plasma are reported.

Description of Probes

Emissive Probe. Emissive probes were employed to measure plasma potentials that were required to correct ion energy-distribution measurements. The probe filaments were tungsten wires that were 0.05 mm in diameter and approximately 6 mm long. Copper support wires were insulated from the plasma with alumina tubing.

Two methods were used to determine plasma potential. In the first method the filaments were heated to approximately 0.18 eV with a 60-Hz half-wave rectified sinusoidal current. The probe filament was biased with respect to ground through plasma potential with a 100-Hz triangular wave. The emission current of the probe was measured through a 1-k Ω shunt between the probe and ground. An oscilloscope was used to record the I-V characteristics during the first voltage ramp in the off segment of the heater cycle, ensuring that the filament was nearly a unipotential surface during measurements. This method is explained in greater detail by Kemp and Sellen.⁶ In the second method, the emissive probe was allowed to float in the plasma while the heater current was varied. Increasing the heater current drove the potential of the probe closer to the plasma potential at which further electron emission was retarded and the probe potential only varied slightly with an increasing heater current.⁷ The results from both measurement methods were averaged to obtain the reported values.

RPA. The most fundamental quantity from a gaskinetic standpoint for any flow is the velocity distribution function of the flow constituents. This function, when combined with the particle density, can be theoretically used to calculate any flow property of interest.

For this investigation a gridded Retarding Potential Analyzer (RPA) was used to determine the ion energy distribution in the plume. This well-known technique uses a series of electrostatic grids upstream of a collecting surface to selectively repel plasma constituents. The RPA used in this investigation employed three grids: the first grid (and probe body) was allowed to float, thus minimizing probe disturbance to the plasma. The second grid was biased at a constant negative potential to repel all plasma electrons from the collector. The third grid was an ion-retarding grid connected to a variable high voltage power supply. The potential of the ion-retarding grid is adjusted between zero and 500 V to selectively repel ions from the collector.

An account of RPA operational theory can be found in most plasma-diagnostic texts.⁸ Briefly, the potential of the ion-retarding grid is varied while monitoring the ion current incident on the collector; thus data are obtained as I(V) vs. V. The negative derivative of these data is directly proportional to the ion energy-distribution function, $F(V)$, according to

$$-\frac{dI}{dV} = \frac{e^2 n_i A_{\text{probe}}}{m_i} F(V). \quad [1]$$

The probe body, grids, and collector were fashioned from stainless steel. The insulators between grids were made of Teflon and ceramic. The entire probe was approximately 2.5 cm in diameter. The grid mesh sizes were as follows. Floating grid: 0.112 mm-dia.-wire spaced at 0.266 mm on center; electron retarding grid: 0.028 mm-dia.-wire spaced at 0.056 mm on center; and ion retarding grid: 0.042 mm-dia.-wire spaced at 0.225 mm on center. For a more detailed description of the RPA used in this investigation refer to Ref. 9.

Faraday Probe. The Faraday probe was a 2.3-cm-dia. planar disk spray-coated with tungsten. The tungsten was used to provide a very low secondary electron yield due to the impacting ions. This disk was mounted flush with the end of a stainless steel cylindrical body. The probe body acted as a shield, ensuring a uniform electric field over the face of the collecting

disk, eliminating edge effects. The collector and body of the Faraday probe were biased with a negative voltage of sufficient strength to repel all plasma electrons so only ions were collected. The ion current collected by the Faraday probe provided a direct measure of the first moment of the ion velocity distribution function, namely ion current density, j_i . By combining this direct measurement of j_i with a known value of $\langle u_i \rangle$, the ion number density can be obtained as

$$n_i = \frac{j_i}{e \langle u_i \rangle}. \quad [2]$$

Heat-Flux Probe. The convective heat-flux, or power density, is related to the third moment of the particle velocity distribution function. For this investigation a heat-flux probe was designed based on commercially available transducers. The prevailing heat transfer mechanisms to the probe are identified as convective (kinetic) heating, radiant heating, ion-electron surface recombinative heating, electron current heating, and ablative cooling (sputtering). Among these phenomena, convective and radiant heating dominate the transport of energy due to the high exhaust velocity of the thruster in addition to the intense radiation produced by both the plasma and the hot thruster body. For ion-electron recombination heating, each ion deposits energy equal to the Xe^+ ionization energy (12 eV) to the surface as it recombines with an electron from the probe. Calculations show that this mode of probe heating comprises approximately 2% of the convective heating and is therefore ignored in this analysis. Elimination of electron current heating is achieved by biasing the probe to ground potential, which was found to be between 5 and 8 volts lower than plasma potential (see Fig. 4). Previous studies have measured the electron temperature to be close to 3 eV in the plume,³ the grounded probe therefore collected negligible electron current. The ablative cooling is assumed to be insignificant in this model. Although comprehensive data for sputtering of surfaces exposed to 300 eV Xe^+ are not available, the kinetic and radiant heating of the hot plume are believed to be much larger than the ablative cooling.

The probe is shown in Fig. 1. The probe consisted of a water-cooled housing containing two identical Schmidt-Boelter heat-flux transducers placed 5 mm apart. The housing was instrumented with a thermocouple to provide a measurement of probe surface temperature. Each transducer was coated with optical black. One transducer was exposed directly to the environment to obtain a measure of total heat-flux. The second identical transducer was covered by a sapphire window; this window shielded the device from convective heat-flux. The useful transmission-wavelength range of sapphire is 200-5,500-nm. Previous research has shown the plasma emissions in the SPT-100 plume to be confined mostly to 400-700-nm,^{10,11} while the black-body radiation from the hot thruster has an expected peak between 1,000 and 5,000-nm. It follows that the sapphire window is effectively transparent to the dominant forms of radiated energy within the plume and provides an effective measure of radiant-heat-flux. Calibration of these transducers, including the sapphire window configuration, was performed by the manufacturer to NIST-traceable standards over the heating and wavelength values expected in this test.

By subtracting the measured radiant-heat-flux from the measured total heat-flux and approximating the heat transfer as outlined above, the particle convective heating can be calculated. Within this model, the convective heat-flux to such a probe is given as the difference between the incident plume heating and the reflected convective cooling, namely

$$q_{\text{conv}} = n_i \left[\frac{1}{2} m_i \int_0^\infty u_i^3 f(u_i) du_i - 2kT_p \int_0^\infty u_i f(u_i) du_i \right]. \quad [3]$$

It is apparent from Eqn. 3 that a direct measurement of q_{conv} combined with known values for the first and third moments of the ion velocity distribution function, $f(u_i)$, and the probe body temperature, T_p , can be used to solve for the ion density, n_i .

It is important to note that the heat-flux probe employs no retarding electrostatic fields, nor does it rely on charge-carrying particles for detection. Therefore, even though Eqn. 3 is written solely in terms of ion properties, the measured convective heat flux is actually due to both ions and neutral particles. It is possible (as will be shown in Analysis) to calculate information about the neutral plasma component by comparing the heat flux-derived ion density to the Faraday probe-derived ion density.

NPF Probe. In an attempt to characterize the neutral particle component of the plasma flow a new probe design was implemented. This probe is referred to as a Neutral Particle Flux (NPF) probe. Detailed documentation of this design is presented elsewhere,¹² however an overview of the probe operation will be presented here.

The probe is essentially a hybrid between an RPA and a vacuum pressure gauge. A set of electrostatic grids are mounted to the inlet of a hot cathode ionization gauge tube. By using one grid as an electron-retarding grid and setting another grid to a high positive voltage to repel all ion flux from the tube, only the neutral component of the plasma is permitted to enter the tube. This neutral gas is ionized and sensed in the standard method of hot cathode ionization gauges. The gauge output is monitored on a standard hot cathode ionization gauge controller calibrated for Xe. A schematic of the NPF probe is shown as Fig. 2.

The pressure measured inside the ionization gauge tube is determined by the condition that the neutral particle flux entering the probe must be equal to the neutral particle flux exiting the probe. Specifically,

$$n_n \langle u_n \rangle_{in} = n_m \langle u_m \rangle_{out} \quad [4]$$

In Eqn. 4, quantities with a subscript n denote neutral particle properties within the plume, while quantities with a subscript m denote neutral particle properties within the measurement volume (gauge tube). Using free molecular theory to calculate the escape flux from the ion gauge tube yields

$$n_m \langle u_m \rangle_{out} = n_m \sqrt{\frac{kT_m}{2\pi m_n}} \quad [5]$$

Utilizing the ideal-gas law to express n_m in terms of measured pressure, P_m , and inserting this result into Eqns. 4 and 5 yields the relationship between probe-measured pressure and neutral particle flux into the probe:

$$n_n \langle u_n \rangle_{in} = \frac{P_m}{\sqrt{2\pi m_n kT_m}} \quad [6]$$

It is apparent, then, that the pressure measured within the probe ionization gauge at a constant gauge temperature is directly proportional to the flux of neutral particles in the plume.

Experimental Set-up

Facility. All tests were performed in the University of Michigan's Plasmadynamics and Electric Propulsion Laboratory (PEPL). The centerpiece of this laboratory is a large 6-m-dia. by 9-m-long vacuum chamber capable of base pressures of approximately 2.7×10^{-5} Pa at pumping speeds of over 25,000 l/s on xenon. A detailed description of this facility has been published previously.¹³ Data were acquired and processed using a computerized digital data-acquisition system.

SPT-100. The thruster used for this experiment was a Fakel flight model SPT-100 Hall-effect thruster. The thruster was controlled by a Space Systems/Loral power processing unit (PPU). Nominal operating conditions were utilized: discharge voltage=300 V, discharge current=4.5 A, total flow rate of 56 SCCM of Xe with a 7% cathode split. Tank pressure was

maintained at less than 6×10^{-3} Pa true Xe pressure during all testing as determined by two hot-cathode ionization gauges.

Probes. The Faraday probe body, collector and the RPA electron retarding grid were biased approximately -30 V with respect to the thruster cathode potential. This voltage was sufficient to repel all plasma electrons while attracting only ion current.³ The RPA ion retarding grid was adjustable from 0 to approximately 500 V.

The heat-flux probe water-cooling lines were connected to a closed-loop thermostatically controlled refrigeration system. The probe body maintained a temperature of between 5 and 6 deg. C for all test points.

The NPF probe electron retarding grid was also set at -30 V with respect to thruster cathode potential. The ion retarding grid of the NPF was set to a constant value of 500 V. This value, as determined from an RPA-type trace of probe output, was sufficient to repel all plume ions, admitting only neutral particles.¹²

Test Set-up. For each test, three probes were mounted simultaneously to a rotating boom apparatus on a computerized remote positioning system. An overview of the set up is shown as Fig. 3. The instruments were positioned 0.5-m from the boom pivot point. By positioning the pivot point directly beneath the thruster exit plane it was possible to obtain probe data at various angles off thruster centerline at a constant radial distance of 0.5-m by simply rotating the boom. As indicated in Fig. 3, positive angles off centerline indicate measurements taken on the cathode side of the thruster, while negative angles denote the non-cathode half plane. This convention will be followed throughout the paper. By translating the pivot point of the instrument boom in addition to rotation, data were collected at radial positions of 1.0-m from the thruster exit plane while ensuring that the probes remained normal to the flow. Angular resolution of the traversing mechanism is better than 0.1 deg.; however initial alignment of the probes with the "zero" point (thruster axis) could only be confidently performed to within 3 deg. The relative uncertainty in angular position between data points is thus 0.1 deg., but the 3 deg. absolute offset has been conservatively indicated as an error bar for all data points.

Upon completion of the baseline data sets the Faraday probe configuration was changed: the Faraday probe was turned "backward" to quantify the background ambient plasma conditions separately from the direct plume flux. In this position the collecting surface of the probe remained at 0.5-m radius from boom pivot point, however the probe faced directly away from the thruster. This allowed the probe body to shield the collecting surface from the direct plume flux, creating a quiescent wake. By sampling the ion current flux within this wake it was possible to directly measure the ambient background plasma conditions due to chamber pumping limitations and CEX.

Results

Emissive Probe. Plasma potential measurements were taken in the negative half-plane of the thruster plume between 0 and -60 deg. off centerline at both 0.5-m and 1.0-m radial distance. At 0.5-m measurements were taken every 15 deg., while the 1.0-m data set includes measurements every 10 deg. The plasma potential varied between 7.2 V and 5.4 V with respect to tank ground, while the thruster cathode remained at a constant -22 V with respect to tank ground. These measurements are shown in Fig. 4.

RPA. RPA data were collected in the negative half-plane (non-cathode side) of the thruster from centerline out to -60 deg. Beyond 60 deg. off axis the collected current fell to levels for which the numerical differentiation required for data reduction produced unacceptably large error-to-measurement ratios. Thus, all successive probe data were limited to points for which RPA traces were available. For the 0.5-m data set, sweeps of ion current vs. retarding voltage were recorded every five deg., with sweeps every ten deg. for the 1.0-m data. Peak ion-

current values were in the range of tens of μA near centerline down to hundreds of nA far off centerline for both 0.5-m and 1.0-m sweeps. Examples of these sweeps are shown as Fig. 5 for the 0.5-m data set. The 10% measurement error represents uncertainties in the collected current. These uncertainties were then propagated through all plume analyses incorporating integrated values based on RPA measurements.

Faraday Probe. Ion current density was measured in the full plane both at 0.5-m radius and 1.0-m from -60 to 60 deg. at five-deg. increments. The centerline-plume ion-current density fell from 5 mA/cm^2 at 0.5 m to about 1.6 mA/cm^2 at 1.0 m. The background wake ion current flux showed similar trends, however the current values were two orders of magnitude lower than the corresponding ram flux. The Faraday probe data are shown in Fig. 6. The indicated 10% error is due to uncertainties in the measured current and probe collection area.

Heat-Flux Probe. Data were obtained with the heat flux probe at 2-deg. increments from -60 deg. to 60 deg. at 0.5-m radius from thruster exit and five deg. increments at 1.0 m. For the positions of -2, 0, and 2 deg. at 0.5 m, the measured total heat-flux exceeded the calibrated range of the sensor. Total heat-flux data are therefore unavailable for these points. The radiant- and total-heat-flux data are shown in Fig. 7. Due to plasma sputtering the surface texture, and therefore the transmission properties of the sapphire window are expected to change over time. However, the entire data set reported in Fig. 7 required the heat-flux probe to be exposed to the plasma for less than 60 seconds. Over this short period no appreciable variation in the window surface was expected; post-test visual inspection confirmed the absence of window damage. The 10% error indicated in Fig. 7 represents uncertainties in calibration as reported by the transducer manufacturer over the measurement range of interest, with an additional 2% error to reflect neglect of ion-electron surface recombinative heating.

NPF Probe. The NPF probe data were obtained at 2-deg. increments in the half plane from -60 deg. to 0 deg. at 0.5 m and at 5-deg. increments at 1.0 m. The over-pressure protect set point for the hot-cathode tube was set for 0.8 Pa. Above this pressure, the tube de-energized in order to prevent damage to the filament. Because of this, data within 10 deg. of centerline could not be obtained at either 0.5 m or 1.0 m. The NPF probe data are shown in Fig. 8. Error bars reflect uncertainty in calibration of total pressure gauge as supplied by the manufacturer.

Analysis and Discussion

Ion Energy Distribution. As shown in Eqn. 1, the non-normalized ion energy distribution can be obtained by numerically differentiating the $I(V)$ vs. V data sweeps of the RPA. Although the values of A_{probe} and n_i are required to find $F(V)$ via Eqn. 1, differentiation of the raw data provides a curve that is directly proportional to $F(V)$. This curve can then be normalized such that the total area under the curve is unity providing a direct calculation of $F(V)$ independent of the constants A_{probe} and n_i . In order to ensure the accuracy of the ion energy distribution a discrete but important correction must be applied to the RPA data: although the first grid and probe body were allowed to float, the ion energy is recorded in volts with respect to thruster cathode potential. This induces an energy shift to the ions as they fall from plasma potential to reference cathode potential. The cathode potential was monitored and found to be approximately -22 V with respect to tank ground. As can be seen from the plasma potential data of Fig. 4, this imposes an appreciable energy shift to the ions (on the order of 30 V) which must be accounted for during post-processing.

The entire data set of ion energy distribution curves is not included in the present paper, however, the dominant trends are evident in the sample data of Fig. 9. For angles near thruster centerline, the ion energy distribution is sharply peaked near a most probable energy of around 230 V, with a full-width-at-half-max (fwhm) of 100 V at -30 deg. off centerline. For larger angles, the distribution becomes much broader due to the appearance of a population of lower

energy ions. Although the most probable ion energy remains 230 V, the fwhm is increased to more than 150 V at -45 deg. This broadening of the energy distribution for large angles was evident in all data points for both 0.5-m and 1.0-m data sets, however the most probable ion energy remains very near 230 V for each trace. Although the thruster discharge voltage was 300 V, a high-energy "tail" of ions with energies greater than the discharge voltage was found in all RPA traces. The size of this tail was largest for angles near thruster centerline and decreased with increasing angle. Furthermore, the tail was smaller in the 1.0-m data sets than for corresponding angles in the 0.5-m data. Although the existence of this tail has been documented by other researchers,¹⁴ a precise explanation for its origin remains unclear.

Quantitatively, the ion energy distribution curves can be better understood by numerically evaluating the first few moments. Previous research has shown the plume of the SPT-100 to be comprised almost entirely of singly ionized Xe.¹⁰ Utilizing this assumption, it is trivial to convert the ion energy distributions, $F(V)$, to ion velocity distributions, $f(u_i)$. The moments of these velocity distributions can then be evaluated and utilized to calculate ionic transport properties. The first moment, or average ion velocity, was computed numerically and is shown in Fig. 10 for both 0.5 m and 1.0 m radius. The error bars of Fig. 10 represent the propagation of original measurement uncertainties through the numerical integration.

A striking result of this analysis was the discovery of a very narrow low-energy core surrounded by a slightly higher-energy annulus with a peak at -20 deg. in the plume at 0.5-m radius from thruster exit. Although such a topology would be expected in the near field of the thruster due to the annular shape of the discharge chamber, it was believed that the divergence of the ion beam would smear out this configuration very rapidly. On the contrary, the average ion velocity on centerline at 0.5-m is less than the velocity computed for any other point measured in the 0.5-m data set. This low-energy core is very narrow, limited to a region in space with a half angle of 5 deg. about thruster centerline. It should be noted, however, that this annulus structure was not uncovered in the Faraday probe data. Since the Faraday probe measures $n_i \langle u_i \rangle$, the rapidly increasing ion density near centerline overwhelms the dip in $\langle u_i \rangle$ and a monotonically increasing ion current density results. The high-energy annulus/low-energy core structure is not present in the 1.0-m data set. At this downstream location the beam divergence has completely filled in the core. In addition to the smearing of the spatial energy structure, the ion velocity for large angles (greater than 30 deg.) is much less at 1.0 m than at 0.5 m.

The existence of a high-energy plasma annulus with low spatial divergence is consistent with thruster discharge chamber geometry and field topology. The high-energy ions are formed closer to the anode and hence, further back inside the discharge chamber. These ions, in order to escape the discharge chamber without colliding with the wall, must have their velocity vectors geometrically contained within a defined solid angle. Those ions formed near the end of the discharge chamber farther from the anode will have lower energy as a consequence of the field topology, and will also have their velocity vectors distributed about a larger allowed solid angle.

The low-energy core in the mid-to-near field is most likely due to the distribution of ion production within the discharge chamber. According to data obtained by Bishaev and Kim,¹⁵ the majority of the ionization within the thruster occurs very near the inner wall of the discharge chamber. In order for these ions to escape the discharge chamber without colliding with a wall and being neutralized, their velocity vectors must be directed largely away from thruster centerline. Such a distribution of velocity vectors would produce a depletion of high-energy ions on thruster centerline until a considerable distance downstream. Such a scenario is depicted conceptually in Fig. 11, with the high-ion-formation region of Bishaev and Kim indicated.

Density Distribution. With the broad inter-related suite of data obtained in this study, it was possible to calculate two measures of particle density. In the first method, the

Faraday probe-measured ion current density, j_i , is combined with the first moment of the ion velocity distribution function, $\langle u_i \rangle$, and used to predict the ion density according to Eqn. 2. The second method is based on the heat-flux-probe data: by subtracting the measured radiant heat-flux from the measured total heat-flux, the value of particle convective heating, q_{conv} , is obtained. Combining q_{conv} with numerically calculated values of $\langle u_i \rangle$ and $\langle u_i^3 \rangle$, and recalling that the heat-flux probe is sensitive to both neutrals and ions, the total particle density (ion and neutral) can be calculated according to Eqn. 3.

Based on the methods outlined above, two separate values of particle density are presented in Fig. 12 for the 0.5-m data, and Fig. 13 for the 1.0-m data. The error bars in Figs. 12 and 13 represent the propagation of all original measurement uncertainties. As can be seen in the figures, both methods of calculating particle density produce comparable results indicating that neutrals represent only a small fraction of the flow. The maximum difference between the values at 0.5 m is approximately 25% at -5 deg., with a somewhat larger discrepancy of 40% on centerline at 1.0 m.

Neutral-Particle Properties. The neutral component of the plume was evaluated in this investigation using two methods: direct measurement of neutral particle flux using the NPF probe, and calculation of neutral particle properties based on the inter-relation of other probe data. The measured neutral pressure within the NPF probe displayed as Fig. 8 can be converted via Eqn. 6 to provide a measure of neutral particle flux. This quantity is plotted in Fig. 14 for both the 0.5-m and 1.0-m data sets. The NPF data suggest a region of high neutral particle flux near plume centerline. Although the data sets are limited to angles larger than 10 deg., it is evident that a well defined core of neutral particles is present in the plume. This core is surrounded by a region of depressed neutral flux bottoming out at about -25 deg., followed by a subsequent rise to ambient background pressure outside of about -40 deg. The region of depleted neutrals near -25 deg. corresponds loosely with the high-energy ionic annulus shown in Fig. 10 at 0.5 m. The relationship between the depressed neutral flux and elevated ion energy is not fully understood at this writing.

The second method of determining neutral properties stems from the inherent difference between the Faraday probe and the heat-flux probe. By subtracting values calculated on the basis of Faraday data from values calculated from the heat flux data, it is possible to quantify the contribution of the neutral flow. This method was used to evaluate the neutral particle heat-flux. The value of convective heat flux due to both neutrals and ions was calculated by subtracting the measured radiant heat-flux from the measured total heat-flux. The ionic contribution to the convective heat flux was derived according to Eqn. 3 with the ion density calculated from the Faraday probe data via Eqn. 2. Subtracting the derived ionic heat-flux from the measured convective (ion and neutral) heat-flux yields the value of neutral particle heating. This quantity is plotted in Fig. 15 for both 0.5-m and 1.0-m data sets, with error bars representing the propagation of all measurement uncertainties. As expected, the neutral particle heating is greater at 0.5 m than at 1.0 m. Furthermore, the neutral heating is confined to a region within 25 deg. of thruster centerline falling off to negligible values sharply for larger angles. This corroborates the NPF data which also showed the neutral flux to be contained within a well-defined region with a half angle of 25 deg.

CEX Processes. As stated in the introduction, CEX processes can be evaluated either by quantifying the slow ion products or the fast neutral products since their production rates are one-to-one. In this investigation both methods of detecting CEX products were attempted.

Analysis of the neutral component of the plasma is missing one vital piece of information to close the CEX analysis: the value of the neutral particle velocity distribution function. However some insight to the neutral component can be derived from available quantities. From a top level perspective, it would be valuable to know whether the neutrals detected by the NPF are "slow" ambient background particles, or "fast" CEX products. If we assume that the neutrals are slow, macroscopically stagnant Maxwellian particles at

temperature T_0 , then the free molecular convective heating to the water cooled probe is computed as

$$q_{\text{conv}} = \frac{1}{4} n_n \langle u_n \rangle k (T_n - T_p). \quad [7]$$

Since the flow has been assumed to be stagnant, the pressure measured by the NPF probe would be the true ambient neutral pressure; this could be converted via the ideal gas law to obtain n_n . Evaluating Eqn. 7 for the sample point at -15 deg. from centerline at 0.5 m where $P_m = 0.8$ Pa (from Fig. 8), and assuming a neutral background temperature $T_n = 300$ K yields a value of neutral particle convective heating of 3.2×10^{-4} W/cm². This is 250 times lower than the value of 0.08 W/cm² obtained from the data for the neutral heating at this location (see Fig. 15). Even if the assumed background neutral temperature is increased in order to agree with the data-obtained heating, the neutrals would have to have an unrealistically high temperature of over 100,000 K at this sample point to account for the 0.08 W/cm² measured neutral heating. It is apparent that a distribution of slow neutrals cannot account for the measured neutral convective heating and that the neutrals measured with the NPF probe are most likely highly-energetic CEX products.

The appearance of CEX products is supported by a statistical collision analysis of the plume/background gas interaction. The charge exchange collision cross section for $\text{Xe}^+ - \text{Xe}$ can be computed according to¹⁶

$$\sigma_c = (K_1 \ln C_r + K_2)^2 \times 10^{-20} \text{ m}^2 \quad [8]$$

with $K_1 = -0.8821$ and $K_2 = 15.1262$. For this investigation, with an average relative interparticle speed $C_r = 17$ km/s and a tank background pressure of 6×10^{-3} Pa, the CEX mean free path is approximately 1.5 m. Although this mean free path is longer than the largest path length in this investigation (1.0 m), examination of the collision statistics reveals that the effect of CEX is not negligible. The fraction of particles which undergo a collision within a path length "s" is given by the well-known survival equation as

$$P_{\text{coll}}(s) = (1 - e^{-s/\lambda}). \quad [9]$$

Eqn. 9 shows that at 0.5 m from the thruster exit, almost 30% of the emitted plume ions have suffered a CEX collision; this increases to a value of almost 50% of the ions undergoing a CEX collision by 1.0 m. In reality, the tank background pressure of 6×10^{-3} Pa is not composed entirely of neutral Xe. Due to facility base-pressure limitations, a portion of this background pressure is residual air. Although accounting for this lower background Xe density would increase the computed $\text{Xe}^+ - \text{Xe}$ mean free path, other non-resonant collisions between particles of dissimilar masses must be accounted for; these collisions would likely affect the plume ions similarly to the ideal case considered here.

Conclusion

By making comprehensive measurements of related ion and neutral-particle properties within the plume, it was possible to gain insight into plume structure and thruster operation. The phenomena investigated included ion-neutral charge-exchange, spatial distribution of ion energy within the plume, and information regarding beam and ambient plasma properties.

Analysis revealed that the plume possesses a very narrow low-energy core surrounded by an annulus of slightly higher energy at 0.5 m radius from the thruster exit. This core is filled in by beam divergence at 1.0 m. This structure is consistent with thruster discharge chamber geometry, field topology, and distribution of ion production.

Through the use of a new probe design coupled with heat-flux measurements, it was possible to derive information regarding neutral particle properties within the plume. The

data analysis suggests that these neutral particles are the high-energy products of ion-neutral CEX collisions. Furthermore, these high-energy neutrals are contained almost entirely within a cone with a half-angle of 25 deg. off thruster centerline. It is apparent that facility-induced interactions between background gas and plume ions are not negligible even at mPa tank pressures.

Acknowledgments

The authors would also like to thank Mr. Michael Day of Space Systems/Loral for use of the SPT-100 and PPU, instrument fabricator Terry Larrow, and PEPL researchers Matt Domonkos, John Foster, James Haas, and Sang-Wook Kim.

Section I References

- [1] Garner, C.E., Brophy, J.R., Polk, J.E., and Pless, L.C., "A 5,730-Hr Cyclic Endurance Test of the SPT-100," AIAA-95-2667, 31st AIAA/ASME/SAE/ASEE Joint Propulsion Conference, July 10-12, 1995, San Diego, CA.
- [2] Ohler, S., Gilchrist, B., and Gallimore, A., "Microwave Plume Measurements of an SPT-100 using Xenon and a Laboratory Model SPT using Krypton," AIAA-95-2931, 31st AIAA/ASME/SAE/ASEE Joint Propulsion Conference, July 10-12, 1995, San Diego, CA.
- [3] Myers, R.M., and Manzella, D.H., "Stationary Plasma Thruster Plume Characteristics," IEPC-93-096, Proc. of 23rd Int'l Electric Propulsion Conference, Vol. 2, 1993, pp. 893-912.
- [4] Manzella, D.H., and Sankovic, J.M., "Hall Thruster Ion Beam Characterization," AIAA-95-2927, 31st AIAA/ASME/SAE/ASEE Joint Propulsion Conference, July 10-12, 1995, San Diego, CA.
- [5] Pencil, E.J., Randolph, T., and Manzella, D.H., "End-of-life Stationary Plasma Thruster Far-field Plume Characterization," AIAA-96-2709, 32nd AIAA/ASME/SAE/ASEE Joint Propulsion Conference, July 1-3, 1996, Lake Buena Vista, FL.
- [6] Kemp, R. F., and Sellen Jr., J. M., "Plasma Potential Measurements by Electrons and Emissive Probes," Rev. Sci. Instrum. 37 (4), Apr. 1996, pp. 455-61.
- [7] Hershkowitz, N., "How Langmuir Probes Work," appears in Plasma Diagnostics: Discharge Parameters and Chemistry, Auciello, O., and Flamm, D., eds., Vol. 1, Academic Press, Inc., San Diego, CA, 1989.
- [8] Hutchinson, I.H., Principles of Plasma Diagnostics, Cambridge University Press, 1987.
- [9] Marrese, C.M., Gallimore, A.D., Haas, J., Foster, J.E., King, L.B., and Kim, S.W., "An Investigation of Stationary Plasma Thruster Performance with Krypton Propellant," AIAA-95-2932, Joint Propulsion Conference, July 10-12, 1995, San Diego, CA.
- [10] Manzella, D.H., "Stationary Plasma Thruster Plume Emissions," IEPC-93-097, Proc. of 23rd Int'l Electric Propulsion Conference, Vol. 2, 1993, pp. 913-23.
- [11] Leray, P., Bonnet, J., and Pigache, D., "Spatially Resolved Emission Spectroscopy Along a SPT Channel. Interpretation of Data by Collisional-Radiative Model," IEPC-97-054, Proc. of 25th International Electric Propulsion Conference, 1997.

- [12] King, L.B., and Gallimore, A.D., "A Gridded Retarding Pressure Sensor for Ion and Neutral Particle Analysis in Flowing Plasmas," *Rev. Sci. Instrum.* 68 (2), Feb. 1997.
- [13] Gallimore, A.D., Kim, S.W., Foster, J.E., King, L.B., and Gulczinski III, F.S., "Near- and Far-field Plume Studies of a 1 kW Arcjet," *Journal of Propulsion and Power*, Vol 12, No. 1, Jan-Feb 96, pp. 105-11.
- [14] Burgrova, A.I., Desyatskov, A.V., and Kharchevnikov, V.K., "Experimental Determination of Ion Energy at the Outlet of SPT-ATON," *IEPC-95-47, Proc. of 24th Int'l Electric Propulsion Conference*, Vol. 1, pp. 364-365.
- [15] Bishaev, A.M, and Kim, V., "Local Plasma Properties in a Hall-current Accelerator with an Extended Acceleration Zone," *Sov. Phys. Tech. Phys.* 23 (9), Sept. 1978, pp. 1055-57.
- [16] Rapp, D., and Francis, W. E., "Charge Exchange Between Gaseous Ions and Atoms," *Journal of Chemical Physics*, Vol. 37, No. 11, 1962, pp. 2631-2645.

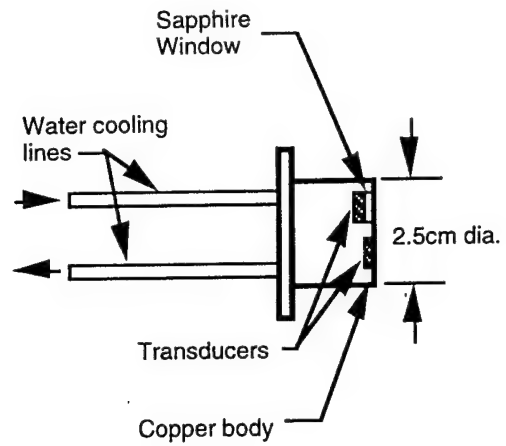


Figure 1. Schematic of Heat-flux probe showing both radiant- and total-heat-flux transducers.

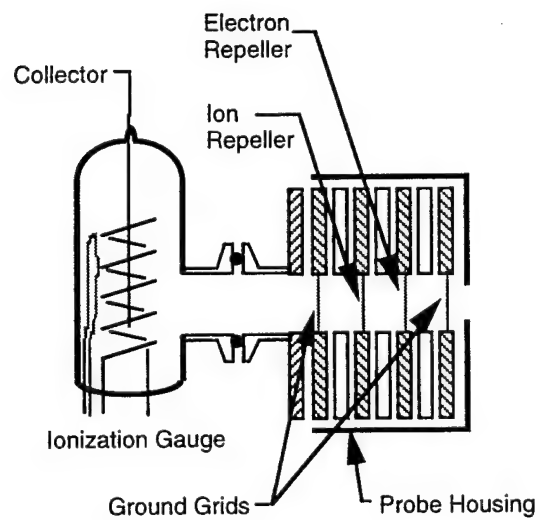


Figure 2. Schematic of NPF probe showing grid arrangement and ionization gauge.

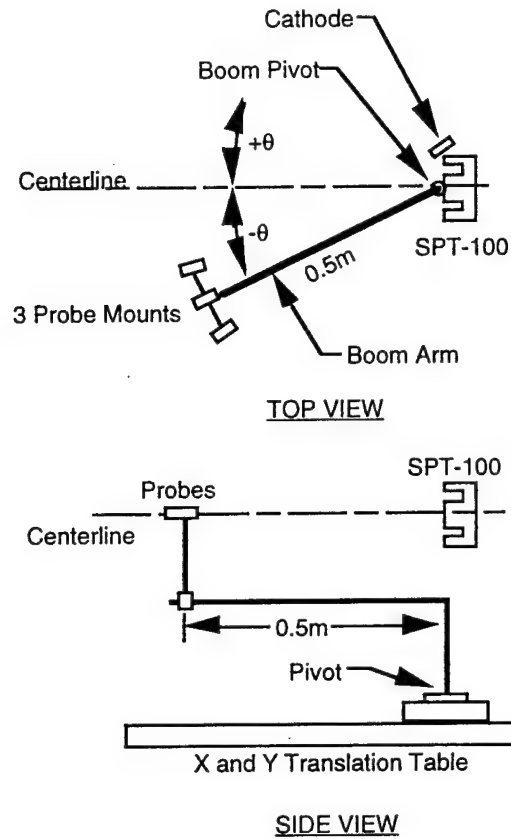


Figure 3. Experimental set-up showing boom/table/thruster layout and angle sign conventions.

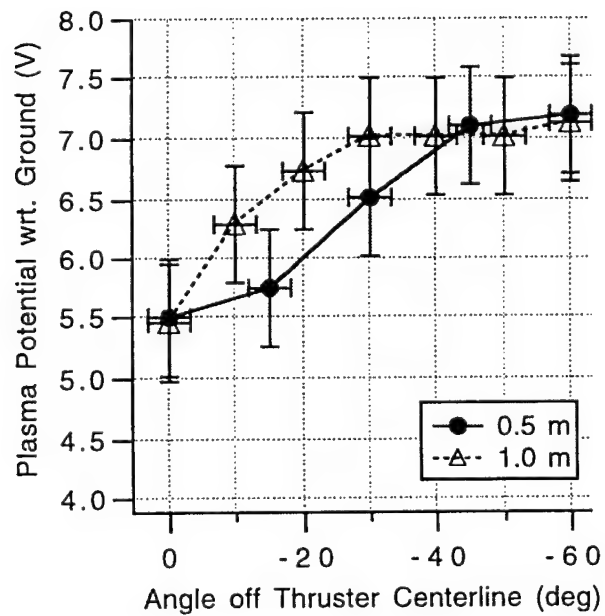


Figure 4. Plasma potential measurements at 0.5-m and 1.0-m radius from thruster.

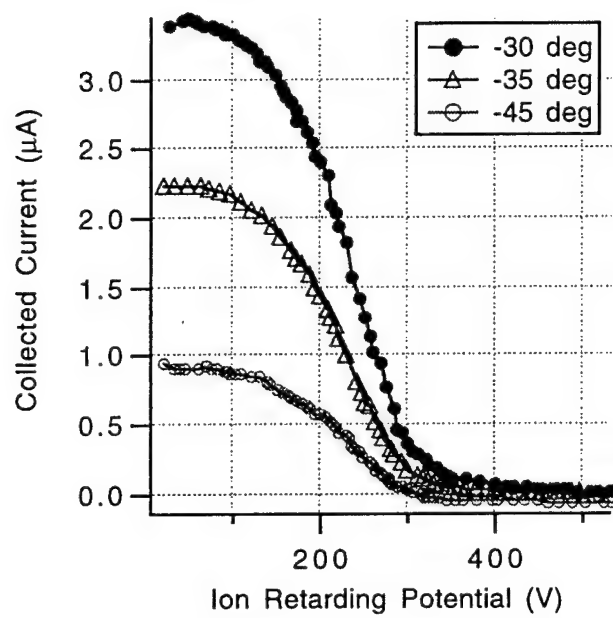


Figure 5. Sample RPA I-V characteristic curves at 0.5-m radius from thruster. Ion retarding potential is with respect to thruster cathode. Uncertainty in current is less than 10%.

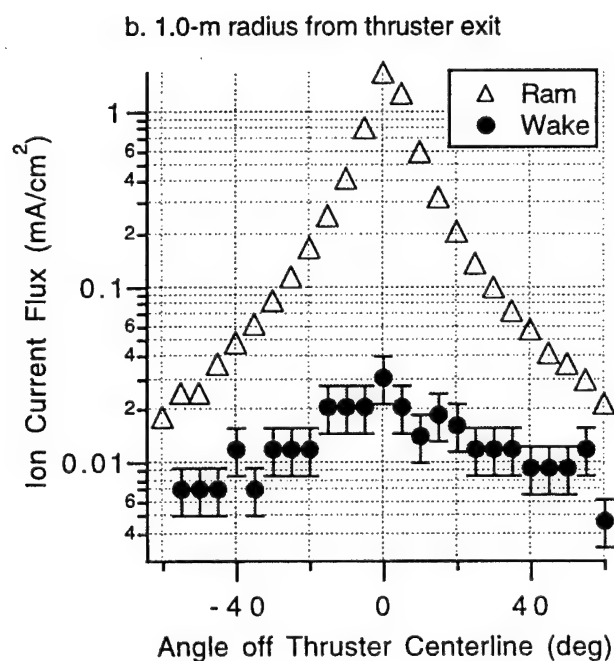
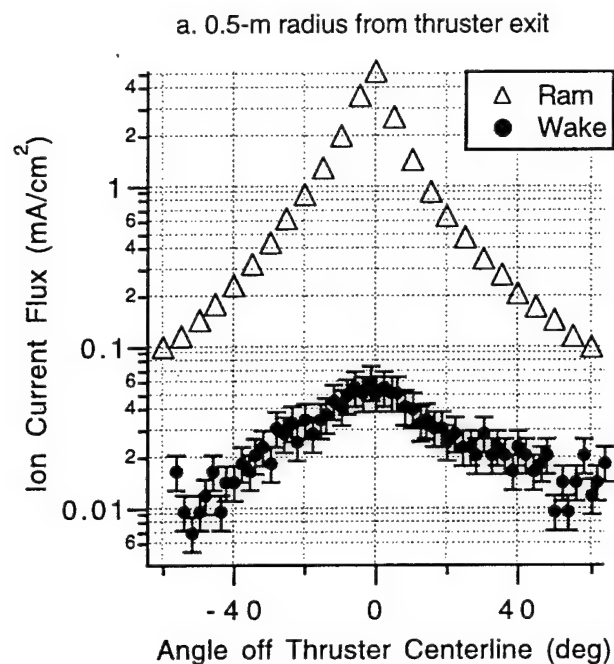
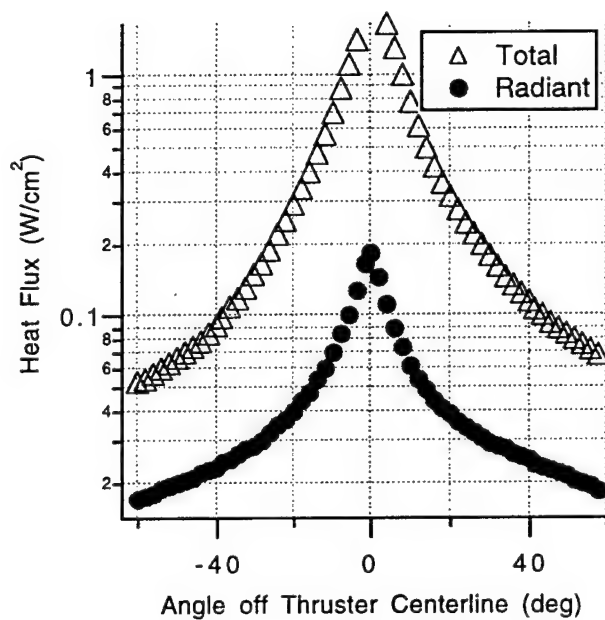


Figure 6b. Ram and wake ion current density at 0.5-m and 1.0-m radius from thruster exit. Uncertainty in angular position is 3 deg., uncertainty in ram current flux is less than 10%.

a. 0.5-m radius from thruster exit



b. 1.0-m radius from thruster exit

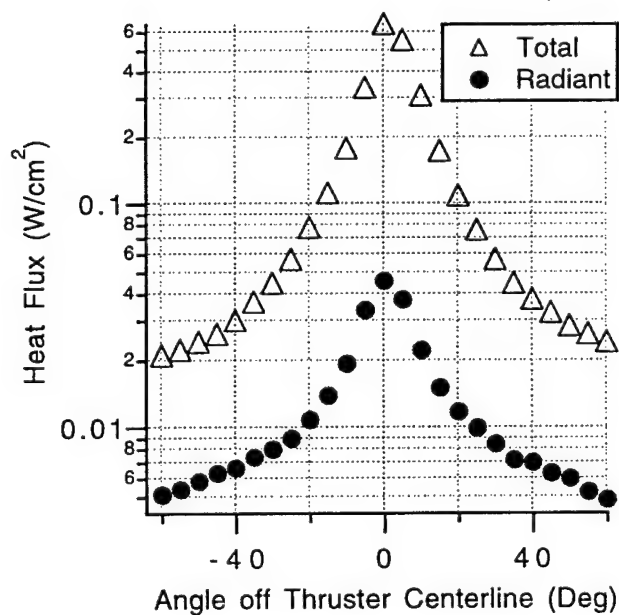


Figure 7. Radiant- and total-heat-flux measurements 0.5-m and 1.0-m radius from thruster exit. Uncertainty in heat-flux less than 10%, uncertainty in angular position is 3 deg.

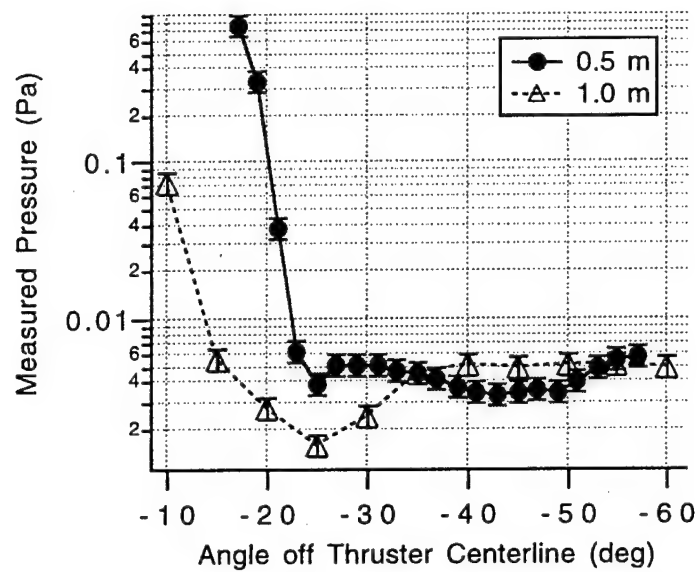


Figure 8. Measured pressure inside NPF gauge tube at 0.5-m and 1.0-m radius. Uncertainty in angular position is 3 deg.

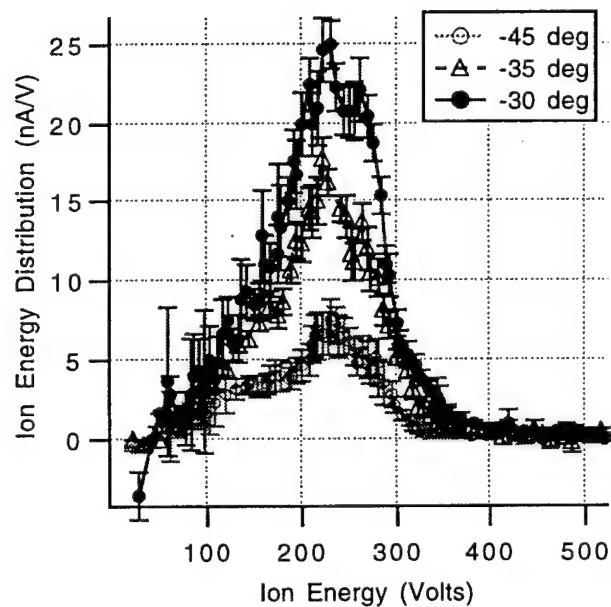


Figure 9. Sample of non-normalized ion-energy distribution curves at 0.5-m radius from thruster exit. Ion energy is with respect to thruster cathode.

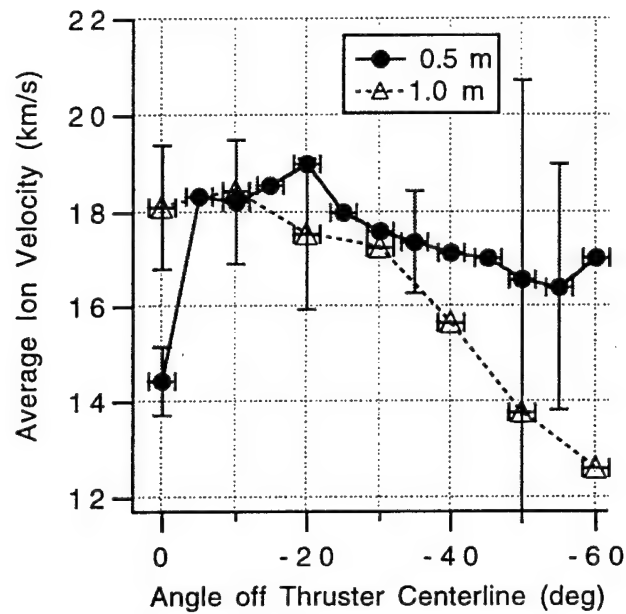


Figure 10. Average ion velocity based on RPA data at 0.5-m and 1.0-m radius. Sample error bars included to indicate magnitude of uncertainty due to propagated errors.

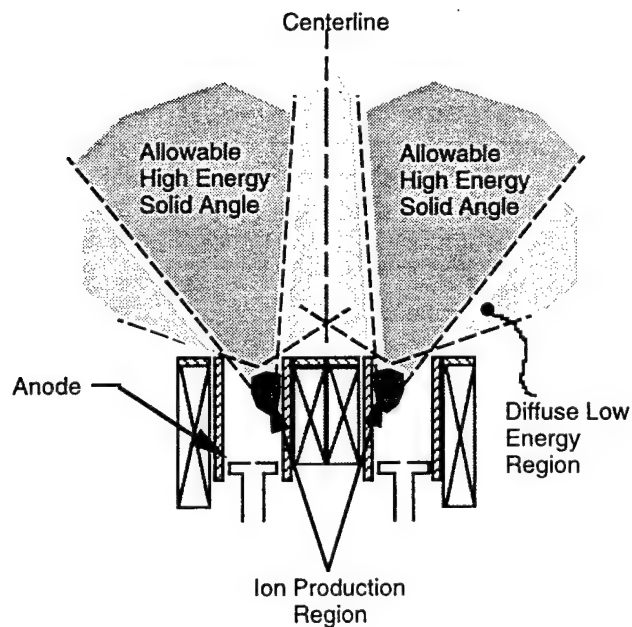


Figure 11. Schematic representation of mechanism causing high-energy annulus and low-energy core in thruster plume. Ion production region denoted as according to Bishaev and Kim.¹⁵ High-energy ions are formed closest to anode.

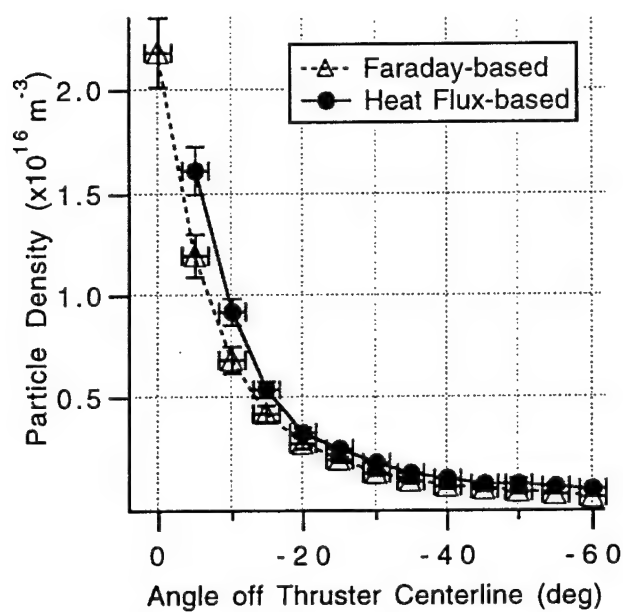


Figure 12. Comparison of calculated particle density based on heat-flux-probe and Faraday probe at 0.5-m radius from thruster.

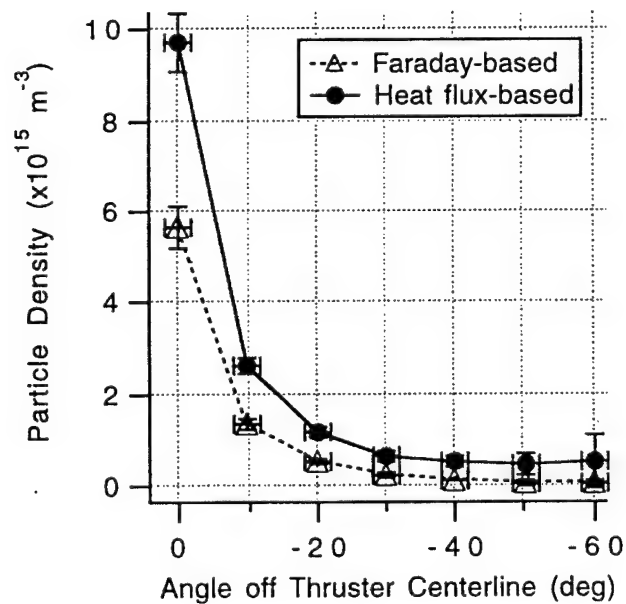


Figure 13. Comparison of calculated particle density based on heat-flux-probe and Faraday probe at 1.0-m radius from thruster.

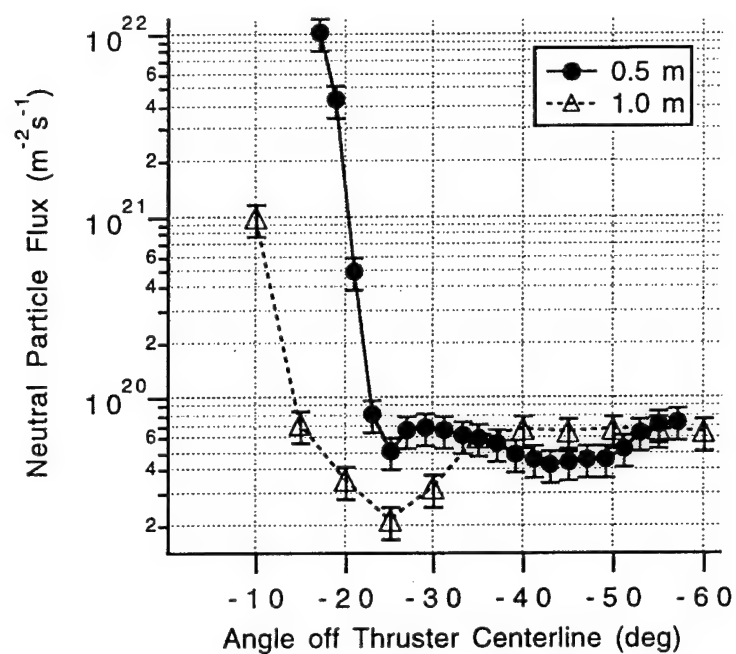


Figure 14. Measured neutral particle flux at 0.5-m and 1.0-m radius.

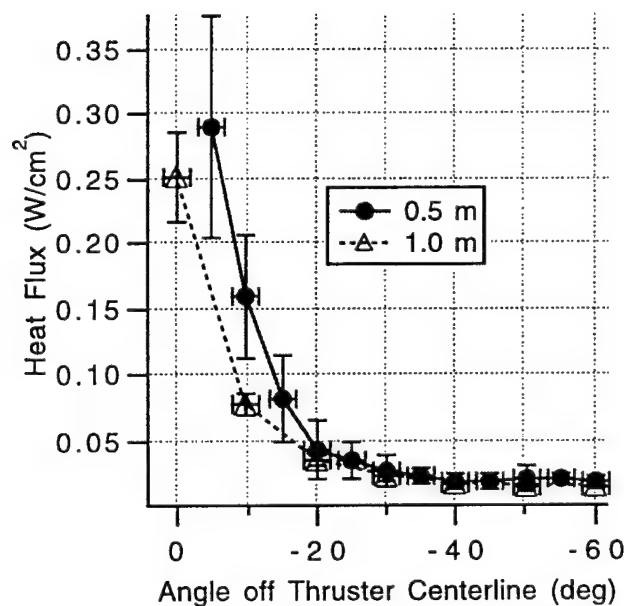


Figure 15. Calculated neutral particle convective heating at 0.5-m and 1.0-m radius.

SECTION II: ELECTROMAGNETIC SIGNAL MODIFICATION IN A LOCALIZED HIGH SPEED PLASMA FLOW: SIMULATIONS AND EXPERIMENTAL VALIDATION OF A STATIONARY PLASMA THRUSTER (SPT)

Shawn G. Ohler
Lincoln Laboratory, Massachusetts Institute of Technology
Cambridge, MA

Brian E. Gilchrist and Alec D. Gallimore
University of Michigan
Ann Arbor, MI

Abstract

High frequency electromagnetic signals are modified by plasmas primarily through strong density gradients or by densities approaching the critical plasma density. A plasma can potentially degrade an electromagnetic based system through signal attenuation as well as added amplitude or phase noise. This paper reviews the physical mechanism and applies a general ray tracing modeling method to understand the possible phase shift, attenuation, phase modulation, and amplitude modulation produced by the localized, high speed plasma flow of a stationary plasma thruster (SPT). The SPT is currently being tested and considered for use aboard next generation spacecraft where careful consideration must be given to possible interactions with satellite electromagnetic systems such as for communication, navigation, and remote-sensing. The study also models the rather significant plume impact to phase and amplitude for lower frequencies. A summary is provided of ray tracing simulations characterizing both phase and amplitude effects at frequencies from 0.5 to 17 GHz and axial positions from 0.25 m to 1.5 m. The results correlate well with known data.

1•Introduction

Modern high performance space electric propulsion systems, such as the SPT-100 Hall thruster, are currently being tested and considered for use aboard next generation spacecraft for such applications as North-South station keeping, repositioning, and orbit transfer due to their high thrust efficiency and nearly optimal specific impulse (I_{sp} , s) [1]. The advantage of using a Stationary Plasma Thruster (SPT) in these satellite missions is increased efficiency of propellant mass utilization resulting in an increase in satellite payload mass for a fixed launch mass. However, consideration must be given to possible interactions of the thruster's dense, high-speed plasma plume with satellite electromagnetic systems used for communication, navigation, and remote-sensing. Therefore, the effect of the SPT on satellite sub-systems must be established. (See Table 1 for general plasma parameter of the thruster.)

Here, we consider the interactions of an electromagnetic (EM) signal with a dense, non-uniform, highly directed mesosonic plume of plasma. It is well known that plasmas interact with EM signals [2-4] by altering the phase, amplitude, direction, and power spectral density of a transmitted signal such as described in Equation 1:

$$E = A[1 + m_{amp}(t)] \times \cos[k(r)r - (\omega - m_{freq}(t))t - m_{phase}(t)] \quad (1)$$

where A is the electric field amplitude (V/m), k is the positionally dependent wavenumber (m^{-1}), r is the position (m), ω is the angular frequency (radians s^{-1}), t is time (s), and m_{amp} , m_{freq} , and m_{phase} are modulation coefficients for amplitude, frequency, and phase, respectively. The plume-signal interaction is determined by the electromagnetic dispersion relation, which is primarily dependent on electron number density and the gradients of electron number density (where both can be time varying in the SPT plume). The plasma plume of a SPT can, in general, impact the amplitude, frequency, and phase of an electromagnetic signal. Amplitude and phase noise are produced by electron density oscillations in the SPT plume. However, experimental measurements indicate that the plume does not significantly alter the frequency component. In order to assess any possible degradation to particular electromagnetic systems (i.e., signal to noise degradation affecting data rates or signal accuracy), modification of these basic parameters must be assessed either experimentally or through validated computer models.

Parameter	Value
Electron Density	10^{15} to $10^{17} m^{-3}$
Discharge Voltage	300 V
Discharge Current	4.5 A
Thrust	85 mN
Axial Velocity	15 km/s
Percent Ionization	>95 %
Electron Temperature	2 to 4 eV
Ion Temperature	0.1 eV
Collision Frequency	$7 \cdot 10^5 s^{-1}$
Dominant Noise Frequency	26 kHz

Table 1: SPT Nominal Parameter Values

Previous investigations of the SPT have partially characterized the impact to electromagnetic signals. These studies characterized the phase noise and power spectral density at a number of frequencies between 2.6 GHz and 17 GHz [5-8] and the amplitude attenuation due to beam spreading was measured at 17 GHz [8]. These measurements provide direct indication of the plume impact on phase, amplitude, and power spectral density and can also help validate computer simulations. The simulations described here use electromagnetic signals to describe the modification of the signal as it propagates through the plume. The technique uses electron number density models [5,8] with a temporal density model [5] to simulate the phase oscillations produced by the thruster. Previous studies have modeled the phase noise produced by the plume, but the work described here and by Ohler [8] also estimate the magnitude of the amplitude noise produced by the plume.

Initially, the ray tracing method is reviewed as relevant to this work. Then, a physical simulation scenario is described which corresponds to previously reported experimental measurements. The ray tracing technique is applied to the physical scenario to find the attenuation and phase shift and then amplitude and phase modulation. In all cases, the simulations compare well with previous measurements. Finally, the technique is applied to a range of frequencies in order to determine general trends for plume impact to electromagnetic propagation.

2• Simulation Methodology

Ray tracing is an extremely useful tool for predicting high frequency electromagnetic transmission characteristics [9-11]. This section first reviews the ray tracing technique and suggests a source of amplitude modulation then describes the physical simulation scenario.

Ray Tracing Fundamentals

Ray tracing is a computer simulation technique which utilizes the geometric optics approximation to predict the progression of an electromagnetic field in a slowly varying media [11]. Ray tracing individually tracks the amplitude, phase, and ray path of the electromagnetic fields. The attenuation and phase of the signal are predicted by integrating the wave number (Equation 2A) along the ray path. The attenuation due to inelastic collisions in the plasma is predicted through the imaginary part of the wave number which is negligible here for the SPT-100 plume [8] and the phase is tracked (Equation 3) by using the real part of the wave number.

$$k(\vec{r}, t) = \frac{\omega}{c} \sqrt{1 - \frac{\omega_p^2(\vec{r}, t)}{\omega^2}} = \omega \sqrt{\mu_o \epsilon_o \epsilon_r(\vec{r}, t)} \quad (2a)$$

$$\omega_p^2(\vec{r}, t) = \frac{n_e(\vec{r}, t) e^2}{\epsilon_o m_e} \quad (2b)$$

$$\phi_2(s_2) - \phi_1(s_1) = \int_{s_1}^{s_2} k(\vec{r}, t) ds \quad (3)$$

In these equations c is the speed of light (m/s), ω_p is the radial plasma frequency ($radians/s$), μ_o is the free-space permeability (H/m), ϵ_o is the free-space permittivity (F/m) m_e is electron mass (kg), ϵ_r is the relative permittivity, n_e is the electron density (m^{-3}), e is the charge of an electron (C), m_e is the mass of an electron (kg), ϕ is the phase of a wave ($radians$), and s is the position of a wave (m).

The ray path follows the gradients of the electron density:

$$\frac{\partial}{\partial s} [\sqrt{\epsilon_r(\vec{r}, t)} \hat{s}] = \nabla \sqrt{\epsilon_r(\vec{r}, t)} \quad (4)$$

where the relative permittivity is related to the electron number density through Equations 2a and 2b.

Power Prediction Using Ray Tracing

Using ray tracing, the power density is found through the conservation of energy. The total power in a single ray is constant since the imaginary part of the wave number is minimal [8]; therefore, reduction in power density is attributed only to beam spreading due to refractive effects. This is quantified by tracking the power of a ray tube defined by several individual rays as in Figure 1. The ray tube cross-sectional area varies proportionally with the degree of refraction and the reduction in power is proportional to the ratio of the area at a reference point (e.g. transmitter antenna) to the area at an observation point (e.g. receiver antenna):

$$S_{rec} = \frac{A_{trans}}{A_{rec}} S_{trans} \quad (5)$$

where A_{trans} and A_{rec} are the areas of the transmitted and received rays (m^2) and S_{rec} and S_{trans} are the power densities of the transmitted and received rays (m^2).

Using these basic equations and a temporal and spatial density model [5, 8] the phase change, ray path, and power density reduction (attenuation) are predicted for a wave traversing the plume of an SPT. The phase shift and noise have been experimentally measured [8] and also simulated using a temporal plume model [5]. The ray path divergence has been demonstrated through measurement of signal attenuation [8]. In this work, amplitude modulation due to variable attenuation is modeled through ray tracing simulations of a Ku-band antenna using a temporal plume model.

Physical Simulation Scenario

The ray tracing analysis is applied to transmission paths in a plane orthogonal to the flow of plasma, 0.15 m from the exit plane of the thruster, where the center of the antenna intersects the axis of the thruster (see Figure 2). The two antennas are moved in unison across the plasma. This axial distance is chosen to provide comparison with previous measurements with Ku-band horn antennas operating at 17 GHz [8]. The computer model simulates the coupling between the two antennas through a standard Gaussian distribution, FN , for the antenna beam patterns,

$$FN = \frac{1}{\sqrt{2\pi}\sigma} \exp \left[-\frac{1}{2} \left(\frac{x}{\sigma} \right)^2 \right] \quad (6)$$

with standard deviation, σ , of 0.024 m [12] and where x is the position in the antenna aperture (m). The combined transmit and receive antenna system is represented in Eq. 6. In order to separately apply the transmit and receive effects, the square root of FN is used later in Eq. 10.

The relative permittivity is found from electron density measurements of an SPT-100 operating at nominal conditions of 300 V, 4.5 A, and 5.8 mg/s of xenon. The density model is the product of a static model and a temporal model. The static density is estimated

through a weighted average of two models, the first more accurate close the thruster and the second more accurate at the farther simulation positions. The near plume model is given by Equation 7 [8] where r (m) and θ (radius) are shown in Figure 2:

$$n_{static}(r, \theta) = C_1 \exp\left(-\left(\frac{r \sin \theta}{C_2}\right)^2\right) + \frac{C_3}{r^2} \exp\left(-\frac{\theta}{C_4}\right) \quad (m^{-3}) \quad (7)$$

$C_1 = 4.7 \times 10^{16} \text{ m}^{-3}$, $C_2 = 0.073 \text{ m}$,
 $C_3 = 1.3 \times 10^{15} \text{ m}^{-1}$, $C_4 = 1.1 \text{ rad}$.

The far plume model is given by Equation:

$$n_{static}(r, \theta) = \frac{n_o \exp\left\{-[\lambda(1 - \cos \theta)]^n\right\}}{r^2 \cos^2 \theta} \quad (m^{-3}) \quad (8)$$

$n_o = 10^{16} \text{ m}^{-1}$, $\lambda = 50$, $n = 0.6$.

The temporal density (n_{temp} , unitless) models is given by Equation 9 [5]:

$$n_{temp}(\bar{r}, t) = 1 - m_{noise} \cos(\omega_{noise} t - k_{noise} \bar{r}) \quad (9)$$

$$m_{noise} = 0.12, \omega_{noise} = 2\pi \times 26 \times 10^3 \text{ rad/sec}, k_{noise} = 10.9.$$

In both models the plume is assumed cylindrically symmetric (constant through all angles of ϕ). The density oscillation frequency is ideally represented as the entire frequency spectrum of the thruster; however, for simplicity in demonstration of the amplitude modulation the dominant oscillation frequency (26 kHz) is used to represent the density oscillations. This assumption provides worst case results for noise produced by the plume.

3• Static Simulations to Find Attenuation and Phase Shift

Our ray tracing method utilizes a combined static and temporal model of the SPT plume. In the simulations, the ray tubes bend (Figure 3) slightly away from the receiver antenna producing small attenuation (due to refraction and not absorption); however, at lower frequencies the attenuation is more severe as will be shown later in Section 5. The performance of the antenna system is predicted for a number of transmission paths across the plume. Each transmission path is evaluated for the effect on attenuation and phase. In order to find the attenuation and phase effected, a simulated plane wave is propagated from the transmitter antenna to the receiver. The plane wave is discretized into many rays each of which has an associated phase and power. The attenuation and phase is found by using a weighted summation of rays (which are traced across the plume) that are coincident with the antenna aperture (Eq. 10).

$$P_{ant} = \frac{\left| \sum_{N=1}^{N_{max}} \sqrt{w l_{pl}(N)} [FN(x_{pl}(N))]^{1/2} [FN(x_{nopl}(N))]^{1/2} \left(\frac{l_{nopl}(N)}{l_{pl}(N)}\right)^{1/2} e^{j\Delta\phi_R(N)} e^{j\phi_{nopl}(N)} \right|^2}{\left| \sum_{N=1}^{N_{max}} \sqrt{w l_{nopl}(N)} [FN(x_{nopl}(N))] e^{j\phi_{nopl}(N)} \right|^{1/2}} \quad (10a)$$

$$\phi_{ant} = \text{angle} \left\{ \sum_{N=1}^{N_{\max}} \sqrt{wl_{pl}(N)} [FN(x_{pl}(N))]^{1/2} [PN(x_{nopl}(N))]^{1/2} \left(\frac{l_{nopl}(N)}{l_{pl}(N)} \right)^{1/2} e^{j\Delta\phi_R(N)} e^{j\phi_{nopl}(N)} \right\} \\ - \text{angle} \left\{ \sum_{N=1}^{N_{\max}} \sqrt{wl_{nopl}(N)} [FN(x_{nopl}(N))] e^{j\phi_{nopl}(N)} \right\} \quad (10b)$$

Eq. 10a and 10b use the superposition of each ray's amplitude and phase to produce the total amplitude and phase of the antenna at a given transmission path. The variable, N , represents a series of rays. The variables are found through ray tracing for each of the N rays. Each ray is defined by ϕ , x , w , and l . $\phi_R(N)$ is the phase of a given ray with the plasma present relative to $\phi_{nopl}(N)$ which is the phase of a ray without the plasma present relative to the starting phase of the ray, $x_{pl}(N)$ and $x_{nopl}(N)$ are the positions of the rays with and without the plasma present relative to the antenna coordinate system utilized for the antenna beam distribution. The variable w is the width of the beam along the axis of the plume which is approximately constant due to the much lower density gradients in that direction. The variables $l_{pl}(N)$ and $l_{nopl}(N)$ are beam dimensions orthogonal to both w and the beam direction both with and without the plasma present. These two quantities are found by using the beam positions $x_{pl}(N)$ and $x_{nopl}(N)$ and using half the distance between beam centers as the beam width. The FN which was defined earlier weights each ray by the position of the ray in the antenna beam.

The attenuation and phase is shown in Figure 4 and 5 for two simulated situations: a single ray tube where each antenna point is represented by the center ray and the full system simulation where the antenna beam function, FN , is utilized to determine each antenna performance. The individual ray tubes results exhibit slight noise which is attributed to the numerical aspects of ray sampling and step size. In both the attenuation and phase, the plots show the expected relationship between the rays and the total antenna function. The amplitude of the simulated ray tubes are actually predicted to have a slight power gain on the edge of the plume where the ray density is higher than in free space.

Experimental data is also plotted in Figures 4 and 5 for comparable conditions. For both amplitude and phase, the simulation tends to over predict the effect of the plume on the transmitted signal when compared to the experimental data (5% for attenuation and 30% for phase). These differences can be attributed to the inherent limitations of the ray tracing technique. Two simulation limitations are the finite ray sampling and step size both having greater importance at smaller wavelengths where the error tends to affect the phase more than the amplitude. Two other limitations are the electron density model which is known to be accurate only to $\pm 20\%$ and the limited accuracy of the antenna distribution function. Given these factors, the difference between the ray tracing simulations and the experimental measurements are reasonable.

4• Temporal Simulations to Quantify Amplitude and Phase Modulation

When the attenuation level varies over time due to oscillations in density, then amplitude noise or modulation is produced on the transmitted signal (Figure 6). The greatest simulated attenuation is -1.92 dB and least is -1.46 dB. The variation of ± 0.23 corresponds to the variation in experimental data in Figure 4. The simulations have been implemented with a 26 kHz plasma oscillation which is the dominant frequency

component; however, amplitude variation of smaller magnitude exists for other frequencies.

The ray tracing simulation indicates amplitude modulation at 26 kHz which is described mathematically for the transmitted signal in Equation 1. In that equation the modulation factor, m_{amp} , is represented by $|m_{\text{amp}}|\cos(\omega_{\text{oscill}}t)$ where ω_{oscill} is the radial frequency of the density oscillation and $|m_{\text{amp}}|$ is the peak-to-peak signal amplitude normalized by the mean amplitude value. $|m_{\text{amp}}|$ is found to be 0.053 (note: this is unitless, not dB) and the mean attenuation is -1.68 dB. The corresponding phase variation (Figure 7) is found through similar methods where m_{phase} is $|m_{\text{phase}}|\cos(\omega_{\text{oscill}}t)$. Here, $|m_{\text{phase}}|$ is the phase variation relative to the mean phase shift ($|m_{\text{phase}}| = 0.094 \text{ rad } (5.4^\circ)$), and the mean phase shift is -0.96 rad (-55°) (relative to transmission through a vacuum).

The power spectral density is a useful description for determining the quality of an electromagnetic signal. Ideally, the carrier power would be contained in a narrow bandwidth relative to the modulation and the noise power would be near the thermal noise floor ($\ll -100 \text{ dB}$) for a wide range of frequency offsets. The power spectral density is calculated for a 17 GHz signal transmitted through the plume 0.15 m from the exit plane using modulation parameters from the ray tracing simulation (Figure 8a).

The plasma oscillations produce 26 kHz harmonics where the first harmonic is produced through a combination of the amplitude and phase modulation. In this particular case, the amplitude modulation produces 3 dB more power in the first harmonic than with the phase modulation alone. The first harmonic compares well (within 2 dB) with the measured results in Figure 8b; however, the simulation under predicts the measured second harmonic. In addition, the broad band noise exhibited in the measurements are not predicted by the single frequency oscillation model. These similarities and differences are common throughout other comparisons of the simulations and experiment. The differences between simulations and experiments would decrease with a more accurate model of the frequency spectrum of plume oscillations.

Additionally, experimental measurements at 1.575 GHz [13] produced a number of facts useful for understanding the limitations and implications of the ray tracing simulation. First, the independence of attenuation and transmission angle with respect to the thruster axis provides flexibility to use the amplitude simulations for any path crossing a similar axial position. Second, the 1.575 GHz data follows trends of lower frequency simulations despite the failure of the simulation at this frequency. Third, the power spectral density measurements indicates significant modulation by the plasma as would be expected at lower frequency and is predicted by simulations as will be demonstrated in the next section.

In summary, density oscillations in the plume produce both amplitude and phase modulation. This evaluation demonstrated the mechanism of amplitude modulation by the plume through ray tracing simulations. Additionally, the simulations compared well to phase, amplitude, and power spectral density measurements for a similar experimental situation.

5• Discussion

We can use our verified ray tracing algorithm described above to establish general trends in the modification of both amplitude and phase to a transmitted signal over a wide range of frequencies and transmission paths. The theoretical limitation of ray tracing can also be used as a boundary for significant power loss and compared to simulations for a range of

positions and frequencies. Here, we describe simulations for 0.25, 0.5, 1, and 1.5 m from the thruster exit plane and for transmitted signals covering 0.5 to 17 GHz. All of the summary simulations are calculated for the plume effect on a single ray in order to make the results more general. This implementation produces worst case results for transmission across the plume since the center ray of the antenna beam experiences the greatest impact. The attenuation simulations are completed for a wide range of situations (Figures 9 and 10). The attenuation indicates a sharp increase in power loss at the lower frequencies, but also a quick reduction in plume impact with increasing distance. The results show less than 3 dB attenuation for frequencies greater than 10 GHz except for the very closest positions. The modulation coefficient follows similar trends indicating up to 25% modulation at the closest measurement point at 3 GHz and also indicating less than 5% modulation for all distances at 17 GHz; however, as was demonstrated earlier with the 17 GHz simulation, even small modulation coefficients produce significant increases in the noise power.

The phase simulations are completed over the same spatial and frequency simulations set as the attenuation (Figures 11 and 12). The phase is more sensitive to simulation error than the amplitude as the frequency approaches the theoretical limit of geometrical optics; hence, the lower frequency values at the closest simulation point did not produce reliable results. Overall, the general trends are similar to the attenuation simulations; however, the rate of decline in the signal impact is slower as the frequency or position increases. Again, even a small modulation factor can produce significant increase in the noise power.

These simulations are used in addition to simulations at lower frequencies to find the 3 dB and 10 dB contours across a range of positions and frequencies. In addition the theoretical limit of geometric optics provides another indicator of significant propagation impact (greater than 10 dB of loss). The limit of geometrical optics, Equation 11 [11], states the wavelength (λ_o) must be much smaller than scale length of changes in the wave number or in this case the permittivity (ϵ_r) which directly relates to the density.

$$\lambda_o \ll \frac{\epsilon_r}{\frac{\partial}{\partial \text{path}} \epsilon_r} \quad (11)$$

This condition implies that if the density changes quickly or for example the plasma frequency density is approached, the ray will bend faster than ray tracing can reliably predict.

The condition for validity of the ray tracing analysis is evaluated for a geometry similar to Figure 2 for a range of axial positions. For any given position the failure point for the highest frequency is along the thruster axis. The 3 dB contour, 10 dB contour, and geometric optics limit contour are shown in Figure 13.

The analysis utilized a general ray tracing analysis to simulate phase shift, attenuation, phase modulation, and amplitude modulation. The simulations compare well with measurements of propagation modification by a stationary plasma thruster. The simulation covered a broad frequency range (500 MHz to 17 GHz) and demonstrated that at the lower frequencies significant signal modification can occur.

These results provide the basis for drawing broader conclusions concerning transmissions across the plume. At frequencies of general interest for electromagnetic transmission, the plume acts to refract an electromagnetic wave, but it does not absorb the energy through collisional or Landau damping. As would be expected, the plume effect on transmission

decreases at increasing distances and increases for lower frequencies. Additionally, these results provide a worst case scenario for transmission when compared to other antenna configurations. To estimate the performance impact for an antenna configuration where one antenna is close to the plume and the other antenna is at a distance, the axial distance where the transmission path of interest crosses the thruster axis can be used to estimate the system impact due to the plume using the information provided in this evaluation.

Acknowledgments

Thanks also goes to C. Nelson for his work on the ray tracing simulations and to M. Day of Space Systems/Loral for use of the SPT-100 Engine.

Section II References

1. Myers, R.M. and D.H. Manzella, Stationary Plasma Thruster Plume Characteristics, paper 93-096 presented at *23rd International Electric Propulsion Conference*, Seattle, WA, 1993.
2. Heald, C.B. and M.A. Wharton, *Plasma Diagnostics With Microwaves*, John Wiley and Sons, Inc., New York, 1965, pp. 4-12.
3. Sheffield, J., *Plasma Scattering of Electromagnetic Radiation*, Academic Press, Inc., New York, 1975.
4. Stix, T.H., *Waves in Plasmas*, American Institute of Physics, New York, 1992, pp. 25-46.
5. Dickens, J.C., M. Kristiansen, and E. O'Hair, Plume Model of Hall Effect Plasma Thrusters with Temporal Consideration, paper 95-171 presented at *IEPC*, Moscow, Russia, 1995.
6. Dickens, J., *et al.*, Impact of Hall Thrusters on Communication System Phase Noise, paper AIAA 95-2929 presented at *31st AIAA/ASME/SAE/ASEE Joint Propulsion Conference and Exhibit*, San Diego, CA, 1995.
7. Ohler, S.G., Ph.D. Thesis, *Space Electric Propulsion Plasma Characterization Using Microwave and Ion Acoustic Wave Propagation*, University of Michigan, 1996, pp. 60-78.
8. Ohler, S., B. Gilchrist, and A. Gallimore, Microwave Plume Measurements of an SPT-100 Using Xenon and a Laboratory Model SPT Using Krypton, paper AIAA 95-2931 presented at *31st AIAA/ASME/SAE/ASEE Joint Propulsion Conference and Exhibit*, San Diego, CA, 1995.
9. Ling, H., *et al.*, Effect of an Arcjet Plume on Satellite Reflector Performance, *IEEE Transaction on Antennas and Propagation*, **39**, , 9, 1412-1419, 1991.
10. Kim, H. and H. Ling, High Frequency Electromagnetic Scattering From an Inhomogeneous Dielectric Body By Ray Tracing, paper presented at *IEEE Antennas and Propagation Society Symposium*, Ontario, Canada, 1991.
11. Born, M. and E. Wolf, *Principles of Optics*, Pergamon Press Book, New York, 1964, pg 121.
12. Ohler, S.G., B.E. Gilchrist, and A.D. Gallimore, Non-intrusive electron number density measurements in the plume of a 1 KW arcjet using a modern microwave interferometer, *IEEE Transactions on Plasma Science*, **23**, 3, 428-435, 1995.
13. Ohler, S.G., *et al.*, RF Signal Impact Study of an SPT, paper AIAA 96-2706 presented at *32nd Joint Propulsion Conference*, Lake Buena Vista, FL, 1996.

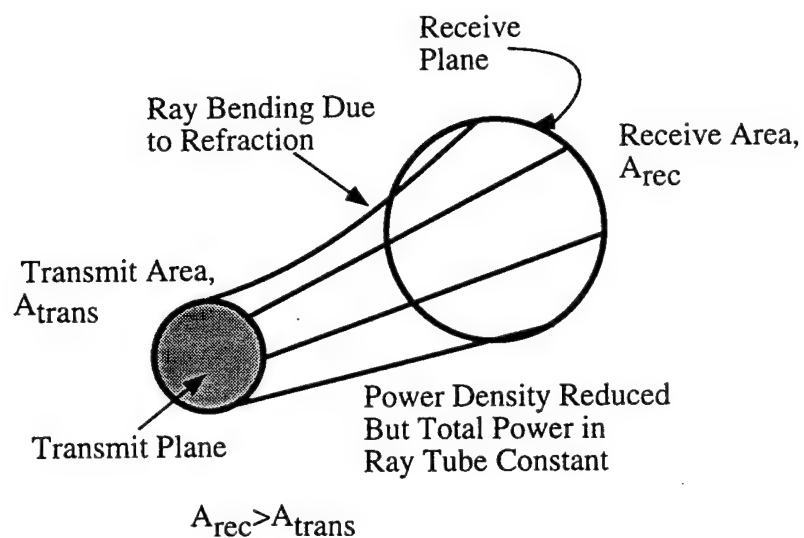


Figure 1. Ray Tube Analysis Produces the Change in Power Density

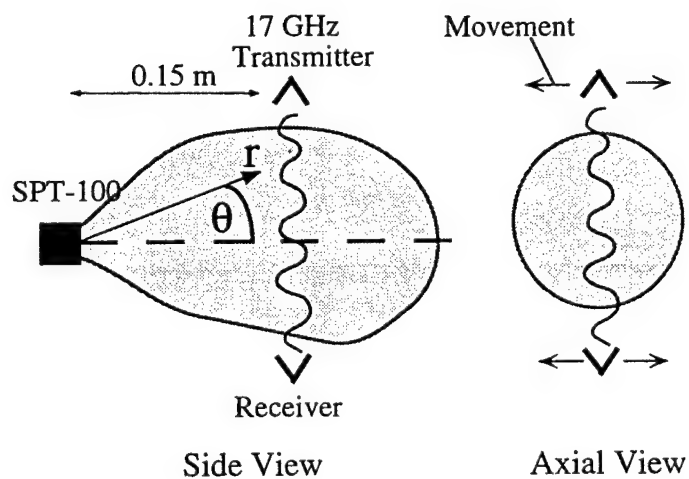


Figure 2. Physical System for Ray Trace Modeling, θ and r are in a spherical coordinate system, x is the antenna aperture coordinate.

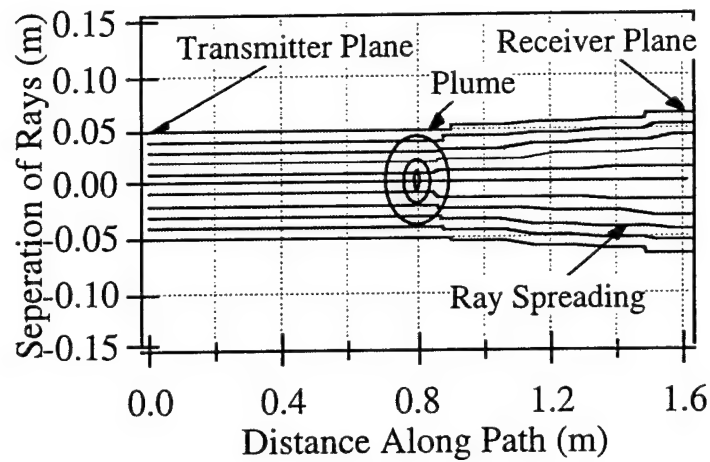


Figure 3. Ray Paths of the Simulated Antenna for a Single Time Step (0.15 m, 17 GHz), lines represent ray tubes.

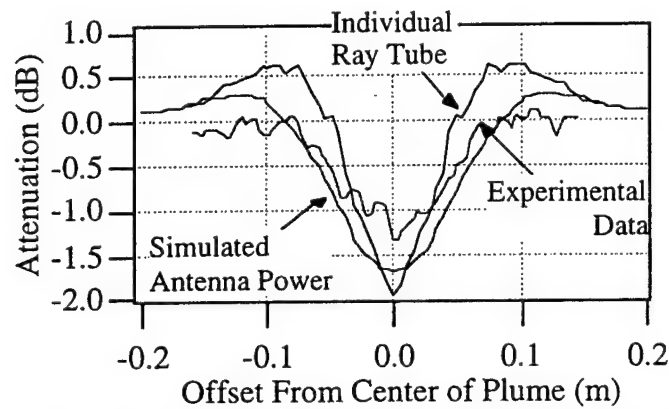


Figure 4. Power Change Due to Plasma for Individual Ray Tubes, Simulated Antenna, and Experimental Results; 0.15 m downstream, 17 GHz.

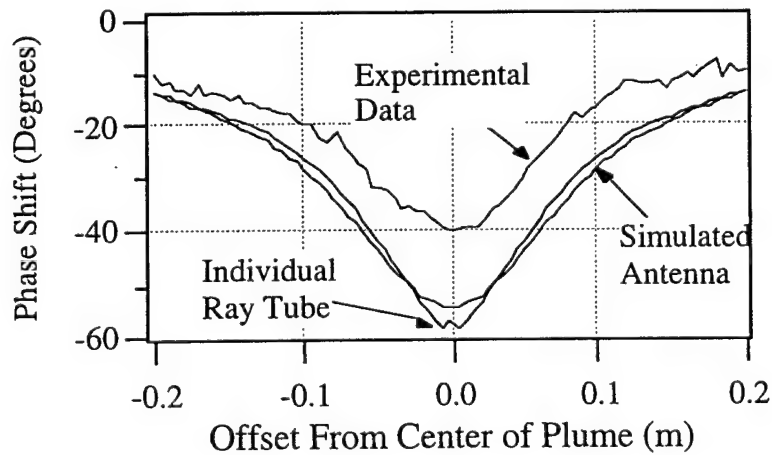


Figure 5. Phase Shift Due to Plasma for Ray Tubes, Simulated Antenna, and Experimental Results; 0.15 m downstream, 17 GHz.

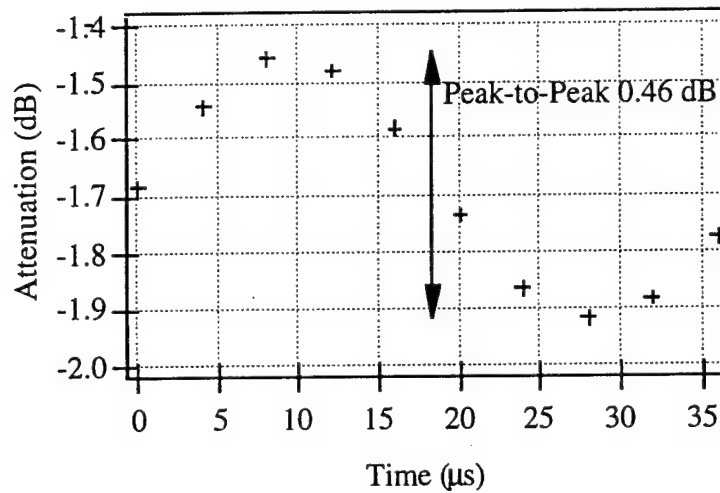


Figure 6. Simulated Amplitude Variation Over Time for a 17 GHz Signal Transmitted Through the Plume 0.15 m from the Exit Plane (Relative to Power With no Plume Present) assuming a modulation frequency of 26 kHz.

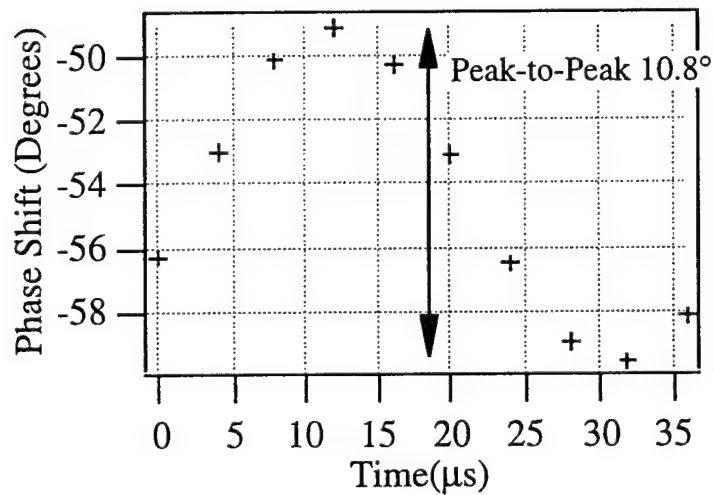
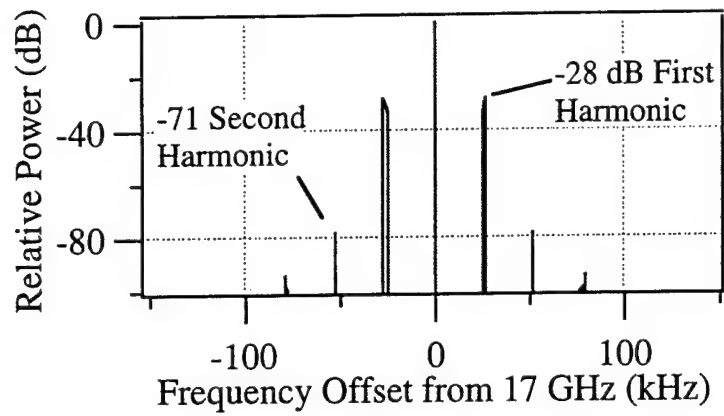
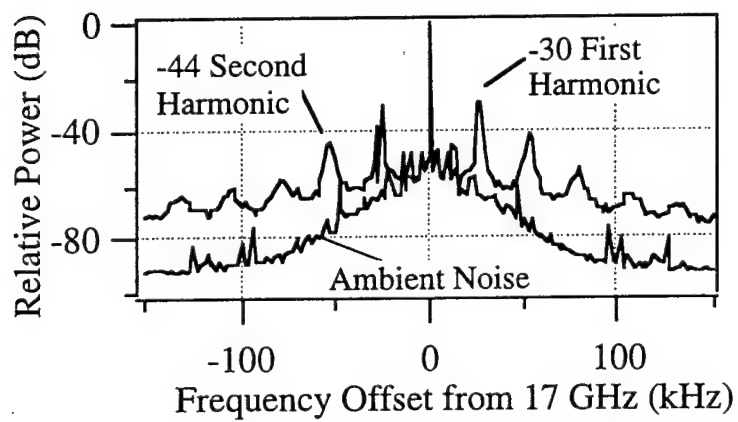


Figure 7. Simulated Phase Variation Over Time for a 17 GHz Signal Transmitted Through the Plume 0.15 m from the Exit Plane (Relative to Power With no Plume Present).



(a)



(b)

Figure 8. Comparison of the Measured and Simulated Power Spectral Density of a 17 GHz Signal Transmitted Across the Plume 0.15 m from the Exit Plane. (a) Simulated Effect of Density Oscillations. (b) Measured Power Spectral Density

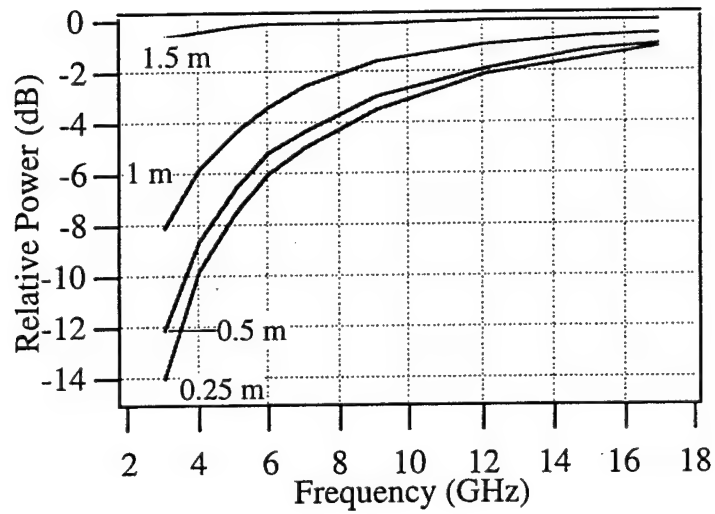


Figure 9. Simulated Attenuation of an Electromagnetic Signal Transmitted Through an SPT Plume.

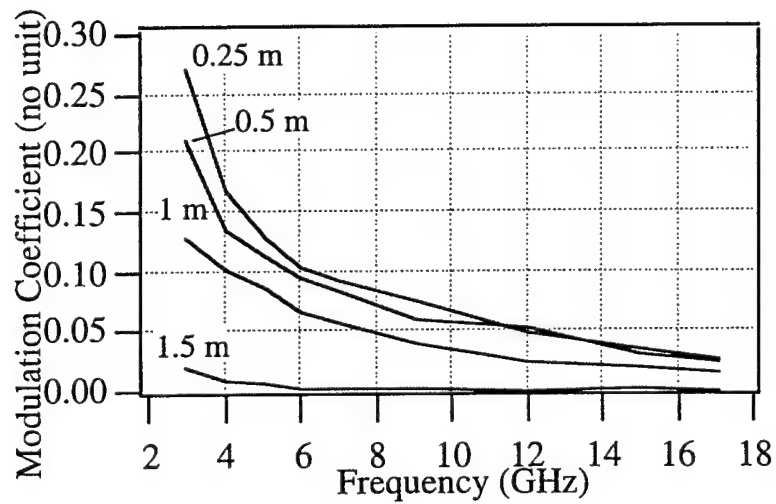


Figure 10. Simulated Amplitude Modulation Coefficient of an Electromagnetic Signal Transmitted Through an SPT Plume

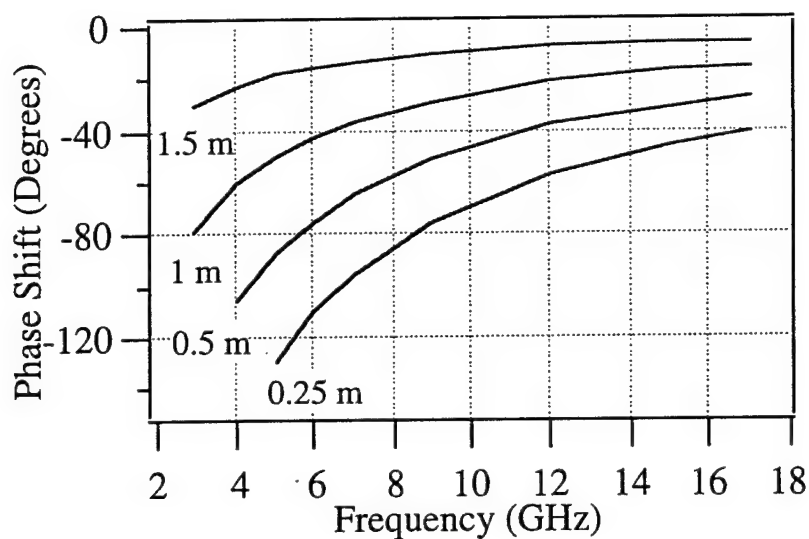


Figure 11. Simulated Phase Shift of an Electromagnetic Signal Transmitted Through an SPT Plume (Referenced to the Phase Shift with no Plasma).

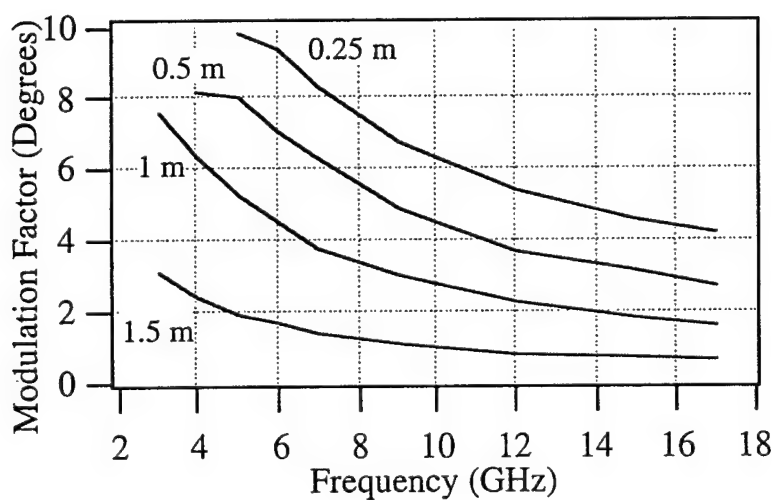


Figure 12. Simulated Phase Modulation Factor of an Electromagnetic Signal Transmitted Through an SPT Plume.

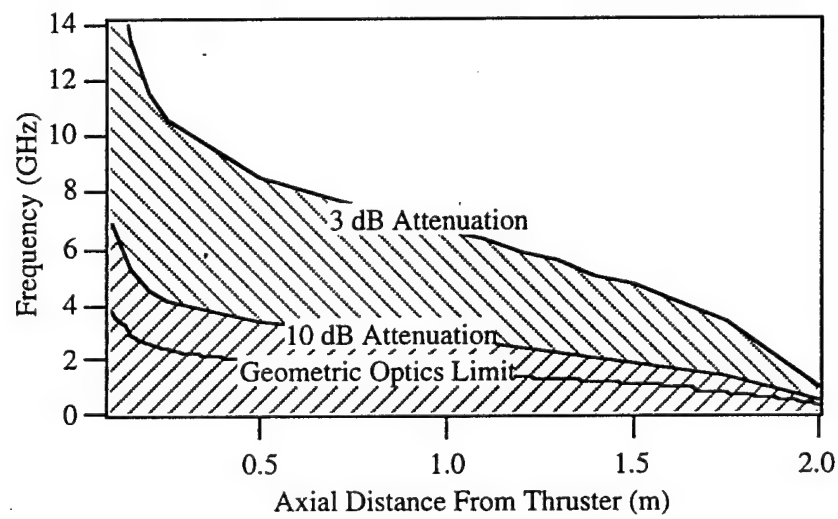


Figure 13. Theoretical Frequency Limit of Geometric Optics With Respect to Transmitting Across the Plume at a Given Axial Distance From the Thruster Exit Plane.

SECTION III: MICROWAVE PLUME MEASUREMENTS OF A CLOSED DRIFT HALL THRUSTER

Shawn Ohler*, Brian E. Gilchrist, and Alec Gallimore
University of Michigan
Ann Arbor, MI

Abstract

The plasma plume from a closed drift hall thruster has been characterized using a 17-GHz microwave diagnostic system. Electron number density profiles are obtained throughout the thruster plume via differential phase measurements. A functional model of plasma density has been developed combining a near-field Gaussian beam term and a far-field point source expansion term. An outcome of this work is a mapping of the transition region between the near- and far-field plume. An indication of slight plume asymmetry is obtained by evaluating total integrated density measurements along rays emanating from the thruster. Additional have determined the plasma plume effect on attenuation and spectral characteristics of a wave transmitted through the plume. The attenuation was small, with slightly over 2 dB loss at 0.09 m along the thruster axis. However, ray tracing attenuation modeling based on plasma density profiles indicates a greater effect for lower frequency operation. The spectral data of the signal transmitted through the plume exhibited clear 26-kHz harmonic sidebands and added broadband noise. Estimates of potential impact to communication and other electromagnetic satellite systems can be obtained directly from the measurements and from the electron number density distribution models derived from the measurements.

Nomenclature

c	=	Speed of Light (m/s)
e	=	Electron charge (C)
f	=	Frequency (Hz)
$FN(x)$	=	Gaussian distribution function of the antennas
m_e	=	Electron mass (kg)
$n(r)$	=	Local electron density in the plume (m^{-3})
n_c	=	$(f/8.98)^2$, Critical or cutoff density (m^{-3})
q	=	Spatial frequency (m^{-1})
r	=	Radial position from thruster (m)
R	=	Maximum radial extent of the plume for Abel analysis (m)
x	=	Spatial position along measurement axis (m)
ϵ_0	=	Permittivity of free space (F/m)
ϕ	=	Phase angle (radians)
λ_i	=	Wavelength (m)
ρ	=	Radial position from thruster axis (m)
θ	=	Angle from thruster axis (radians)
ω	=	Radial frequency (radians)

* Currently Technical Staff, Lincoln Laboratory, 244 Wood St., Lexington, MA 02173, member AIAA

Introduction

Closed drift electric propulsion are currently being tested and considered for use aboard next generation spacecraft for North-South stationkeeping, repositioning, and orbit transfer. Closed drift thrusters (CDTs) are attractive in these roles due to their high thruster efficiency and Isp of 1300 to 2700 seconds, optimal for many of these missions [1]. Understanding possible plume effects on electromagnetic signals is important for evaluating spacecraft integration issues. Using a large vacuum facility with proper placement of antennas, it is possible to characterize directly the plasma effects on electromagnetic signal phase, amplitude, and spectral content. These same measurements can also be used to measure plume plasma density non-intrusively which data [2] can be used as the basis for predictive models of effects on electromagnetic signals at various frequencies.

Previous CDT studies have reported on various aspects of their operation and spacecraft integration [2-7]. However, only limited measurements of plume impact on electromagnetic signals have been given [2,7]. A number of studies have reported on plume parameters at limited locations such as electron number density, electron temperature, ion velocity, and ion energy [1,9-11].

Characterization of the plume through microwave diagnostics provides a non-intrusive method to accurately characterize the plasma. The use of microwaves avoids local perturbations of the flow and probe heating inherent in intrusive diagnostics close to the thruster. In addition, a microwave diagnostic system provides a direct measure of communication issues such as power loss and noise increase.

Here, we report on differential phase mapping measurements which lead to the determination of electron number density. Also reported are power spectral density results which will expand on previous spectral measurements at lower frequencies. Finally, direct measurement of attenuation will provide the first reported direct experimental indication of power loss.

The following section reviews the theory of microwave interferometry, the Abel inversion technique as applied to our situation, and the experimental apparatus including the thrusters, vacuum chamber, and positioning system in addition to the microwave measurement system. In Section 3, experimental results are presented. Section 4 reports on a functional model of the plume plasma density. Plume asymmetry is estimated, and measurement accuracy of the experimental system assessed. Finally, Section 5 contains a summary of results and accomplishments.

Experimental System and Theory of Operation

All experiments reported were performed at the Plasmadynamics and Electric Propulsion Laboratory (PEPL) at the University of Michigan in a 9-m-long by 6-m-diameter stainless-steel vacuum chamber. The facility is evacuated by six 0.81-m-diameter diffusion pumps each rated at 32,000 l/s on nitrogen (with water-cooled cold traps), backed by two 2,000 cfm blowers, and four 400 cfm mechanical pumps. These pumps give the facility a measured overall pumping speed for xenon of over 27,000 l/s. Plume diagnostics are performed through the use of a probe positioning system. The table contains two rotary platforms on a linear stage with 1.5 m of travel in the radial direction on a 0.9 m travel axial stage. The entire probe positioning system is mounted on a movable platform to allow for measurements to be made throughout the chamber. A more complete description of the experimental facilities can be found in Gallimore, et al. [11].

A diagram of the Hall thruster is shown in Fig. 1. It is a commercial grade model SPT-100 built by the Russian Fakel Enterprises and on loan from Space System/Loral and previously tested by NASA Lewis [1,4, 8-10] and the Jet Propulsion Laboratory [5]. The

inner diameter of the outer ceramic ring is 0.1 m and the cathodes are LaB₆ thermionic emitters. A more complete description of the thruster can be found in refs. [4,5].

The microwave system (Fig. 2) used for these measurements has been designed to work in the Ku band (12-18 GHz) [13, 14]. Density measurements are taken using a 17 GHz signal transmitted through the plume of the thruster orthogonally to the thruster axis at a transmitted power of less than 0.1 milliwatts. The measurement system consists of a computer-controlled network analyzer connected to a microwave frequency conversion (both up converting and down converting) and amplification circuit and two lens-corrected horn antennas each with 7° to 8° beam widths. The antenna beam patterns are described by a Gaussian distribution function with a standard deviation of 0.024 m [14]. The positioning table moves the microwave system throughout the plume at a rate of 0.01 m/s. Measurement noise is a result of small vibrations of the measurement system while moving and the 20-dB power difference between the transmitted and received microwave signal. The total resulting phase noise is $\pm 2^\circ$ and the amplitude noise is ± 0.2 dB. The stability of the microwave system enables a straight forward differential comparison of attenuation and phase with and without the plasma present.

The measurement system provides three data. Differential phase and differential amplitude are obtained through the network analyzer transmission coefficients. The power spectral density is attained through using the network analyzer's transmitted signal and by recording the frequency spectrum on a spectrum analyzer from the received signal.

All of the measurements provide information concerning electromagnetic system impact. The phase shift measurements provide additional information related to the line-integrated plasma electron density through microwave interferometric analysis [14]. By making multiple measurements along a plane perpendicular to the thruster axis and assuming radial symmetry, the local electron density can be found using an Abel inversion technique [15-17].

The chordal phase measurements and their gradient in the measurement plane can be used according to the Abel inversion relation [15] to obtain radial electron density estimates throughout the radial plane. However, noise introduced by the derivative of raw data and the singularity at the integral end point can create difficulties in applying the inversion directly. Therefore, several methods have been used in the past to avoid these problems [14, 18]. In the analysis used in this study, an implementation of a low pass filter [19] coupled with a double transform of the Abel integral [20] reduces these computational issues. Specifically, the Abel integral is manipulated into a double transform; first a spatial Fourier transform followed by a Hankel transform:

$$n(\rho) = 2\lambda n_c \int_0^{+\infty} q J_0(2\pi\rho q) \int_{-\infty}^{+\infty} \phi \exp(-j2\pi xq) dx dq \quad (1)$$

Also, after performing the Fourier transform a low-pass filter can easily be implemented in the transform domain. Thus, data noise can be filtered in a straightforward manner with removal of the singularity.

Experimental Results

The SPT-100 was nominally operated at 300 V and 4.5 A discharge voltage and current, using xenon propellant at a flow rate of 5.5 mg/s through the anode and 0.29 mg/s through the hollow cathode. (A single flow control was available with 5% of the total flowing through the cathode.) In order to maintain the discharge current, the flow was

changed no more than 0.5 mg/s total flow. The tank pressure was maintained below 6×10^{-3} Pa (5×10^{-5} Torr) throughout the experiments.

Measurements of differential phase, differential amplitude, and power spectral density are presented. The phase measurements provide a direct indication of the electron density while the amplitude and spectral measurements indicate additional effects of the thruster plume on a microwave signal.

Electron Density Measurements

Differential phase measurements have been taken in parallel planes orthogonal to the thruster axis, and measurements were recorded every 0.005 m. The planes are located between 0.09 m and 0.90 m axially from the thruster exit plane. Along the axial direction, measurements were taken in 0.03 m increments from 0.09 m to 0.39 m and every 0.06 m farther out from the thruster. The spatial resolution along the thruster axis is limited to the sampling resolution. In the orthogonal direction, the measurements are sampled every 0.005 m; therefore, the antenna beam (~ 0.025 m) is the limit to spatial resolution in this direction. The higher spatial sampling aids in data analysis (however, this is not required for the Abel inversion). The absolute positional uncertainty is approximately ± 0.02 m and the relative uncertainty between measurement planes is approximately $\pm 2 \times 10^{-3}$ m.

In order to determine the local electron number density, the antenna pattern first is removed from the measurements via deconvolution using the calibration distribution function [14]. A digital low-pass boxcar filter then removes the high frequency noise from the measurement and deconvolution process. The filter cutoff frequency is chosen to minimize high frequency noise while maintaining the measurement features. The Abel inversion through the transform method then finds the local electron number density in the plume. Finally, for data analysis purposes, the data are transformed from a Cartesian coordinate system into a spherical coordinate system through linear interpolation. Figure 3 shows one set of phase data 0.09 m from the thruster exit plane overlaid with the resulting electron density distribution which is found through the above analysis method.

The results presented here are comparable to the previously reported results within the uncertainty of the measurements. Figure 4 shows electron density measurements at 0.30 m for both the microwave measurements and Langmuir probe data taken by Myers and Manzella [1]. The measurements reported here show a peak density of $6.2 \times 10^{16} \text{ m}^{-3}$ ($\pm 17\%$) and reduction by a factor of three along a similar contour at 21° off center line. Myers and Manzella report a peak density of $5.7 \times 10^{16} \text{ m}^{-3}$ (Langmuir probe accurate to $\pm 50\%$) decreasing by factor of three at 22° off center line for the SPT-100 at 0.30 m. The difference in measurements is well within the uncertainty expected of the separate measurements.

Attenuation Measurements

Signal power reduction has been explored since high peak density and density gradients exist which can refract on an electromagnetic signal. The SPT-100 plume produces a small degradation in the transmitted signal which is slightly over 2 dB of loss at the closest measurement point of 0.09 m. Beyond 0.24 m axially from the thruster and 0.05 m from the thruster axis, the loss is less than 1 dB. Figure 5 presents attenuation measurements for the SPT-100. The minimal reduction in power does not impact the phase measurements as greater than a 10 dB loss would be required to affect the microwave system resolution.

Power Spectral Density

The phase noise produced by the microwave system and the positioning system is $\pm 2^\circ$. It was expected that oscillations in the discharge current (nominally $\pm 50\%$) and the plasma found previously by Dickens [6] for the SPT-100 thruster might produce significant additional phase noise. Figure 6 shows the power spectral density for transmission through the plume 0.14 m from the exit plane of the SPT-100 compared with the power spectral density without the plasma plume. Measurement of the broadband noise show that the thruster raises the noise power by 5 to 25 dB (from -110 dBm) for offsets between 10 kHz and 1 MHz from the 17 GHz signal. In addition, coherent peaks in the frequency spectrum occur at 26 kHz harmonic sidebands with largest peaks at approximately -30 dB below the carrier.

Analysis of Results

Functional Model of Electron Density

We have developed a plume density model based on the density measurement using a combination of two functions that attempt to bridge the near- and far-field distributions. The near-field term treats the distribution as an ideal Gaussian beam, while the far-field term models the point source expansion of a plume [21, 22]. The following expression mathematically summarizes the plume model:

$$n(r) = C1 \cdot \exp\left(-\left(\frac{r \sin \theta}{C2}\right)^2\right) + \frac{C3}{r^2} \exp\left(-\frac{\theta}{C4}\right) \quad (2)$$

The $r \sin \theta$ term in the Gaussian exponential argument accounts for variations in the plane orthogonal to the thruster axis. The coefficients for the expression are obtained through a least squares minimization of the difference between the data and the model from 0.12 m radially out to 0.70 m and for angles 0 to 50° with respect to the thruster center line. Table 1 contains the coefficients for this expression used for the SPT-100.

Table 1: Coefficients of the Functional Model of Electron Density

C1	$4.7 \times 10^{16} \text{ m}^{-3}$
C2	0.073 m
C3	$1.3 \times 10^{15} \text{ m}^{-1}$
C4	1.1 rad

Figure 7 shows the close comparison of the model with the density measurements in the region where the coefficients were optimized. The slight variation in the measurements are representative of the typical thruster variation over time. The measurements shown in Fig. 7 were taken over approximately 30 minutes. In a test where the microwave system was held at a constant position the phase varied by 3° over a ten minute span. This indicates a variation of 7% in line-integrated electron density.

Figure 8 shows the density contour of the model. As would be expected, farther away from the thruster axis, the free expansion term matches the observed distribution. This model is valid within the measurement region from 0.12 to 0.90 m radially and out to at least 70° . It is expected that additional factors will need to be considered outside this region. For example, the first term is a constant as a function of r for $\theta = 0$. However,

clearly this term must decay at some distance depending on collisional effects and plasma neutralization.

Estimation of Asymmetry

The Abel integral depends on an assumption of radial symmetry; however, the SPT is known to exhibit a small asymmetry [8]. Since only a single cathode is placed to one side of the thruster (see Fig. 1), the primary asymmetry in the SPT thruster configuration is assumed to be caused by the cathode [8]. In the experiments, the cathode is in the horizontal direction and the measurements are in the vertical direction. An estimation of the asymmetry due to the cathode can be determined through comparison of the phase data from measurements on either side of the thruster axis when the cathode is placed entirely on one side.

The estimation of asymmetry is found by using the phase shift which measures the line-integrated plasma density along the transmission path. Summing the phase shift measurements along lines radially outward from the thruster gives an indication of the number of particles in a particular direction. By summing the phase data in the two half planes with and without the cathode, an asymmetry estimate can be made. The first step is to integrate the number of particles along distinct angular directions. Figure 9 shows the particle flow diagram for the thruster where the magnitude is a measure of the average number of particles per m per radian along a certain angular direction. By summing the particle number values on either side of the cathode, the off-axis particle vector for the thruster is estimated to be 1.3% of the total or 0.8° degrees away from the axis. Manzella [8] reports the thrust vector to be 2% of the total thrust. The thrust vector is an indication of particle flux (not just particle density), but the indication of asymmetry is similar. If all other asymmetry mechanisms produce less variation, then it is expected that the local density error for individual measurement sweeps will be less than 2% of the peak density along the thruster center line.

Comments on Attenuation and Power Spectral Density

While collisional damping sometimes occurs in plasmas, the collision frequency here is expected to be less than 10 MHz, and therefore much less than the 17 GHz transmission frequency. Thus, the primary cause for attenuation should be refraction effects in the plume. This is verified by applying a two dimensional ray tracing algorithm [23, 24] that uses the electron density model. Figure 10 shows the calculated ray paths through the plume and Fig. 11 overlays one of the attenuation sweeps with the ray tracing results. The traces in Fig. 10 are 0.15 m from the exit plane of the SPT. This not only confirms the expectation that the attenuation is due to refractive losses but verifies consistency with our electron density model.

Ray tracing calculations, 0.15 m from the thruster, were also done at 10 GHz and 6 GHz. The 10 GHz trial has shown greater than 3.5 dB peak loss while the 6 GHz loss is greater than 10 dB peak loss. Complete reflection of the signal (infinite attenuation) is achieved at the plasma frequency (2.8 GHz at 0.15 m from the thruster). The refraction of rays is so great that the ray tracing method is not valid for frequencies below 4.8 GHz at 0.15 m from the thruster. This could have significant impact on lower-frequency microwave signals such as the Global Positioning System (GPS) which transmits at 1.6 GHz.

The spectral measurements indicated a noise increase between 5 and 20 dB for offsets between 10 kHz and 1 MHz. The added noise power could be of concern for some radar and communications systems. However, the phase differential and amplitude differential measurements made here were not appreciably affected due to the narrow 3 kHz

bandwidth of the microwave system. As previously stated, the thruster produced additional phase noise of $\pm 0.5^\circ$ which is now attributed to the thruster broadband noise. The added phase noise is filtered along with the measurement system noise.

Error Analysis of Density Measurements

The total system measurement error is estimated by examining the individual sources of uncertainty within the measurement and the analysis phases. A basic model of the density based on the phase measurements is used in simulations to assess uncertainty. Each of the factors is varied individually to determine the effect on the final results. The percent difference in the peak electron density for a sweep is used as a figure of merit for the system. Uncertainty in position, phase reference, and filter cutoff in the Abel inversion analysis have all been evaluated by determining how each parameter uncertainty effects the final result. The results are presented for each parameter. The positioning uncertainty results in a peak density variation of $\pm 3\%$. Varying the phase reference produces $\pm 1\%$ density variations. Lastly, uncertainty in the choice of cutoff frequency produces $\pm 10\%$ variation in peak density. This uncertainty dominates due to the semi-quantitative nature of choosing the cutoff frequency in comparison to the quantitative nature of the other uncertainties. The 2% error allocated to the effect from asymmetry is also included. An additional 1% is included to account for other uncertainties in the diagnostic system such as a slight non-ideal behavior affecting the plasma model. The total uncertainty is estimated to be $\pm 17\%$. The system has shown a repeatability in the peak density to within 10%, well within the estimated uncertainty.

Summary

The electron number density of a closed drift Hall thruster is mapped in vacuum in the region from 0.09 m to 0.90 m axially from the thruster with discharge voltage of 300 V and discharge current of 4.5 A. The measurements of the SPT-100 compare well with previous data taken at a constant radial distance of 0.30 m. The peak density in the measurement region 0.09 m axially from the thruster was $1.3 \times 10^{17} \text{ m}^{-3}$ for the SPT-100 thruster.

The results were modeled using a functional combination of a Gaussian beam and a point source expansion term in an attempt to bridge the near- and far-field characteristics of the thrusters. The model fits very well in the optimization region from 0.12 m to 0.70 m radially from the thruster.

Indications of asymmetry due to the cathode are derived by summing the particles in the two half planes, with and without the cathode. These calculations indicate a 0.8° off-axis density asymmetry for the SPT-100. The results with the SPT-100 agree with previous measurements using the velocity vector as an indicator of asymmetry [8]. This small asymmetry does not affect the density results beyond the estimated uncertainty.

The spectral measurements indicate a 26 kHz harmonic modulation of the density with broadband noise raising the -110 dBm noise floor between 5 and 20 dB for a spectral range of 10 kHz to 1 MHz. The phase noise indicated by the plasma oscillations produced only a $\pm 0.5^\circ$ phase variation for our narrow band system but could have greater impact on more sensitive radar systems with wider bandwidth and lower operating frequency.

Attenuation measurements showed slightly over 2 dB of loss at the nearest measurement point at 17 GHz. However, the attenuation was measured at below 1 dB 0.24 m axially from the exit plane and 0.08 m radially out from the thruster center line. The attenuation produced minimal phase variation. The loss of power is primarily attributed to refraction effects near or within density gradients in the plume. The electron number density functional model has been applied in a ray tracing algorithm demonstrating

consistency with the attenuation measurements. The modeling also indicates that electromagnetic signals operating at lower frequencies, such as GPS, could have significant performance degradation without careful planning of antenna/thruster placement or operational scheduling.

ACKNOWLEDGMENTS

The authors would like to thank several students at PEPL including M. Domonokos, J. Foster, J. Haas, S.W. Kim, B. King, and C. Marrese, whose help made the experiments happen. We would also like to thank M. Holladay of the Space Physics Laboratory for his work on coding the ray tracing model. Our appreciation also goes to Prof. V. Liepa and Prof. K. Sarabandi for their generous use of equipment. We wish to thank M. Day from Space Systems/Loral for the loan of the SPT-100.

Section III References

1. Myers, R.M. and Manzella, D.H., "Stationary Plasma Thruster Plume Characteristics," 23rd International Electric Propulsion Conference, Seattle, WA, Paper 93-096, Sept. 1993.
2. Ohler, S., Gilchrist, B.E., Gallimore, A.D., "Microwave Plume Measurements of an SPT-100 Using Xenon and a Laboratory Model SPT Using Krypton," 31st Joint Propulsion Conference, San Diego, CA, Paper 95-2931, July, 1995.
3. Pencil, E.J., "Preliminary Far-Field Plume Sputtering of the Stationary Plasma Thruster (SPT-100)," 23rd International Electric Propulsion Conference, Seattle, WA, Paper 93-098, Sept. 1993.
4. Sankovic, J., Hamley, J., and Haag, T., "Performance Evaluation of the Russian SPT-100 Thruster at NASA LeRC," 23rd International Electric Propulsion Conference, Seattle, WA, Paper 93-094, Sept. 1993.
5. Garner, C.E., et al., "Performance Evaluation and Life Testing of the SPT-100," 23rd International Electric Propulsion Conference, Seattle, WA, Paper 93-091, Sept. 1993.
6. Dickens, J., Kristiansen, M., O'Hair, E., "Plume Model of Hall Effect Plasma Thrusters with Temporal Considerations," 25th International Electric Propulsion Conference, Moscow, Russia, Paper 95-171, Sept. 1995.
7. Dickens, J., Mankowski, J., Kristiansen, M., and O'Hair, E., "Impact of Hall Thrusters on Communication System Phase Noise," 31st Joint Propulsion Conference, San Diego, CA, Paper 95-2929, July, 1995.
8. Manzella, D., "Stationary Plasma Thruster Ion Velocity Distribution," 30th Joint Propulsion Conference, Indianapolis, IN, Paper 94-3141, June 1994.
9. Manzella, D.H., "Stationary Plasma Thruster Plume Emissions," 23rd International Electric Propulsion Conference, Seattle, WA, Paper 93-097, Sept. 1993.
10. Absalamov, S.K., et al. "Measurement of Plasma Parameters in the Stationary Plasma Thruster (SPT-100) Plume and its Effect on Spacecraft Components," 28th Joint Propulsion Conference, Nashville, TN, Paper 92-3156, July, 1992.
11. Marrese, C., Gallimore, A.D., Haas, J., Foster, J., King, B., Kim, S.W., Khartov, S., "An Investigation of Stationary Plasma Thruster Performance with Krypton Propellant," 31st Joint Propulsion Conference, San Diego, CA, Paper 95-2932, July, 1995.
12. Gallimore, A., Reichenbacher, M., and Guiczinski, F., "Near and Far-Field Plume Studies of a 1kW Arcjet," 30th Joint Propulsion Conference, Indianapolis, IN, Paper 94-3137, June, 1994.

13. Ohler, S.G., Gilchrist, B.E., and Gallimore, A.D., "Non-intrusive electron number density measurements in the plume of a 1 KW arcjet using a modern microwave interferometer," *IEEE Trans. Plasma Sci.*, Vol. 23, No. 3, June, 1995, pp. 428-435.
14. Ohler, S.G., Gilchrist, B.E., and Gallimore, A.D., "Flexible microwave system to measure the electron number density and quantify the communications impact of electric thruster plasma plumes," *Rev. Sci. Instrum.* 68, No. 2, Feb. 1997, pp. 1189-1194.
15. Sips, A.C.C., "Doctoral Thesis: Reflectometry and Transport in Thermonuclear Plasmas," in the Joint European Torus, College van Dekanen, 1991.
16. Wu, H.P. and McCreery, R.L., "Observation of Concentration Profiles at Cylindrical Microelectrodes by a Combination of Spatially Resolved Absorption Spectroscopy and the Abel Inversion," *Anal. Chem.*, Vol. 61, No. 21, Nov. 1989, pp. 2347-2352.
17. Okada, S., et al., "Reduction of the Density Profile of a Field-reversed configuration From Detailed Interferometric Measurements," *J. Appl. Phys.*, Vol. 16, No. 12, June 1989, pp. 4625-3631.
18. Lanquart, J.P., "Error Attenuation in Abel Inversion," *J. Comput. Phys.*, Vol. 47, 1982, pp. 434-443.
19. Sharma, S.K., "Density Profile Determination of Cylindrically Symmetric Nonuniform Plasma Spatial Filtering," *Plasma Phys. Contr. Fus.*, Vol. 28, No. 1B, 1986, pp. 391-392.
20. Smith, L.M., Keefer, D., and Sudharsnan, S.I., "Abel Inversion Using Transform Techniques," *J. Quant. Spectrosc. Radiat. Transfer*, Vol. 39, No. 5, 1988, pp. 367-373.
21. Carney, L.M. and Sankovic, J.M., "The Effects of Arcjet Thruster Operating Condition and Constrictor Geometry on the Plasma Plume," 25th Joint Propulsion Conference, Monterey, CA, Paper 89-2723, July, 1989.
22. Birkner, G.A., Hallock, H.K., and Ling, H., "Arcjet plasma plume effect on a microwave reflector antenna," *Rev.Sci. Instrum.*, Vol. 61, No. 10, Oct. 1990, 2978-2980.
23. Ling, H. and Kim, H., "Electromagnetic Scattering From an Inhomogeneous Object By Ray Tracing," *IEEE Trans. Antennas and Propag.*, Vol. 4, May 1991, pp. 517-525.
24. Ling, H., et al., "Effect of an Arcjet Plume on Satellite Reflector Performance," *IEEE Trans. Antennas and Propag.*, Vol. 39, No. 9, Sept. 1991, pp. 1412-1419.

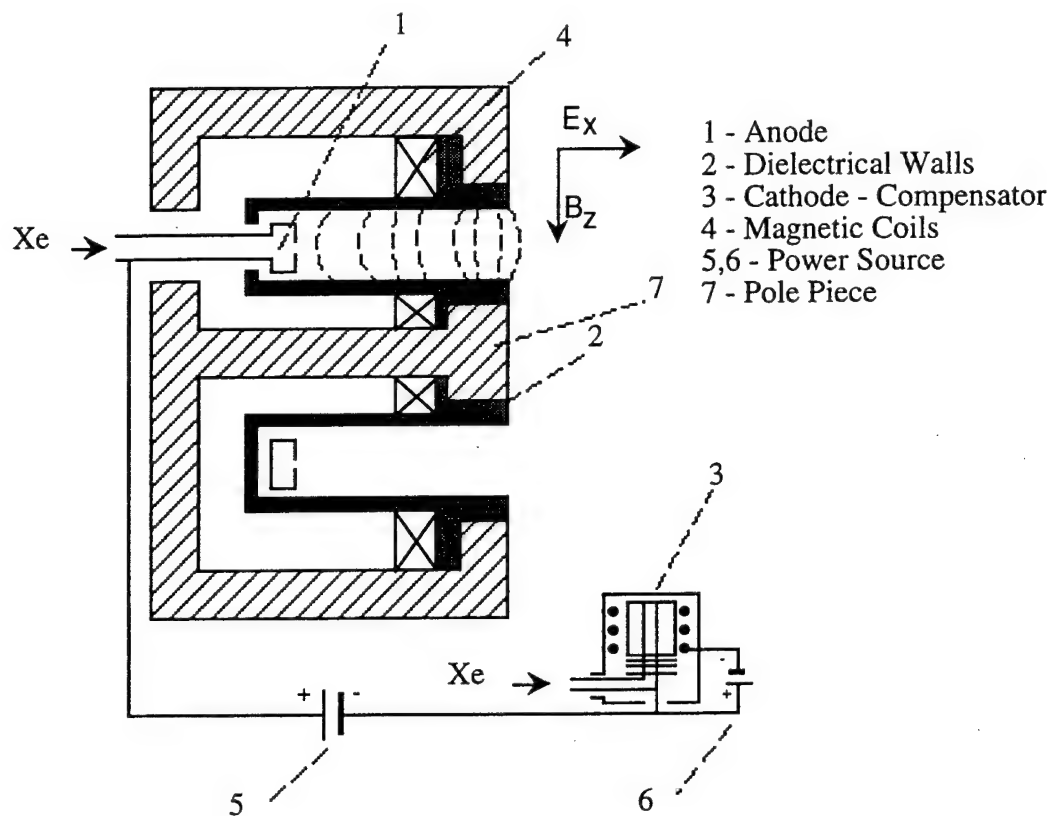


Figure 1: Diagram of SPT-100 with discharge chamber pointed upward.

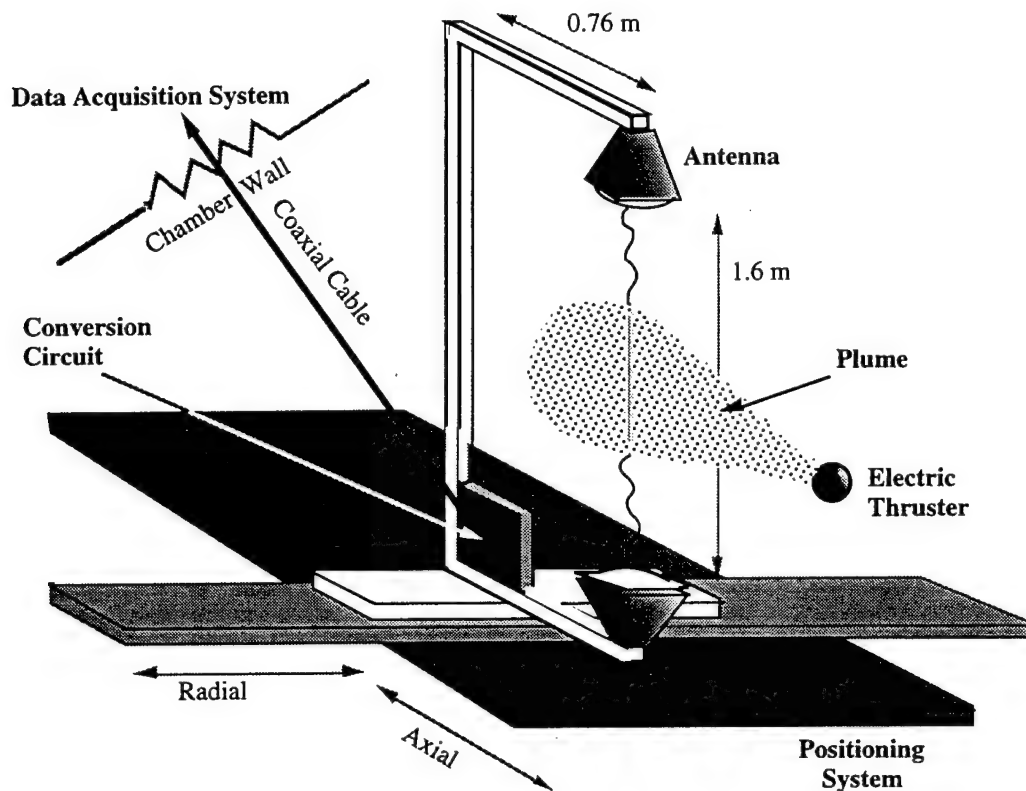


Figure 2: Microwave System Schematic.

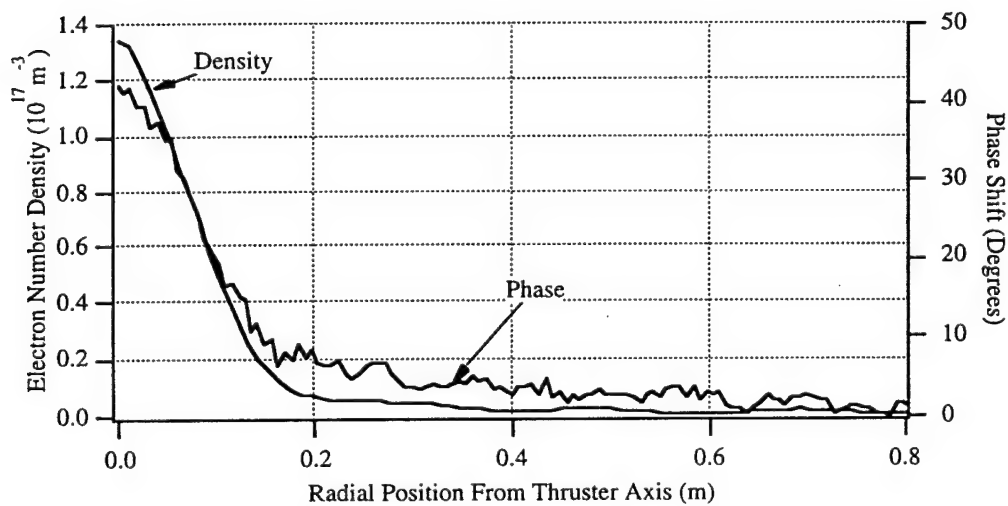


Figure 3: Overlay of phase measurements and calculated density for the SPT-100 at 0.009m from thruster exit plane.

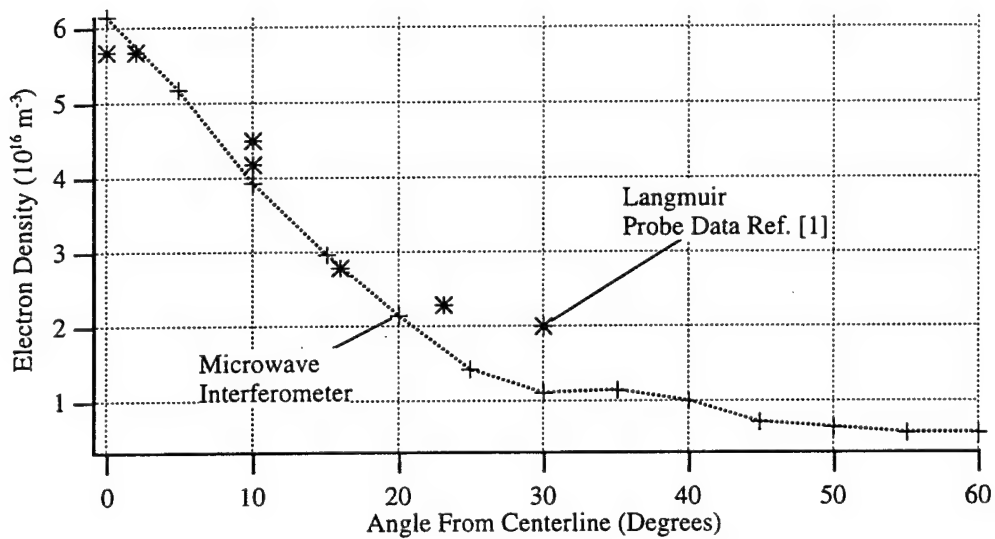


Figure 4: Comparison of microwave measurements to Langmuir probe results taken by Myers [1] both at 0.3 m from the thruster exit plane.

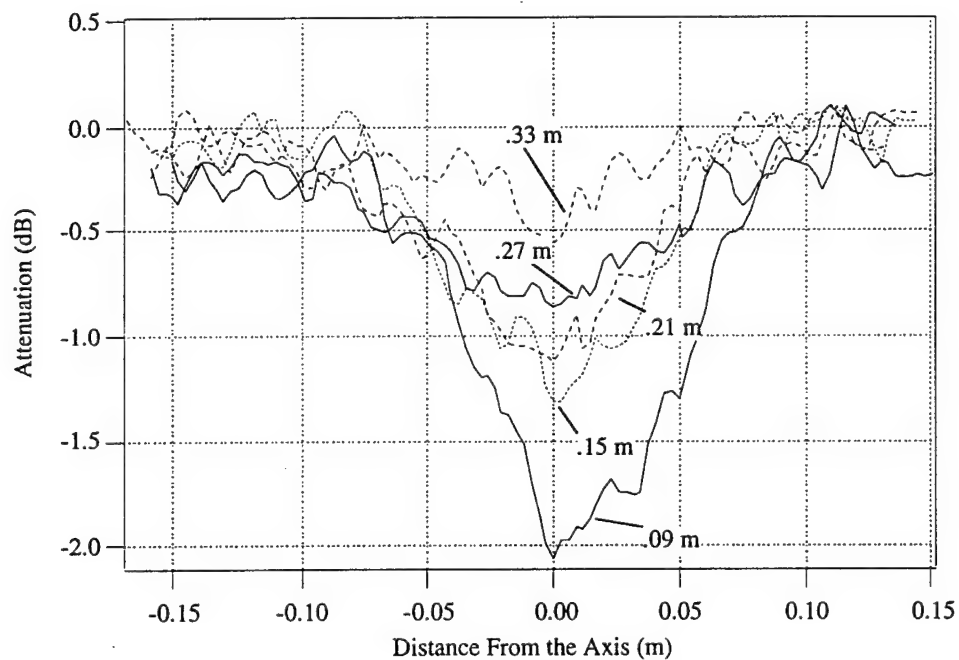
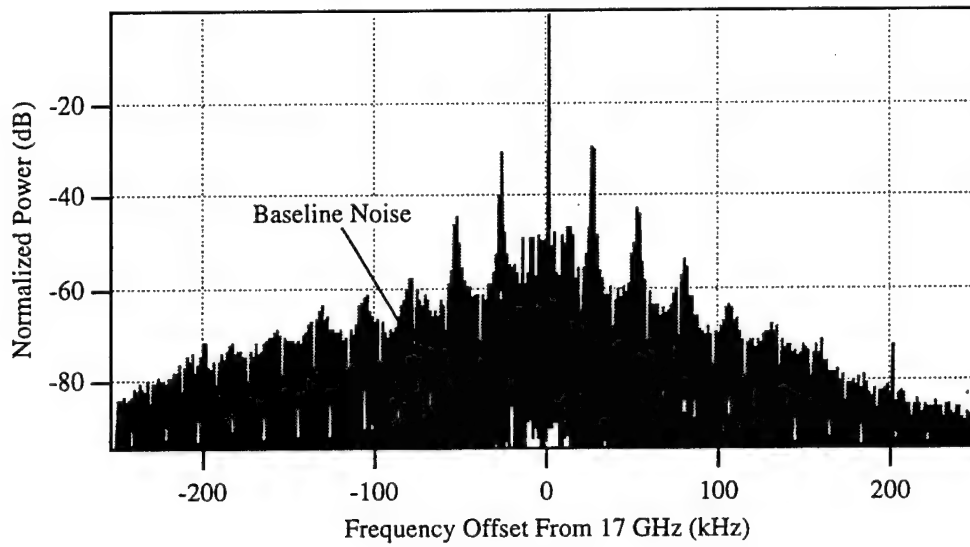


Figure 5: Attenuation measurements for the SPT-100 showing the trends in five planes orthogonal to the thruster axis.

a) 0.15 m downstream of exit



b) 0.5 m downstream of exit

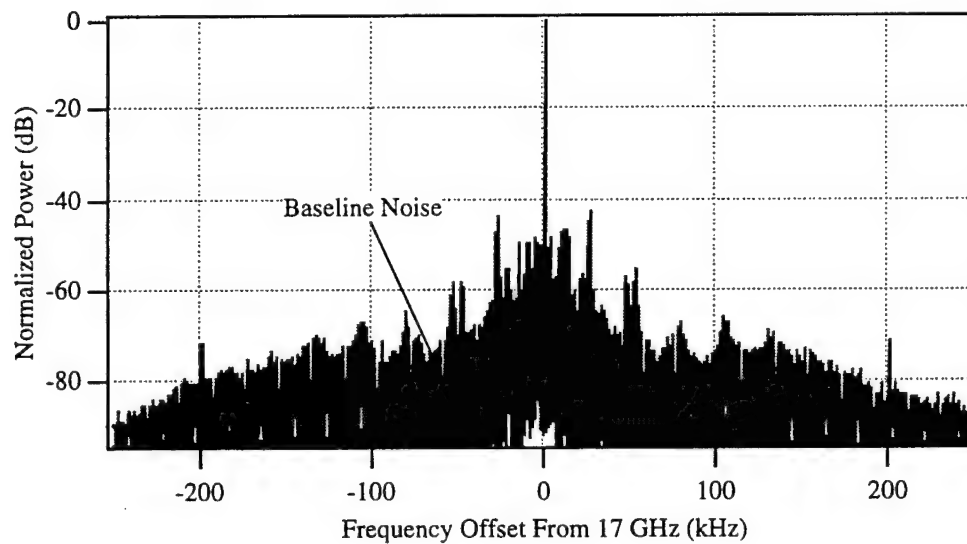


Figure 6: Power spectral density around the 17 GHz signal for the SPT-100; darker region indicates the baseline noise level.

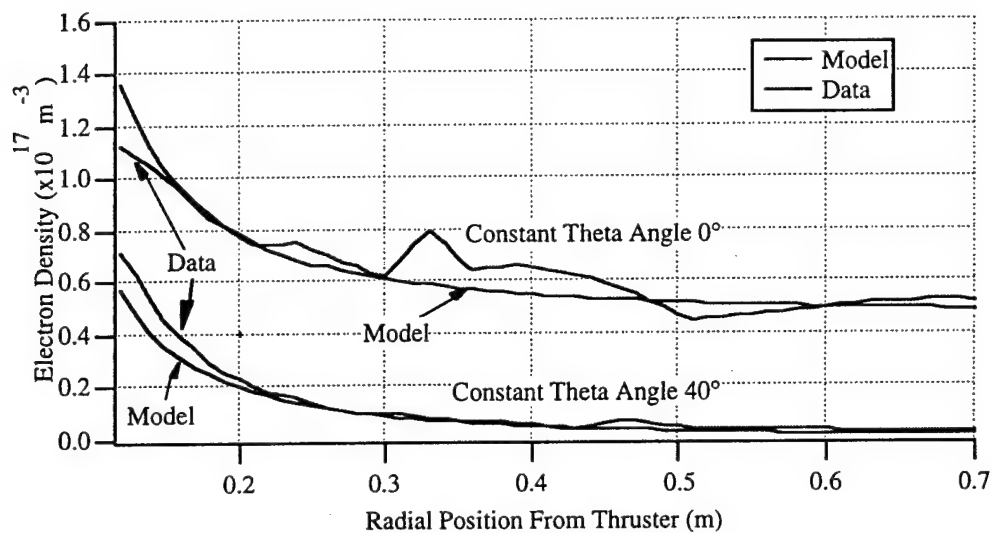


Figure 7: Electron density of the functional model overlaid on the measured data for constant angles with respect to the SPT-100 center line.

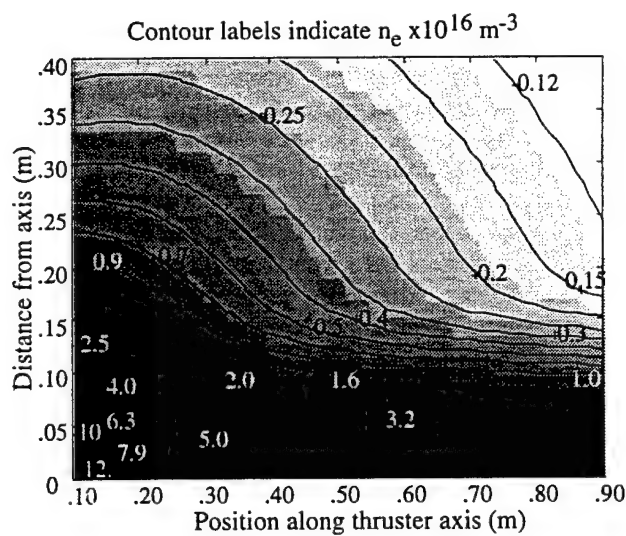


Figure 8: Electron number density functional model contour plot for the SPT-100.

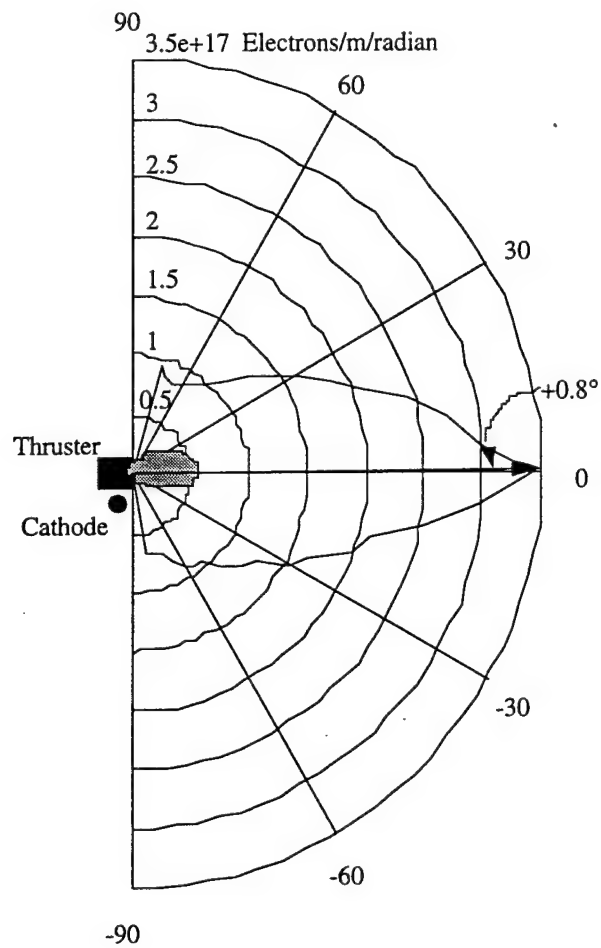


Figure 9: Integrated particle plot for the SPT-100 showing the number of particles at angles from thruster axis. The total particle vector is only 0.8° off axis.

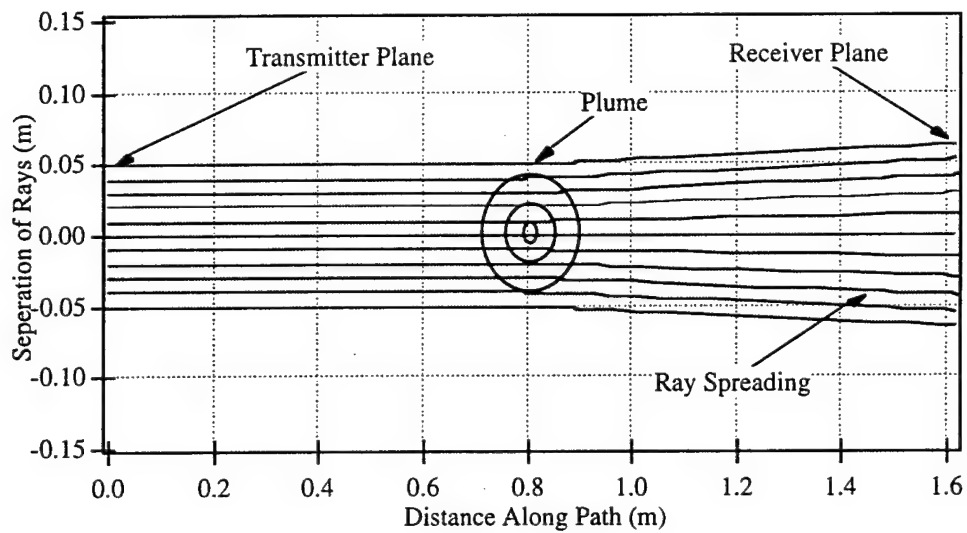


Figure 10: Ray paths of a 17 GHz signal based on the density model. Parallel ray paths diverge after traversing the plume.

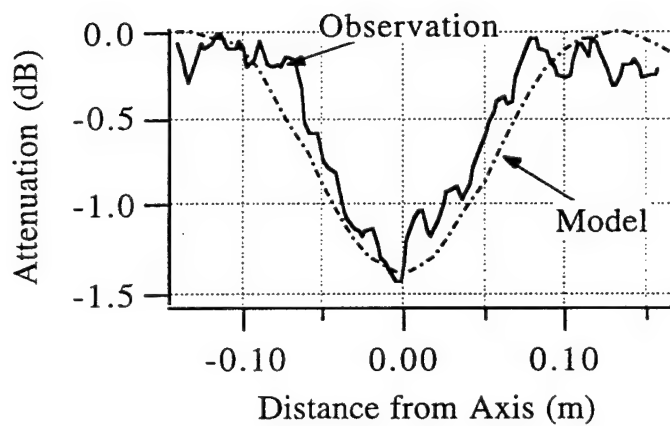


Figure 11: Overlay of one of the attenuation sweeps and the ray tracing results, 0.15 m from the exit plane.

SECTION IV: A MOLECULAR BEAM MASS SPECTROMETER FOR HALL THRUSTER PLUME STUDIES

Abstract

To assess the interaction due to the direct impingement of the ions on spacecraft surfaces it is necessary to accurately quantify the ionic transport properties as a function of spatial coordinates around the thruster. These data can be combined with surface interaction models to predict surface erosion, contamination, and heating rates. Previous studies have used probe-based techniques to obtain the transport of mass, energy, and charge on a global (species-independent) scale within an extensive volume of the plume. This paper presents preliminary data from an effort to further improve the probe-based quantities by extending the data to species-dependent measurements of transport properties. The construction of the Molecular Beam Mass Spectrometer (MBMS) reported herein was motivated by the shortcomings discovered in the previous probe-based techniques. The probe data has proven very useful, however, like any diagnostic technique they are subject to limitations. Although the MBMS system is subject to its own inherent imperfections, these limitations are different from and complimentary to the probe-based techniques.

I. Nomenclature

$y=$	Spatial coordinate (m)
$x=$	Spatial coordinate (m)
$d=$	Analyzer plate separation (mm)
$d_{\text{tof}}=$	Ion flight path length (m)
$l=$	Interslit distance (mm)
$m_p=$	Proton mass (kg)
$n=$	Ion mass (amu)
$q=$	Ion integral charge state
$t_{\text{tof}}=$	Ion time-of-flight
$w=$	Entrance and exit slit width (mm)
$\theta=$	Ion launch angle (rad)
$V_p=$	Repelling plate voltage (V)
$E_i=$	Ion energy (eV)
$k=$	Analyzer spectrometer constant
$I_i=$	Ion current (A)
$A_{\text{coll}}=$	Ion current collector area
$e=$	Elementary charge (coul)
$m=$	Mass of ion (kg)
$I_{i,E}=$	Current of ions with energy E (A)
$n_{i,E}=$	Density of ions with energy E (m^{-3})
$F(E)=$	Ion energy distribution function
$V_d=$	Thruster discharge voltage (V)
$I_d=$	Thruster discharge current (A)

II. Introduction

1. Motivation. With the promise of high performance and economic benefits in the near future, there is currently a widespread effort to fully flight qualify Closed Drift Hall Thrusters (CDT's) and proceed to routine application of these devices.¹⁻⁵ The study reported in this paper represents an ongoing program at the University of Michigan to characterize the interaction between the plume of a CDT and the supporting spacecraft. Two basic interaction

modes are being studied: the effect of the plasma environment on transmitted and received electromagnetic communication signals,⁶ and the potential structural impact caused by high energy plume ions.⁷

To assess the interaction due to the direct impingement of the ions on spacecraft surfaces it is necessary to accurately quantify the ionic transport properties as a function of spatial coordinates around the thruster. These data can be combined with surface interaction models to predict surface erosion, contamination, and heating rates. Previous studies have used probe-based techniques to obtain the transport of mass, energy, and charge on a global (species-independent) scale within an extensive volume of the plume. This paper presents preliminary data from an effort to further improve the probe-based quantities by extending the data to species-dependent measurements of transport properties.

The construction of the Molecular Beam Mass Spectrometer (MBMS) reported herein was motivated by the shortcomings discovered in the previous probe-based techniques. The probe data has proven very useful, however, like any diagnostic technique they are subject to limitations. Although the MBMS system is subject to its own inherent imperfections, these limitations are different from and complimentary to the probe-based techniques.

Of great interest in calculating both plume transport properties and thruster performance is an accurate measurement of the ion energy distribution. This has previously been measured using a gridded Retarding Potential Analyzer (RPA) as an in-situ probe.⁷ Recent experience has shown that the elevated density within the RPA due to the "ram" build-up inside the probe can cause both collisional broadening and attenuation of the incoming ion energy stream. Furthermore, the RPA technique has no dependence upon charge carrier mass or charge state, i.e. it cannot discriminate between multiply charged ions of the same mass nor ions of different masses. As another measure, ion energy data has also been obtained through Laser Induced Fluorescence (LIF),⁸ these data show a much narrower energy distribution than the probe-based RPA technique. A means of reconciling the discrepancy between these two techniques has not yet been proven.

Another desirable quantity for both thruster and spacecraft designers is the thruster erosion rate. Erosion limits the life of the thruster itself in addition to potentially depositing erosion material on sensitive spacecraft surfaces. Previous methods to quantify this erosion include pre- and post-test weighing of the thruster itself to determine mass loss, and the examination of deposition material on witness plates and quartz crystal microbalances (QCM's) immersed in the plume. Although these methods provide accurate, useful data, a limitation to both is their sensitivity only to net deposition/erosion rate. The thruster simultaneously erodes the sample materials through plume ion sputtering while depositing thruster-body erosion products; the witness plate/QCM technique does not discriminate between these two processes. In addition, much of the deposited material may be due to facility effects (i.e. pump oil, sputtered material from vacuum chamber surfaces).

2. MBMS Diagnostic Goals. In order to complement the extensive data sets as described above, the construction of an MBMS system for CDT research was initiated.

A primary goal of this study is to measure the ion energy distribution of the primary plume mass species, Xe, to a greater accuracy than obtained through the RPA technique. In addition, this energy distribution will be measured as a function of the Xe charge state, i.e. separate energy distributions will be measured for Xe^+ , Xe^{++} , and Xe^{3+} . Limitations inherent to the RPA such as collisional energy broadening, attenuation, and space charge shielding effects of the repelling grids are eliminated through the use of differential pumping and a small diameter ion beam. From a spacecraft interaction standpoint this will facilitate comparison between the previous RPA and LIF measured values for a more accurate evaluation of plume transport. In terms of thruster performance, these data are especially insightful. The ion energy distribution is intrinsically linked to the spatial distribution of ion production rate and the topography of the electric field within the thruster discharge chamber: knowledge of any two quantities uniquely specifies the third. By analyzing the charge state dependent distributions, it is

possible to derive information regarding internal temperatures and ion production within the thruster.

Another main focus of this research is to measure the species fractions and transport rate of minority plume constituents such as heavy metals and ceramic components to more fully understand thruster erosion processes. By limiting the analysis of minority carriers to those particles with energies on the order of the thruster discharge voltage, this diagnostic will be insensitive to low energy minority species formed by ion sputtering of facility surfaces and will indicate only those particles which originated within the thruster. If signal strength permits, energy distributions of these minority constituents will also be performed. This will indicate the physical location within the thruster of possible thruster life-limiting erosion phenomena.

III. Description of Apparatus

The MBMS system can be operated in either of two modes: global energy analysis mode, or time-of-flight mass spectrometric mode. In this section the overall configuration of the instrument will be presented, followed by a discussion of both modes of operation.

1. Overall Configuration. The MBMS system uses a set of orifice skimmers to admit a beam of plume ions from the main vacuum chamber into an array of differentially pumped sub-chambers. The overall layout of the system is shown in Fig. 1. The skimmers are fashioned from 304 SS plates drilled and countersunk. This creates a very thin edge on the inlet orifice and minimizes skimmer wall effects. Both collimator and sampling skimmers had 2.5-mm-dia. orifices. The low densities within the plume and relatively large mean free paths permit the use of flat plates as opposed to cone or trumpet-shaped skimmers while introducing negligible upstream scattering.

An ion beam from a CDT plume is admitted through the sampling skimmer into the first sub-chamber. A second collimating skimmer geometrically confines the ions to a beam with half angle less than 2.5 mrad. This collimated beam passes through the entrance slit of a 45 degree parallel plate electrostatic energy analyzer; a selected beam energy is allowed to exit the analyzer through an exit slit; the ions with a pre-selected energy then proceed to an electron multiplier, where the ion current is amplified by a factor of 10^8 .

The 45 degree electrostatic energy analyzer is a flexible, robust method for particle energy filtering that has been utilized in a variety of research.⁹⁻¹² A schematic of this system is shown in Fig. 2.

The plasma beam is admitted through the entrance slit and immediately enters a region of constant electric field of magnitude V_p/d with a launch angle of 45 deg. The much lower energy electrons are sharply deflected in a direction opposite to the ions and effectively removed from the beam. The ions experience a region of constant acceleration in the y-direction such that the spatial equation of their trajectory is

$$y = x - \frac{1}{2d} \frac{V_p}{E_i} x^2$$

In order for an ion to pass through the exit slit and be detected it must intersect the point $y=0$, $x=l$; this pass constraint is defined as the spectrometer constant, k , and is given by

$$k \equiv \frac{V_p}{E_i} = \frac{2d}{l}$$

The energy resolution, or resolving power, of the analyzer is dictated by instrument geometric parameters and is given by

$$\frac{\Delta E_i}{E_i} = \frac{w \sin \theta}{l}$$

Table 1 outlines the pertinent parameters for the energy analyzer and MBMS system constructed for this study. The energy analyzer was constructed of 1.5-mm-thick aluminum plates. In order to eliminate field distortion due to the surrounding grounded vacuum chamber, a set of seven centrally slotted shim plates were biased using a voltage divider; this ensured a constant homogeneous electric field between the inlet plate and repeller.

Parameter	Value
l	571 mm
d	160 mm
w	2 mm
$\Delta E_i/E_i$	2.5×10^{-3}
k	0.56

Table 1. Defining parameters of 45 degree electrostatic energy analyzer.

The beam chambers are constructed of standard conflat-style vacuum hardware with tube I.D. of six inches for the portion of the MBMS within the main vacuum chamber and eight inch I.D. for the differential pumping and energy analysis chambers. The MBMS inlet chamber and skimmer are maintained at facility ground. Although this imposes a slight perturbation to the plume, previous research with such a system has shown that this small effect can easily be corrected and has no effect on the resulting data.⁹

The beam inlet chamber is pumped by a 10" oil diffusion pump, and the energy analysis chamber by a 6" oil diffusion pump. The system is capable of base pressures of 3×10^{-7} Torr within 2 hrs of pumpdown with no system bakeout. A large 8" diameter gate valve is used to isolate the energy analysis section from the main tank to facilitate rapid re-configuration and pump cycles without the need to vent the main tank.

Energy Analysis Mode. In this mode of operation the MBMS is insensitive to particle mass, however, by utilizing a sensitive picoammeter to monitor the output of the electron multiplier, high-resolution ion energy distribution data can be obtained from centerline to large angles approaching and possibly exceeding 90 degrees.

In Energy Analysis mode both the ion beam gate potential and Einzel lens are de-energized and maintained at facility ground. The repelling voltage of the 45-degree energy analyzer is varied using a highly accurate electrometer, while the steady-state ion current from the electron multiplier is measured using a picoammeter.

The equation relating the collected current to the energy distribution function is

$$I_i = A_{\text{coll}} e n_i \langle u_i \rangle$$

For a single value of pass energy,

$$\langle u_i \rangle = u_i = \sqrt{\frac{2qE_i}{m}}$$

so that now, the collected current for a given energy can be expressed as

$$I_{i,E} = A_{\text{coll}} e n_{i,E} \sqrt{\frac{2qE_i}{m}}$$

where $n_{i,E}$ is now the density of ions with energy E_i , which is precisely the ion energy distribution function:

$$F(E) \equiv n_{i,E} = \frac{1}{e A_{\text{coll}}} \sqrt{\frac{m}{2q}} \frac{I_{i,E}}{\sqrt{E_i}}$$

The ion energy distribution function for a constant n/q is thus proportional to the collected current at a given pass energy divided by the square root of the pass energy.

Time-of-Flight Mode. By utilizing a high voltage pulsing network in addition to a fast, low-noise current amplifier on the electron multiplier, the MBMS can measure the relative intensity of each mass species within the plume as a function of ion energy. In this configuration an electrostatic beam gate is used to "chop" the incoming ion beam into short pulses. A deflection voltage of approximately -1.5 kV is applied between two planar electrodes creating an electric field that steers the beam into the chamber wall. A momentary (2 μsec) pulse is then applied to the deflection plates eliminating the electric field and admitting a short burst of ions towards the energy analyzer and collector. The 45-degree analyzer transmits only those ions with a set value of $1/2 mu^2$ to the electron multiplier for detection; since ions of equal energy but differing mass will travel at different velocities, the ions will arrive "bunched" by mass at the collector with the lightest ions arriving earliest. The resulting current output of the electron multiplier will be a series of peaks in time which, combined with the known flight path length, can be converted into intensity as a function of particle mass according to

$$\frac{n}{q} = \frac{t_{\text{tof}}^2}{d_{\text{tof}}^2} \frac{2eE_i}{m_p}$$

where n is the particle mass in AMU, q is the integral ion charge state, t_{tof} is the flight time, d is the flight path length, and m_p is the proton mass.

In order to maximize ion throughput, a three component Einzel lens was mounted immediately downstream of the beam gate. This lens utilized a short focal length to transmit a collimated beam of ions to the energy analyzer and reduced the current attenuation due to geometric beam spreading.

IV. Preliminary Data

1. Experimental Set-up. Due to the unavailability of an SPT-100 at the time of testing, preliminary tests were done in the plume of a D-55 anode layer thruster. Operating conditions were $V_d=300$ V, $I_d=4.5$ A, mass flow of 60 sccm Xe. The thruster was mounted to a rotary table such that the centerline of the thruster exit plane coincided with the axis of rotation of the table; this allowed remote rotation of the D-55 relative to the fixed MBMS skimmer inlet enabling data acquisition as a function of angle off plume centerline. The thruster/table assembly was mounted in the main vacuum chamber with the exit plane 0.5 m from the skimmer inlet.

In order to correct for the plume perturbation imposed by the grounded MBMS inlet an emissive probe was used to measure the local plasma potential.¹³ A single-loop probe was mounted 10 cm upstream of the skimmer. By subtracting the value of the local plasma potential from the measured ion energy, the data are corrected for the energy imparted to the ions as they "fall" from plasma potential through the sheath on the inlet skimmer to ground potential.

For operation in Energy Analysis mode the output of the electron multiplier was monitored using a picoammeter. The repelling voltage on the 45-degree energy analyzer was slowly varied using an electrometer and the corresponding current was recorded from the picoammeter to a computer.

For operation in time-of-flight mode the picoammeter had insufficient bandwidth to measure the rapidly changing time-of-flight current pulse. In this mode, a fast (5 nsec rise time) transimpedance preamplifier was constructed to perform a 50 mV/ μ A conversion on the electron multiplier output current; the output of this preamplifier was post-amplified by a high-frequency, low-noise amplifier having a voltage gain of 50 for an overall amplifier gain of 2.5 V/ μ A; combined with the gain of the electron multiplier this circuit comprised an amplification of the true ion current to a level of 2.5×10^{14} V/A.

The circuit utilized for time-of-flight mode is depicted in Fig. 3. The beam gate voltage was supplied by a -1.5 kV supply controlled through a high-voltage switcher; the output of this switcher was measured using a high-voltage probe and employed as the trigger to the digitizing oscilloscope. The output of the electron multiplier post-amplifier was recorded on the scope and waveform averaged over 500 pulses to improve signal-to-noise values. The data was then downloaded to a computer for post-processing.

2. Results. Ion energy distribution curves have been recorded from thruster centerline out to 90 degrees at a radial distance of 0.5 m from the D-55 exit plane. The centerline ion energy distribution is shown as Fig. 4. This curve shows a most-probable ion energy of 278 eV (with respect to ground) with a full-width-at-half-max of 30 eV. During thruster operation the cathode potential floated to -13 V with respect to thruster ground; this represents an available ion energy of 287 eV with respect to ground. Although the peak in the energy distribution is less than 287 eV as expected, there exists a high-energy tail portion of the curve corresponding to ions with energies greater than that imposed from the discharge voltage. This phenomenon has been repeatedly observed in Hall thruster plume ion energy measurements and has yet to be fully explained.

As the angle off centerline was increased, the ion energy distribution remained essentially unchanged out to an angle of approximately 75 degrees. Beyond this angle, the energy distribution displayed a rapid shift of energy from the roughly 280 eV peak to a broader distribution having a peak at about 140 eV within a space of 5 degrees. This energy shift is shown as Figure 5.

In order to maximize signal strength initial time-of-flight mass spectra was limited to points within 10 degrees of the thruster centerline at a radial distance of 0.5 m from the exit plane. By adjusting the pass energy of the 45 degree analyzer separate spectra can be obtained for any given value of ion energy. A sample plot of the time-of-flight spectra is shown as Fig. 6 for a point 10 degrees off centerline and an ion pass energy of 300 eV.

Prominent features of Fig. 6 include an intense peak at $m/q=131$ corresponding to singly ionized xenon propellant which comprises the bulk of the plume flow. In addition to the 131 peak, prominent peaks exist at $n/q = 65.5$ (Xe^{2+}) and $n/q = 43.6$ (Xe^{3+}). Close analysis reveals the existence of minor peaks having n/q less than about 30; these peaks correspond to parasitic atmospheric gasses entrained within the plume due to facility pumping limitations. An amplified plot of this region of the spectra is shown as Fig. 7 with the probable source of the peaks labeled. Due to electron impact dissociation the facility water vapor produces peaks at $n/q=18$ (H_2O^+), 17 (OH^+), and 1 (H^+); the source of the $n/q=12$ (C^+) peak is most likely from large sheets of flexible graphite used to shield facility surfaces from sputtering. The remaining peaks are due to parasitic atmospheric gasses.

From an analysis of Fig. 6 it is possible to calculate the ionization fractions of 300 eV ions as $\text{Xe}^+=93\%$, $\text{Xe}^{2+}=5\%$, and $\text{Xe}^{3+}=2\%$. In contrast, Fig. 8 shows a plot of the mass spectra corresponding to an ion pass energy of 240 eV, showing a much larger fraction of doubly ionized xenon. By assembling a large number of mass spectra corresponding to different ion pass energies one can calculate the ionization fraction as a function of ion energy for a given position within the plume; Fig. 9 shows such a plot for the point 10 degrees off axis at 0.5-m-radius.

VII. Section IV References

- [1] Gallimore, A.D., Gilchrist, B.E., King, L.B., Ohler, S.G., and Ruffin, A.B., "Plume Characterization of the SPT-100," AIAA-96-3298, 32nd AIAA/ASME/SAE/ASEE Joint Propulsion Conference, July 1-3, 1996, Lake Buena Vista, FL.
- [2] Pencil, E.J., Randolph, T., and Manzella, D.H., "End-of-life Stationary Plasma Thruster Far-field Plume Characterization," AIAA-96-2709, 32nd AIAA/ASME/SAE/ASEE Joint Propulsion Conference, July 1-3, 1996, Lake Buena Vista, FL.
- [3] Manzella, D.H., "Stationary Plasma Thruster Plume Emissions," IEPC-93-097, 23rd International Electric Propulsion Conference, Sept. 13-16, Seattle, WA.
- [4] Day, M., Maslennikov, N., Randolph, T., and Rogers, W., "SPT-100 Subsystem Qualification Status," AIAA-95-2666, 31st AIAA/ASME/SAE/ASEE Joint Propulsion Conference, July 10-12, San Diego, CA.
- [5] Garner, C.E., Brophy, J.R., Polk, J.E., and Pless, L.C., "A 5,730-Hr Cyclic Endurance Test of the SPT-100," AIAA-95-2667, 31st AIAA/ASME/SAE/ASEE Joint Propulsion Conference, July 10-12, 1995, San Diego, CA.
- [6] Ohler, S.G., Ruffin, A.B., Gilchrist, B.E., and Gallimore, A.D., "RF Signal Impact Study of an SPT," AIAA-96-2706, 32nd AIAA/ASME/SAE/ASEE Joint Propulsion Conference, July 1-3, Lake Buena Vista, FL.
- [7] King, L.B., and Gallimore, A.D., "Ionic and Neutral Particle Transport Property Measurements in the Plume of an SPT-100," AIAA-96-2712, 32nd AIAA/ASME/SAE/ASEE Joint Propulsion Conference, July 1-3, 1996, Lake Buena Vista, FL.
- [8] Manzella, D.H., "Stationary Plasma Thruster Ion Velocity Distribution," AIAA-94-3141, 30th AIAA/ASME/SAE/ASEE Joint Propulsion Conference, June 27-29, 1994, Indianapolis, IN.
- [9] Pollard, J.E., "Plume Angular, Energy, and Mass Spectral Measurements with the T5 Ion Engine," AIAA-95-2920, 31st AIAA/ASEM/SAE/ASEE Joint Propulsion Conference, July 10-12, San Diego, CA.
- [10] deZeeuw, W.A., van der Ven, H.W., de Wit, J.M.M., and Donne, J.H., "An electrostatic time-of-flight analyzer for simultaneous energy and mass determination of neutral particles," Rev. Sci. Instrum. 62 (1), Jan 1991, pp. 110-117.
- [11] Gaus, A.D., Htwe, W.T., Brand, T.J., and Schulz, M., "Energy spread and ion current measurements of several ion sources," Rev. Sci. Instrum. 65 (12), Dec. 1994, pp. 3739-3745.

- [12] Esaulov, V.A., Grizzi, O., Guillemot, L., Huels, M., Lacombe, S., and Vu Ngoc Tuan, "An apparatus for multiparametric studies of ion-surface collisions," *Rev. Sci. Instrum.* 67 (1), Jan 1996, pp. 134-144.

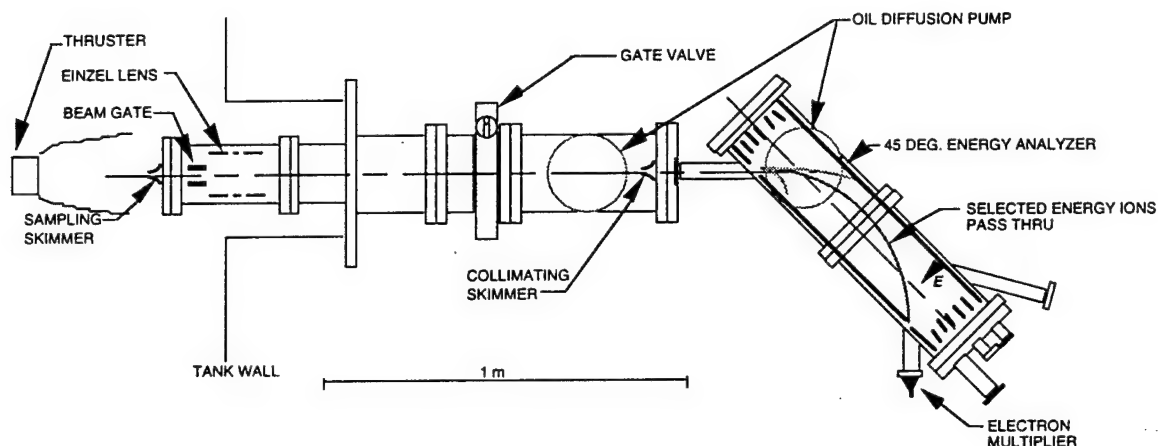


Fig. 1. Overall layout of MBMS system showing ion optical components and interface with main vacuum chamber.

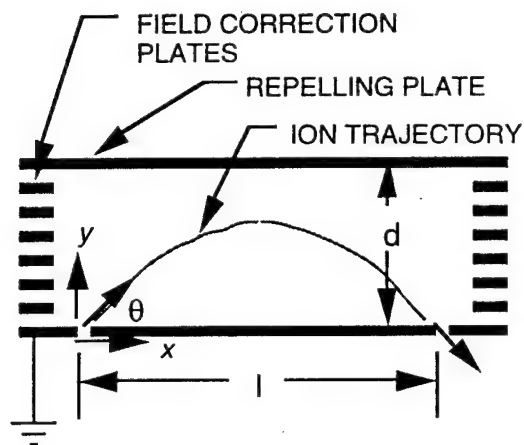


Fig. 2. Schematic of 45-degree electrostatic energy analyzer and nomenclature.

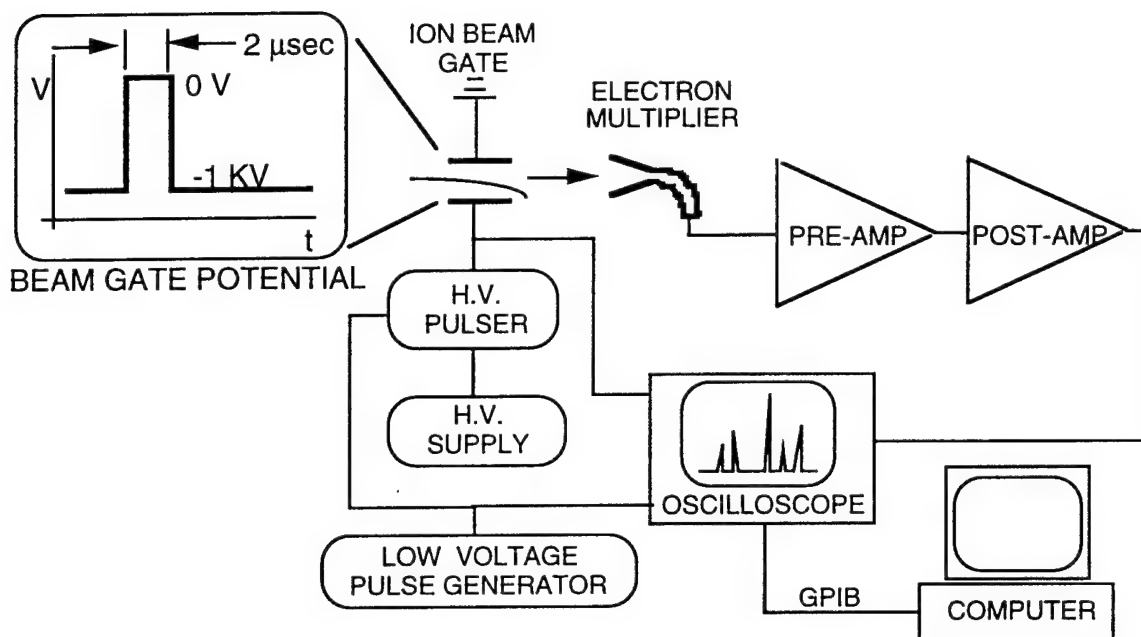


Fig. 3. Schematic of set-up for operation of MBMS in time-of-flight mode. The HV Pulser network drives the potential of one of the deflection electrodes on the ion beam gate; the opposing electrode is maintained at facility ground. The DC high voltage bias applied to drive the electron multiplier and the Einzel lens supply are not shown here.

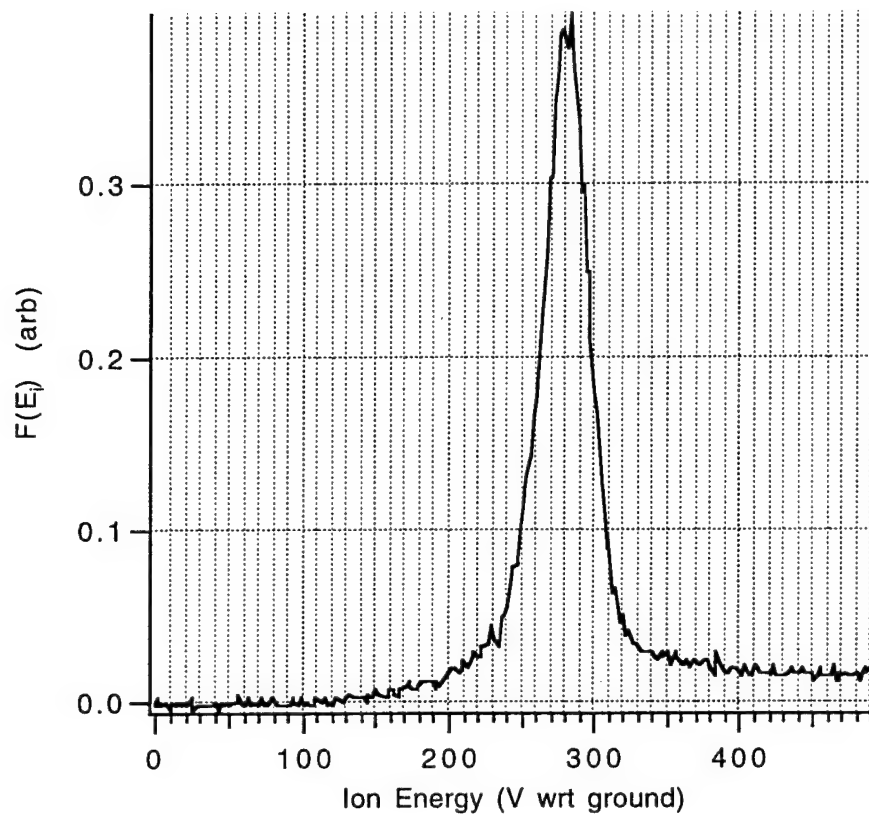


Fig. 4. Centerline ion energy distribution measurement in the plume of the D-55 at 0.5-m- radius from thruster exit plane.

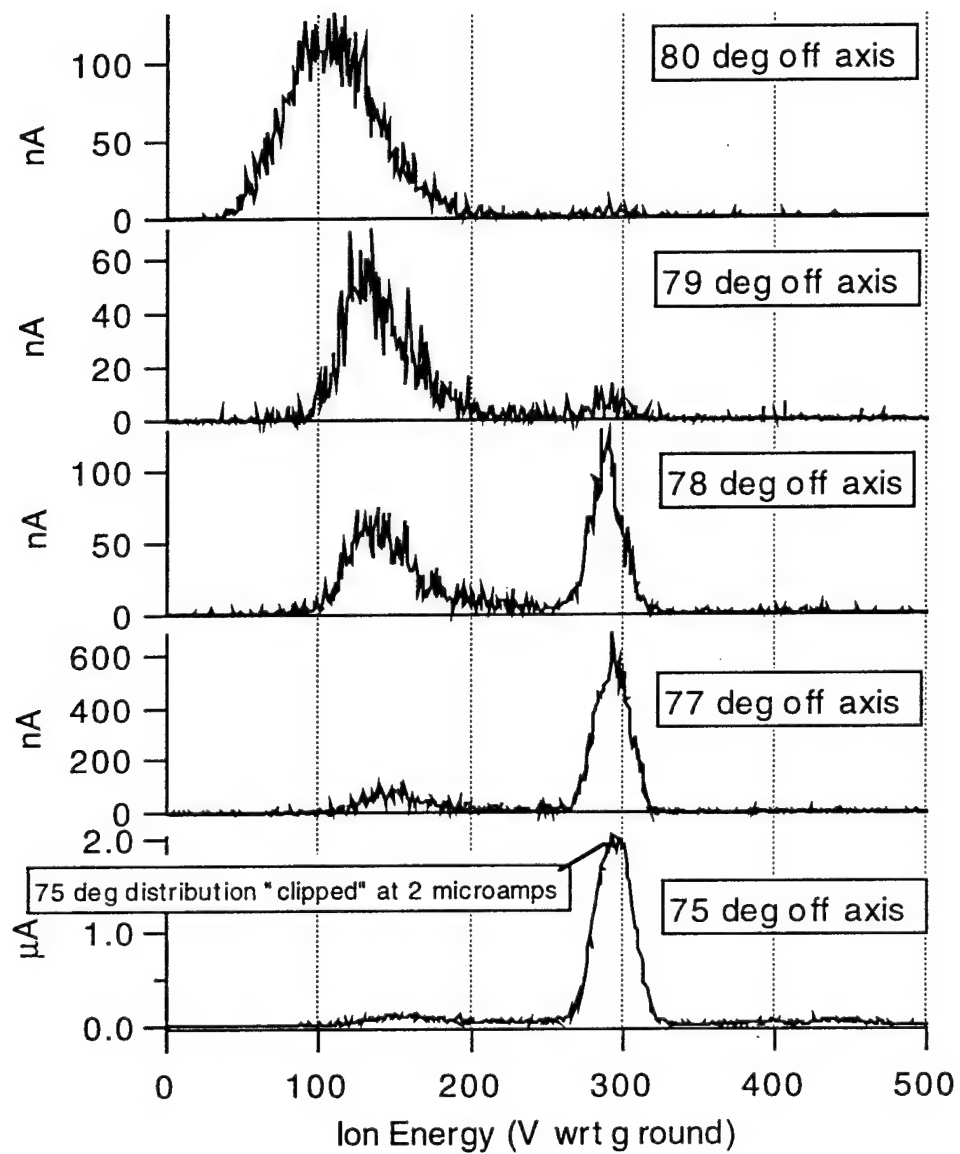


Fig. 5. Angular evolution of ion energy distribution in D-55 plume at 0.5-m-radius from thruster exit plane.

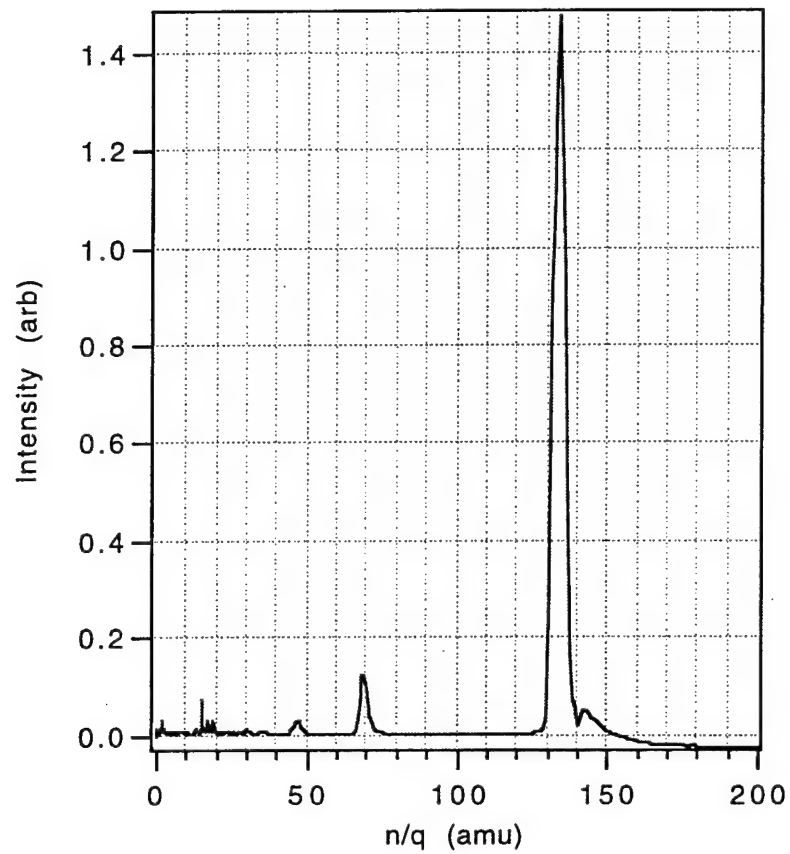


Fig. 6. Ion mass spectra in D-55 at 10 degrees off centerline, 0.5 m radius from exit plane. Spectra is shown for 300 eV ions.

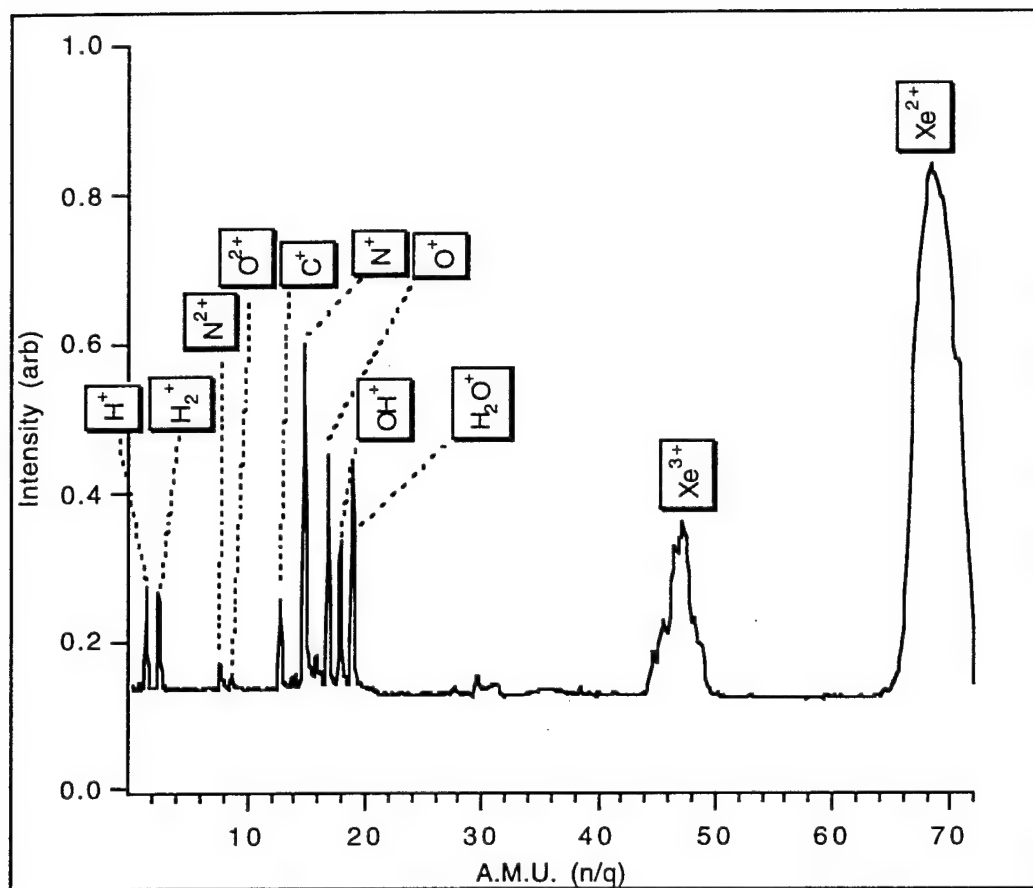


Fig. 7. Minor plume constituents in D-55 at 10 degrees, 0.5-m-radius. Spectra shown is for 300 eV ions.

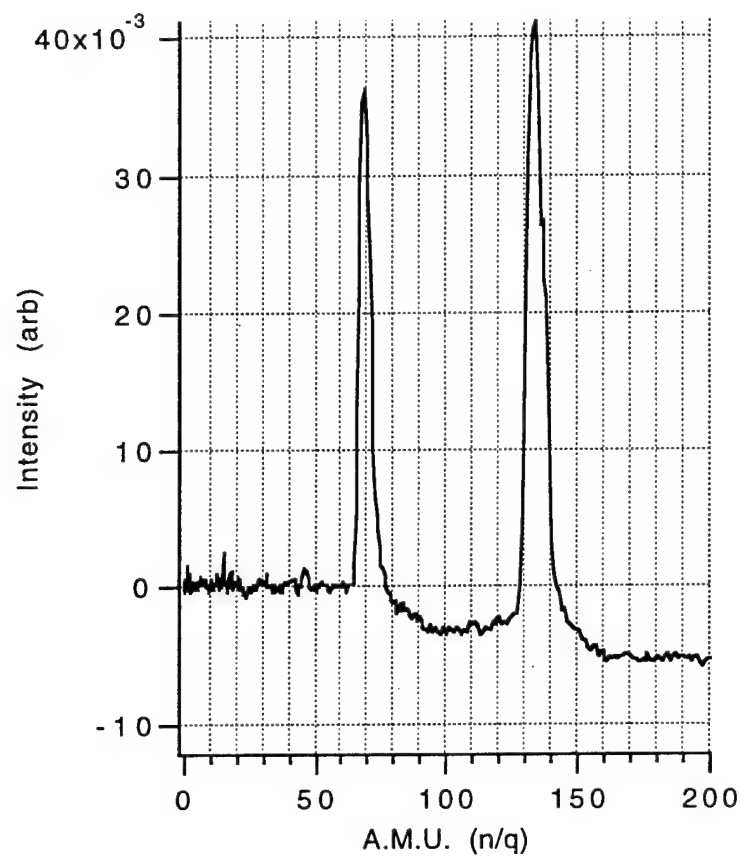


Fig. 8. Mass spectra in D-55 plume 10 degrees off centerline, 0.5-m-radius from exit plane.
Spectra is shown for 240 eV ions.

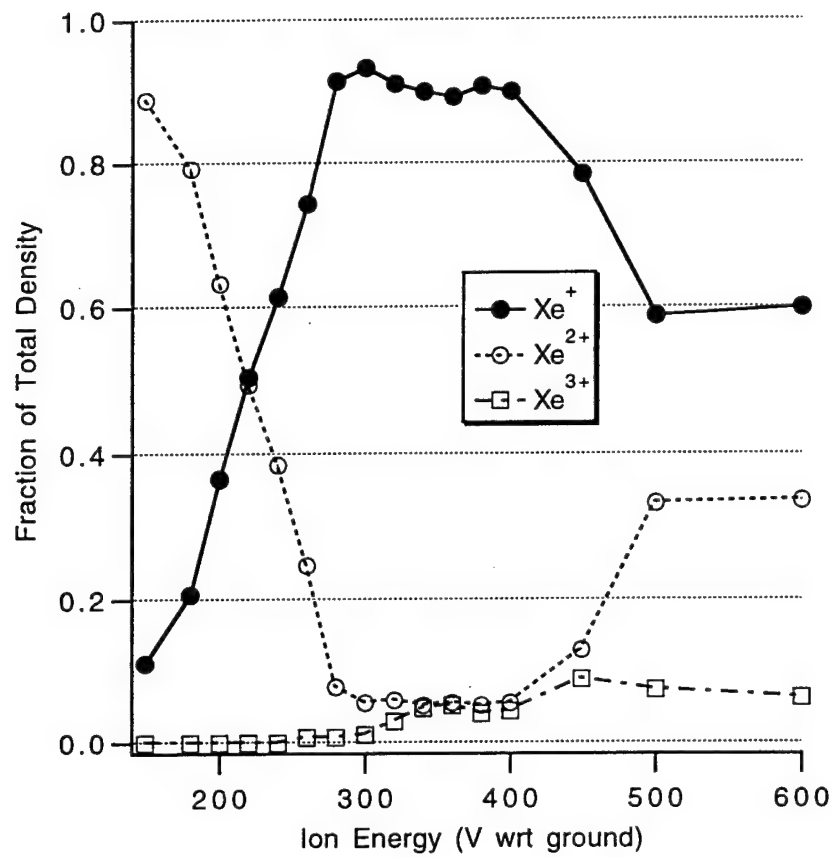


Fig. 9. Ionization budget of propellant species in D-55 at 10 degrees, 0.5-m-radius.

SECTION V: PROPAGATION CHARACTERISTICS OF AN ION ACOUSTIC WAVE IN A FLOWING PLASMA

Shawn G. Ohler, Brian E. Gilchrist, Alec D. Gallimore
University of Michigan, Ann Arbor, MI

Abstract

Ion acoustic wave propagation is characterized for excitation by a cylindrical wire probe in a flowing. The characterization provides the understanding necessary to develop a new diagnostic technique to estimate the flow velocity and the sum of electron and ion temperature. These quantities are important in understanding general plasma physics and specifically for characterizes electric propulsion thrusters. General propagation and excitation characteristics are explored by varying the probe size and stimulus potential in order to determine a reasonable experimental situation. The propagation characteristics are interpreted and compared with previous results which indicate a dependence on the probe wake in addition to the basic ion acoustic wave dispersion relation. The results have potential implication to wave-wake phenomena for spacecraft applications.

1• Introduction

Knowledge of plasma properties aids in understanding and evaluating the production and physical mechanisms of a plasma. Properties of particular importance in moving plasmas include the directed flow velocity and thermal velocities; quantities that directly affect the propagation of ion acoustic waves. Therefore, by characterizing and understanding ion acoustic wave propagation in flowing plasmas, a diagnostic technique that is simple and straight-forward can potentially be implemented to measure flow velocity, electron temperature, and ion temperature. In addition to implications as a basic diagnostic technique, characterization of ion acoustic wave excitation and propagation will improve general understanding of wave phenomena in flowing plasma, which has application in a number of fields of plasma science such as ionospheric and space studies, fusion, and electric propulsion.

Flow velocity and thermal velocities in electric propulsion thruster plasmas are important for evaluating thruster performance and operation. This study focuses on the stationary plasma thruster (SPT) plume which is a highly-focused plasma with a central core approximately 20 cm across where the density decreases gradually increases with distance from the source. The density is approximately 10^{16} m^{-3} at 1 m downstream on axis; the density can vary by more than an order of magnitude depending on position. The thruster operates primarily on xenon, but argon and krypton are used for additional comparison. The electron temperature is expected to be approximately 4 eV and the ion temperature 0.1 eV. The flow velocity depends on the gas propellant and the discharge voltage but is expected to be approximately 16 km/s. The magnetic field in the measurement region is below 10^{-3} T .

Previous diagnostic techniques have characterized flow velocity, electron temperature, and ion temperature. Electron temperature characterization is generally made easily and accurately with Langmuir probes. The flow velocity can be measured using either a retarding potential analyzer (RPA), an electrostatic quadrupole probe, Doppler analysis of a scattered wave, laser induced fluorescence (LIF), or using wave propagation characteristics. The RPA effectively obtains the energy distribution of the ions, but it is intrusive and does not directly measure the flow velocity [1]. An electrostatic quadrupole probe can simultaneously measure most quantities, but depends on very accurate knowledge of the probe-plasma interaction [2-5]. Doppler analysis is very accurate and non-intrusive, but the signal amplitude is extremely small in many instances [6, 7]. LIF has excellent spatial resolution, but depends on a complex energy level model and usually only measures a vector component of the flow velocity [8]. Wave propagation characterization does not have the limitations of probe plasma interaction, can be relatively non-intrusive, and relies on a simple theoretical basis. Previous use of wave propagation information has been implemented

using (1) the frequency domain characteristics of lower hybrid waves but this requires a strong magnetic field [9], and (2) the time-of-flight method to find the velocity of a wave in the plasma, but this method assumes a zero phase velocity to estimate the flow velocity [10].

The ion temperature has always been difficult to quantify. Previous methods have utilized the scattered wave information such as with Rutherford or Thompson scattering or using the Doppler spreading in LIF measurements. The scattering methods depend on an extremely small scattered signal, while LIF technique depends on a complex theoretical model and is restricted to regions of the plume near the thruster exit to ensure high signal-to-noise ratios [11-14]. An alternate method to estimate ion temperature could be through utilizing the propagation characteristics of an ion acoustic wave. By understanding the propagation pattern of an ion acoustic wave in a flowing plasma, the flow velocity and sum of the electron and ion temperature can be found through a simple analysis, relatively independent of probe-plasma coupling, and without ignoring the wave velocity.

This study investigates the propagation characteristics of an ion acoustic wave in relation to implementation of a diagnostic technique to measure flow velocity, electron temperature, and ion temperature. The results build upon previous research of ion acoustic wave propagation and research with probes in flowing plasmas. Initially, the theoretical basis of ion acoustic wave propagation is reviewed, and the current experimental conditions are summarized. The characterization results are presented as related to issues of excitation and propagation of ion acoustic waves. Finally, the results are summarized in a discussion which concludes with an evaluation of this technique.

2• Basic Theory

The dispersion relation (Equation 1 a and b) for an ion acoustic wave in a flowing plasma [15] provides the theoretical basis for a diagnostic technique that uses ion acoustic wave propagation characteristics to find plasma parameters.

$$V_{iaw} = \sqrt{\frac{KT_e + 3KT_i}{m_i}} \quad 1a$$

$$\frac{\omega}{k} = V_{tot} = V_{iaw} + \hat{k} \cdot V_{flow} \quad 1b$$

Propagation is explored through modeling excitation with an infinitesimally thin cylindrical probe. The general propagation characteristics are investigated and explained. Finally, possible propagation characterization is related to three plasma parameters: flow velocity, electron temperature, and ion temperature.

Exciter Characteristics

Ion acoustic waves can be excited by a metallic probe inserted in a plasma that is driven with an oscillating potential. The waves can be excited by a number of geometries: grids, spheres, bipolar probes, or cylindrical probes [16-19]. In this research, a small cylindrical wire probe (on the order of a Debye length in diameter) is used even though this geometry has a low coupling efficiency [16] in order to minimize both electrostatic and fluid dynamic disturbance. The probe height is chosen smaller than a wavelength so that it appears as a small monopole source which produces an electric field radially outward. The applied oscillator potential is maintained less than the floating potential (ion saturation region) in order to produce an ion sheath which minimizes the disturbance to the plasma. However, the amplitude is greater in magnitude than the electron temperature in order to produce a sheath oscillation which effectively launches an ion acoustic wave [20, 21].

Propagation Pattern

The radiation pattern for the wire probe is developed through a basic physical interpretation to qualitatively explain the measurement. The propagation pattern of the probe is evaluated in the

plane orthogonal to its length (see Figure 1) which is also the measurement plane. An ion acoustic wave is produced through a time-varying probe potential. When a potential is applied, a sheath forms a cylinder around the probe which is a few Debye lengths in thickness. Around the sheath, a presheath which can be many Debye lengths thick, launches the ion acoustic waves. The presheath electric field radiates radially outward from (or inward to) the probe producing a longitudinal ion acoustic wave radiating isotropically in the X-Z plane in a non-flowing plasma as in Figure 1.

On the other hand, in a flowing plasma, the pattern is skewed in the direction of the flow (see Figure 2). In a plasma moving slower than the wave velocity the wave is expanded (or Doppler shifted) in the direction of the flow and compressed in the direction opposite the flow. When the flow velocity is faster than the wave velocity, the wave cannot propagate opposite to the flow and is limited to a propagation zone which is defined by the wave velocity and flow velocity. The last case is of interest in this research.

Initially, the wave is excited (or radiates) isotropically from the source. After initial excitation, the wave propagates with the wave number which is determined by the vector sum of the ion acoustic wave velocity and the flow velocity (Equation 1b). With this model no propagation occurs opposite the flow. Propagation initiated orthogonal to the flow follows a path determined by the vector sum of the velocities where the angle of this vector defines the theoretical propagation zone of the wave (Figure 3). Lastly, propagation parallel to the flow direction moves with a velocity equal to the sum of the ion acoustic wave velocity and the flow velocity (Figure 4).

Determining Flow Velocity, Electron Temperature, and Ion Temperature

The velocity of both the ion acoustic wave and the plasma flow are found by quantifying the propagation along the two limiting directions: orthogonal and parallel to the flow. The wave propagation orthogonal to the flow follows a path that is the boundary of the propagation zone; experimentally determining the propagation zone (θ) defines the ratio of the two velocities (Equation 2). The wave propagating parallel to the flow is defined by the wavenumber and frequency which are directly related to the sum of the velocities through Equation 3. The wave is excited with a known frequency and the wavenumber is determined through a measurement of the wavelength. The two measurements uniquely determine the wave velocity and flow velocity.

$$\theta = \tan^{-1}(V_{iaw} / V_{flow}) \quad 2$$

$$\lambda = 2\pi(V_{flow} + V_{iaw}) / \omega \quad 3$$

Determining the wave velocity and flow velocity does not require knowledge that the electrostatic wave is an ion acoustic wave. The only assumption is that a coherent electrostatic wave propagates in the plasma, and it is superimposed onto the flowing plasma. By experimentally verifying that the electrostatic wave is an ion acoustic wave, additional information is obtained through the ion acoustic wave dispersion relation. The ion acoustic wave velocity is proportional to the sum of the electron and the ion temperatures. In our experimental situation the ion temperature is over an order of magnitude less than the electron temperature and hence can be approximated as zero in order to estimate the electron temperature from the phase velocity. The ion temperature can also be estimated if the electron temperature is found independently such as with a Langmuir probe. However, the ion temperature determination is very sensitive to the accuracy of electron temperature and phase velocity.

3• Experimental Description

The ion acoustic wave probe system is composed of three primary components: the positioning system, the exciter and detector probes, and the data acquisition system. The first two components are placed in a vacuum chamber. Probe characteristic are transmitted in and out of the chamber via coaxial cable to the data acquisition system which comprises a lock-in-amplifier and computer.

The stainless steel vacuum chamber used for these experiments is 9-m-long by 6-m-diameter and located in the Plasmadynamics and Electric Propulsion Laboratory (PEPL) at the University of Michigan. The vacuum facility is supported by six 0.81-m-diameter diffusion pumps each rated at 32,000 l/s on nitrogen and 5000 l/s on xenon, backed by two 2,000 cfm blowers, and four 400 cfm mechanical pumps. The experimental facilities are described in more detail in Gallimore [22].

A state-of-the-art probe positioning system provides the capability to spatially map plume parameters. The system is driven and monitored with a computer. The positioning system is mounted on a movable platform to allow for measurements to be made throughout the chamber. The positioning system contains two linear stages with 0.9 m of travel in the axial direction and 1.5 m of travel in the radial direction. The axial direction, shown in Figure 5, is along the axis of the thruster. The radial axis indicates the direction orthogonal to the plane created by the thruster axis and the probe axis.

The probes used for excitation and detection of voltage signals are oriented orthogonal to the direction of the flow (vertically). One stationary and one movable probe (Figure 5) allow detailed spatial mapping of the propagation characteristics in the plane orthogonal to the probe axis. In all cases a tungsten wire is fed through a ceramic or Teflon insulator and connected to RG-58 coaxial cable which is protected and supported in a metal shield (see Figure 6). The tungsten wires vary in thickness from 0.12 to 2.64 mm outer diameter and from 0.2 to 2.1 cm long. The outer diameter of the insulator is 2-4 times the outer diameter of the wire and the metal shield is stainless steel tubing. The stainless steel tube is connected to ground via the support structure which is either connected to the positioning table for the movable probe or the chamber floor for the stationary probe.

The primary measurement system consists of a lock-in-amplifier (Stanford Research Systems SR850) connected to a computer via GPIB and controlled through LabView software. The lock-in-amplifier acts as a sensitive transmitter and receiver through digital control of the transmitted signal and digital filtering of the received signal. The processing capabilities include filtering with better than 0.1 Hz bandwidth and 18 dB/octave attenuation. This allows for the detection of an extremely small signal in the noisy and relatively large ambient voltage signal. The excitation signal from the lock-in-amplifier has a maximum peak-to-peak voltage of ± 5 V and testing is reported in the frequency range of 1 to 100 kHz (maximum frequency of this lock-in-amplifier model). Excitation voltage amplitude and bias levels outside of the lock-in-amplifier range are obtained through the use of an operational amplifier and DC power supply.

4• Plasma Source: Stationary Plasma Thrusters

For the development of the ion acoustic wave diagnostic, two SPTs have been studied (Figure 7), the Fakel SPT-100 and Moscow Aviation Institute (MAI) laboratory-model SPT, both built in Russia. The primary thruster, an SPT-100, is a commercial grade flight model closed-drift Hall thruster built by the Russian Fakel Enterprises that is on loan from Space System/Loral and previously tested by NASA Lewis [8, 23-26] as well as others. This thruster is operated with xenon propellant at nominal operating conditions of 300 V anode-cathode potential, 4.5 A discharge current, 5.0 mg/s through the anode, and 0.56 mg/s through the cathode.

The second engine is a laboratory-model device that is similar to the Fakel thruster but has not been refined for flight qualification status. This thruster is operated with either argon, krypton, or xenon propellant with flow rates of 2 to 5 mg/s through the anode, and 0.3 to 0.8 mg/s through the cathode. The electrical inputs include voltage applied to the anode, cathode, and ignitor and the current applied to the heater, inner magnet coil, and outer magnet coil. A range of operating conditions existed for the electrical parameters. The cathode-anode discharge potential is between 120 and 310 V with a discharge current of 3 to 5 A. The ignitor is floating during operation with a potential between 15-1000 V necessary to ignite the discharge. The heater current is 8 A, and the inner and outer magnets are set between 2 to 4 A.

In order to verify operation in the ion saturation region, the floating potential has been monitored in each test. Measurement with a voltmeter indicates the floating potential, for both the Fakel and MAI thrusters, varies between +4 to +8 V which is dependent upon the operating conditions and propellant.

In addition to the floating potential, the plasma noise characteristics are also measured in terms of the voltage noise characteristics on the floating probe. Natural plasma oscillations can degrade the signal that the lock-in amplifier receives. In addition to signal degradation, the natural oscillations of the plasma could potentially damp the excited ion acoustic wave and make characterization of the propagation characteristics difficult. The natural oscillations of the plasma are measured by connecting the probe via coaxial cable to an oscilloscope with high input impedance. The frequency components of the plasma oscillations show the dominant frequency of both thrusters to be between 20 to 30 kHz as expected from the microwave measurements of the Fakel SPT-100 [27]. Hence, frequencies near this range should not be used for excitation, propagation, and detection of ion acoustic waves.

5• Results

Ion acoustic wave excitation, propagation, and detection are characterized in this work through comparison and evaluation of different experimental situations. Initially, the plasma is characterized in terms of the floating potential and plasma noise. This supplements the general plasma parameters measured in other investigations (see earlier sections of this report): electron density, electron temperature, ion temperature, and collision frequencies. Next general propagation patterns are discussed to provide an overview of probe-plasma coupling characteristics. The probe-plasma coupling is evaluated through separate comparison of detection characteristics for different excitation potentials, probe sizes, and excitation frequencies. Lastly, detection characteristics are presented for a number of thruster propellants. A summary of the tests to characterize ion acoustic wave excitation and propagation is listed in Table 1.

General Ion Acoustic Wave Characterization

A general idea of the propagation characteristics is necessary in order to understand the comparisons of various experimental information in the following sections. Measurements are presented that have been taken using the MAI thruster (krypton, 120 V, 3.3 A). The stationary probe is approximately on the thruster centerline 1 m from the exit plane. The movable probe is swept spatially over a range of axial and radial positions with respect to the stationary probe in order to characterize the amplitude and phase spatial variation.

An ion acoustic wave coupled into a mesosonic plasma would ideally only propagate downstream. Experiments verified that, indeed, propagation only occurred downstream; however, slight disturbances are detected for a short distance upstream which is thought to be near-zone presheath coupling. The measured characteristics upstream are essentially noise as indicated by low voltage amplitude and erratic voltage and phase.

Downstream of the excitation signal the wave generally propagates with decreasing amplitude in a cone radiating from the exciter which has previously been referred to as the propagation zone (Figure 2). The edge of the cone in the far-zone (>5 cm) is determined by the ion acoustic wave velocity and the plasma flow velocity. In general, the amplitude of the ion acoustic wave is primarily proportional to the number density since electrostatic coupling through the particles produces the ion acoustic wave. Another prominent feature is the interference pattern (or amplitude nulls) in the radial direction which also propagates outward from the exciter. Nulls also occurs in the axial direction very close to the excitation source where, in addition to the nulls, two large peaks in amplitude occur (Figure 8). The peak in the propagation pattern generally occurs in the direction of the flow. In Figure 8, the peak is slightly off axis ($\sim 0.5^\circ$), but is within the alignment accuracy of the measurements.

The spatial change in the phase tracks closely to amplitude variation. Radially from the center, the phase changes gradually except near the amplitude nulls where 180° changes in phase occur. The phase decrease along centerline in the far-zone (for increasing separation) corresponds to the expected phase shift of a propagating wave moving at a velocity which is the sum of the ion acoustic wave and the flow velocity. Near the edges of the propagation zone the phase is erratic, indicative of no propagation in that region. The interference pattern exhibited in the ion acoustic

wave measurements is attributed to the wake of the excitation probe and is discussed in the following section after further results are presented.

Figures 9 and 10 show the variation of radial and axial phase of an ion acoustic wave in the plasma of the MAI thruster. As Figure 10 shows, the convected wave velocity remains constant beyond approximately 10 cm downstream of the thruster. This provides the rough boundary for which this technique may be employed.

Excitation Potential and Probe Size

In order to qualitatively determine acceptable excitation voltages, a range of signal magnitude and bias levels have been tested (± 5 , ± 10 , ± 20 , ± 40). The tests indicate coupling effectiveness and dependence on excitation through comparison for different excitations of amplitude and phase of the detected signal. The measurements have demonstrated strong dependence of the received voltage amplitude on excitation amplitude in the near-zone but much less dependence on excitation amplitude in the far-zone. As expected, the higher amplitude excitations generally produce higher detected signals. The phase exhibited little change for various excitation levels in both regions. Differences primarily occur in the near-zone where wake effects and probe excitation levels have the greatest influence. Lower voltage levels have been tested with similar trends as are exhibited by the higher voltage levels.

The bias voltage variation testing is recorded for ± 5 V amplitude and 3 bias levels: 0 V, -10 V, and -30 V. No positive bias levels were tested due to the desire to remain biased in the ion saturation region. (Biasing in the ion saturation region minimizes plasma perturbation and a wake effect.) The tests have been completed using the SPT-100 thruster with xenon propellant and operating at 300 V and 4.5 A. The received signal is affected less by excitation bias voltage than for excitation amplitude. For the purposes of this study, the trends in all three cases are similar for both amplitude and phase with the most significant variation in the near-zone region.

Various probe sizes have also been tested to qualitatively determine how probe size affects the excitation and detection of the ion acoustic wave. In the first experiment, four tungsten wire probes are tested, the size of each is listed in Table 2 (Probes 1 to 4). The MAI thruster is operated with krypton at 120 V and 3.4 A. As expected, the larger probes are more effective at detecting the voltage variation of the ion acoustic wave; however, the relationship is not directly related to the area of the probe. For instance, an increase in area by a factor, M , produces less than a factor M increase in detected amplitude. The phase, on the other hand, does not exhibit significant difference between probes except for Probe 4 which is much shorter than the other three. In general, a range of probe sizes are acceptable for the detector probe given amplitude and phase considerations.

In the second experiment, two tungsten probes are compared as exciters where the sizes are listed in Table 2 (Probe 5 and 6). In this test the SPT-100 thruster is operated with xenon at 300 V and 4.5 A. For both probes the amplitude and phase follow the same trends as the previous experiment. However, the probe area ratio is much larger in this experiment; therefore, as expected, the amplitude and phase difference is larger. The amplitude differs by a factor of 4 to 5; however, the amplitude ratio is still not as large as the area ratio. The phase in this experiment, for both the small and large probe, exhibit the same differential spatial change. However, the difference in probe size produces a phase shift in the detected signal.

Additional measurements of the amplitude variation in the radial direction highlight the wake effect that is measurable with the larger probe. Radial sweeps have been recorded at ten axial positions. These measurements have been recorded for the SPT-100.

The near-zone character demonstrated in the measurements resolve the null in the signal directly behind the probe where no particles are present (direct wake region). This null transforms into the main lobe observed in the downstream measurements also indicated in Figure 11 which is typical of wakes behind cylindrical probes [28-33]. In the mid- to far- zone region the amplitude signal does not decay as would be expected for a wake response, rather it propagates as would be expected of an ion acoustic wave. The far-zone wave pattern is that of an ion acoustic wave in a flowing plasma with the amplitude modified by the near-zone wake amplitude pattern.

Excitation Frequency

A number of different probe excitation frequencies (3.2 kHz to 100 kHz) were tested in order to determine the effect of excitation frequency on the results and also to characterize the dispersion relation for an ion acoustic wave (Figure 12). In this test, the MAI thruster was operated with xenon at 278 V and 4.9 A and tungsten wire probes are used with 0.22 mm outer diameter and 1 cm long. The probes were approximately on the centerline of the thruster, hence they were aligned along the flow axis.

All frequencies follow similar trends in amplitude with a strong peak and null followed by a region where the amplitude slowly decreases out to the farthest measurement point. The detected amplitude varies linearly with frequency where the highest frequency produces the lowest amplitude; however, even the highest test frequency excites a wave well within the resolving capability of the lock-in amplifier. The higher frequencies are desirable due to the noise characteristics of the SPTs which peaks at 26 kHz [34].

The phase also exhibits similar characteristics across the frequency range with more noisy phase measurements in the near-zone where the probe still has an effect and in the farthest measurement points where the amplitude is lowest (Figure 11). Phase jumps occur at the same separation distance as the nulls in the amplitude for all of the frequencies. Aside from the phase jump at 8 cm, the phase progresses at a constant rate for each of the tests for distances greater than 2.5 cm (near-zone). The phase shift is higher over the same distance for higher frequencies as would be expected. At the lowest frequencies, characterizing the phase change per distance is difficult due to the small phase shift even over the large measurement range.

Characterization of Phase Shift and Propagation Zone

The amplitude variation both radially and axially has been found in the MAI thruster plume using three different propellants. Similar operating conditions have been used for each of the three gases: argon, 310 V, 3.8 A; krypton, 298 V, 4.5 A; and xenon, 278 V, 4.9 A. This test also used tungsten wire probes 0.22 mm thick and 1 cm long.

The phase variation with probe separation (Figure 13) is measured at 50 kHz and up to 50 cm probe separation. For measurements past the near-zone (~5 cm), the phase velocity (slope of the line) is constant except for the phase jump at 7 to 10 cm. The measurements indicate a progressively noisier signal for lighter gases. This would be expected since the SPT operates more effectively with the heavier particles (such as xenon). The comparison demonstrates the expected trend of a slower velocity for the heavier propellants as would be expected with comparable discharge potentials.

The amplitude contours for the three gases are developed from eight to ten radial spatial sweeps at axial distances on centerline ranging from every 0.25 cm to 40 cm (depending on which trial). A sample data set is shown in Figure 14 for xenon. The radial sampling ranged from 4 data points/cm at the center to 0.8 data points/cm at the edges of the sweep. Reference lines highlight the important features including peak, nulls, and signal edges.

Each of the reference lines is extracted directly from the raw data. The peak is the maximum amplitude for each radial sweep. The nulls are the first minimum to either side of the peak. The signal edge is the approximate point where the amplitude decreases to the noise level in each plot.

A number of factors contribute to uncertainty or variation in the measurements. Due to the limited spatial sampling in the measurements, identification of the three quantities (peaks, nulls, signal edges) is generally accurate to only ± 0.5 cm within each data set. Additional uncertainty exists in the absolute position relative to other data sets. The position uncertainty accounts for the deviation in individual points and also the shift in all three quantities for a number of data sets. Lastly, in the farthest measurement points, plasma non-homogeneity could cause slight aberration in the measurements.

The general trends are consistent in all three data sets. First, the peak propagation is slightly off center indicating a slight angle with respect to the flow. The null point tends to expand away from the peak, but not as quickly as the signal edge. Finally, the signal edge angles out sharply in the near-zone, but quickly assumes a smaller expansion rate in the far-zone. Comparison of all three

data sets leads to the observation that in the far-zone the propagation expands at approximately equal angles which is independent of the propellant.

6• Analysis and Summary

The results just presented characterize ion acoustic wave propagation in a SPT plume and provide information helpful in developing a simple method to utilize the propagation characteristics to ascertain flow velocity, electron temperature, and estimate ion temperature. First, the wake-wave pattern is discussed in more detail in order to determine what information can be derived from the propagation pattern. Then, the spatial mapping of amplitude and phase is utilized in order to estimate plasma flow velocity, ion acoustic wave velocity, and the sum of the plasma thermal temperatures. Finally, the results are utilized to affirm the presence of an ion acoustic wave in this plasma (as opposed to assuming this fact *a priori*), establish acceptable excitation levels and probe size, and establish the region over which ion acoustic wave propagation is consistent.

Discussion of Wake-Wave Pattern

The wake-wave interference pattern exhibited in the propagation characteristics close to the excitation probe (<5 cm) are very similar to the results reported in studies of the wakes behind small cylindrical probes in a flowing plasma. Previous work has studied wake structure through both theoretical modeling [35-39] and experimental investigation [28-33]. Additional work related to the observed wave pattern has studied near-field interference patterns of antennas exciting ion acoustic waves [40, 41]. The studies have been reported in plasmas with similar temperature ratios ($T_e / T_i \approx 10$) and velocity ratios ($V_{flow} / V_{iaw} \approx 10$) when compared to the expected plasma parameters in this study. The previous wake studies demonstrated that the density perturbation is measurable behind even a small probe in a region up to 100 times the probe diameter [28, 31]. The mechanism of disturbance for the wake studies are primarily a fluid effect and not a result of a varying electrostatic signal on the probe. Also, in the wake studies, the ratio of the ion acoustic velocity to the plasma flow velocity determined the shape of the wake cone; however, for cylindrical probes the edge of the cone is not necessarily directly related to the velocity ratio where the wake angle is larger than predicted by the ratio of the velocities [31].

The ion acoustic wave pattern is similar to the wake studies in a number of ways in the near-zone where the similarities are most evident in the results for characterization of the largest probe. In particular, the null directly behind the probe is measured just as in wake studies where the axial position of the null is related to the probe size, flow velocity, and ion acoustic wave velocity. The trends are also similar in the formation of the initial main lobe which evolve into side lobes as the wave moves downstream. In addition to the studies with the large probe which spatially characterizes the propagation pattern, indicate that close to the probe the expansion angle is significantly larger than in the far-zone where in this study, the expansion angle is thought to be dominated by the ion acoustic wave propagation expansion angle.

As just stated, the interference pattern close to the excitation probe is similar to the pattern of the wake behind a cylindrical probe; however, the differences are significant farther than 50 probe diameters from the probe. In the near-zone for both the wake experiments and this study, a null in the center directly behind the probe is found to progress into the main lobe with two side peaks just as the wake structure would predict. However, in the wake studies for distance greater than 50 probe diameters the lobe structure decays significantly, while in this study, the propagation pattern persists to the limit of the measurements (up to 1000 diameters). This result indicates that the near-zone of the probe wake significantly affects the wave amplitude. However, in the far-zone the expansion of the propagation is determined by the ion acoustic wave propagation. The nulls in the propagation pattern are therefore a consequence of the near-zone interference pattern produced by the wake of the probe. Additionally, the edge of the propagation zone in the far-zone is determined solely by the ion acoustic wave, since the wake region as seen in the near-zone is actually expected to expand at a greater angle than the ion acoustic wave.

To summarize the results of the ion acoustic wave characterization, the excitation and propagation of a wave can be divided into four regions as shown in Figure 15: presheath region,

wake region, near-zone region, and far-zone region. A sinusoidally varying probe potential produces an oscillating sheath and presheath. The presheath region launches the ion acoustic wave into the plasma. The region directly downstream of the probe is shielded; hence, no particles exist in this region. After the wave is launched by the presheath, the wake of the probe produces an interference pattern dependent on the probe size, plasma density, thermal temperatures, and flow velocity. The wake-interference pattern is a density disturbance that attenuates quickly in comparison to the ion acoustic wave propagation; however, the coupling effect of the wake-interference pattern partially determines the ion acoustic wave propagation pattern in the far-zone (since the ion acoustic wave amplitude is proportional to particle density). In the far-zone the wave propagates as a normal ion acoustic wave in a flowing plasma where the amplitude distribution is determined by the near-zone interference pattern.

Plasma Parameters Calculations Using Spatial Characterization of Propagation

Phase data can be used to find the wavelength and total velocity of the ion acoustic wave that is superimposed on the flowing plasma. Using the data from Figure 13 these quantities are found from a linear fit to the phase over the region from 11 to 50 cm separation. The slope of the linear fit is related to the wavelength through Equation 4 since the slope is just the unit change in phase over distance.

$$\lambda = \frac{360^\circ}{\Delta\phi} d = \frac{360^\circ}{\text{slope}} \quad 4$$

The drift velocity of the plasma is assumed to be constant with respect to excitation frequency; therefore, any difference in total wave velocity as a function of the frequency would be due to velocity difference in the excited wave. However, the measurements summarized in Table 4 show a constant velocity at all frequencies within the expected accuracy of the measurement. Therefore, the results are consistent with the constant phase velocity expected from an ion acoustic wave. Overall, the individual measurements are within $\pm 15\%$ of the average velocity value for xenon propellant. Additional measurements using argon and krypton propellants are also consistent with these findings where each gas has an average velocity constant as a function of excitation frequency. In addition to measurement noise, one possible source of error in these measurements is misalignment with the flow axis which would produce a smaller slope in the phase data thus inflating the velocity calculation by up to 15% frequencies.

As discussed earlier, in order to find the flow velocity and the ion acoustic wave phase velocity, two measurements are necessary: phase variation along flow axis, and amplitude variation in the radial direction. As just demonstrated, the spatial phase variation provides information concerning the sum of the two velocities. Furthermore, the radial amplitude variation provides the information necessary to determine the edge of the propagation zone.

The propagation zone edge is found from the data such as in Figure 14. The accuracy of the interpretation is limited due to the lack of spatial sampling in these measurements. An expansion angle is determined for each radial sweep by taking half the angle formed by two far-zone edge points and the exciter position. This angle is not precisely the expansion angle since the near-zone expansion creates a small offset. However, the difference in the two angles is within the accuracy of the propagation zone edge determination ($\pm 1.5^\circ$). The average angle in the far-zone is given in Table 5 for each of the three propellants tested. All of the individual angles are within $\pm 1.5^\circ$ of the averages. The expansion angle is related to the ratio of the velocities by Equation 2. The slope of the phase versus distance are calculated using the data from Figure 13 for the three gases, and they are also listed in Table 5. These measurements provide the information to find the plasma flow velocity and ion acoustic wave velocity. Additionally, the ion acoustic phase velocity and dispersion relation yields the sum of the electron and ion temperatures.

The trends in the results are not surprising. The flow velocity and ion acoustic wave velocity decrease with increases in propellant mass. The velocities are slightly higher than expected, but still within the uncertainty of the technique. The plasma flow velocity is similar to other published

measurements for SPTs running on xenon which report velocities between 13 and 18 km/s [8]. Also, the sum of electron temperature and ion temperatures in Table 5 is also similar to previous results which report electron temperatures between 1 to 6 eV and ion temperature of 0.1 eV [25, 26, 42, 43]. Additionally the wave expansion angle is approximately the same for all three propellants. This would be expected since in the far-zone the propagation expands at an angle proportional to the ratio of the ion acoustic velocity to the directed flow velocity. Both velocities are proportional to the inverse square root of the mass; therefore, the expansion angle should be independent of propellant mass given similar electron temperature and accelerating voltage.

Summary of Wave Propagation Studies

The experiments and calculations in this section describe ion acoustic wave propagation in flowing plasma, in particular, in the plume of a SPT. In order to develop an effective diagnostic technique, the results are summarized as applied to three questions. Does a coherent ion acoustic propagate in the plume? What probe geometry and signal will effectively excite and detect ion acoustic waves? Lastly, for what exciter-detector separation distances are the propagation parameter meaningful and resolvable?

The coherent propagation of an ion acoustic wave was established through multiple corroborating experiments. Initially, experiments confirmed the type of excited wave as an electrostatic wave moving slower than the flow velocity since no signal is detected upstream of the exciter. Additionally, the velocity was found to be constant across the frequency spectrum which is in agreement with the dispersion relation of an ion acoustic wave. Moreover, the propagation pattern in the far-zone cannot be solely explained from the wake of the probe but was explained by ion acoustic wave propagation. Lastly, the flow velocity and electron temperature found from the phase shift and propagation zone measurements was consistent with previous results for the SPT. Therefore, the experiments have established the propagation of an ion acoustic wave.

The effect on the excitation and detection of the ion acoustic wave has been explored for a number of excitation amplitude and bias voltage. Differences in propagation characteristics between excitation levels were greatest in the near-zone of the probes; however, in the far-zone differences between excitation levels were small. The excitation voltage was chosen to maintain simplicity and minimize noise from other components; therefore, the majority of testing used the lock-in amplifier directly as the excitation source where the maximum peak-to-peak voltage is $\pm 5V$.

The experiments with exciter and detector probes of varying sizes indicated that a wide range of probe sizes work effectively in terms of acceptable amplitude and phase measurements (Section 6.2.4). A larger probe was attractive due to its increased signal amplitude. However, a smaller probe produces a smaller wake region which was important in order to utilize the propagation information. For typical SPT plume densities, probes greater than 0.2 mm and less than 1 mm in diameter will excite and detect ion acoustic waves with sufficient amplitude to obtain good resolution with a lock-in amplifier and still limit the wake region to less than 5 cm. In general, no phase bias was exhibited by probes of similar size.

The excitation frequencies were tested up to 100 kHz (maximum frequency of the available lock-in amplifier). The lower frequency signals produce a larger amplitude signal, but the higher frequencies produce a larger phase shift. Additionally, for the SPT plume, the noise power spectral density peaks between 20 to 30 kHz and decreases for increasing frequency. Since the ion acoustic wave oscillations are physically similar to the natural oscillations, the excitation frequencies should be chosen with low noise and interference. In the range available, the frequencies above 50 kHz provide sufficient phase shift and amplitude to produce good measurement resolution. However, note that in these experiments the maximum frequency was determined by the capabilities of the lock-in-amplifier.

In order to optimize spatial resolution of the plume diagnostic, the acceptable detector distance from the exciter should be minimized. In this case, the spatial mapping provides the information necessary to qualitatively determine a minimum acceptable distance. The spatial mapping was implemented by linear radial sweeps in axial planes. This provided general information about the ion acoustic wave. However, for characterization of the propagation zone, the characterization should be implemented for a constant distance from the excitation probe in order to more closely

follow an equi-phase contour of the spherical wave emanating from the probe. Additionally, the sampling resolution should be much finer than used in Section 6.2 in order to accurately determine the propagation zone edge. Given the good consistency in the propagation pattern, the characterization can be implemented at a single distance from the excitation probe. The phase shift can also be sampled at two distances to get an estimate of the phase shift.

The spatial characterization of the MAI thruster and SPT-100 thrusters has established an area of consistent propagation where more limited spatial characterization is sufficient to obtain necessary information. For the MAI thruster, measurements 10 cm or farther downstream will yield consistent results. For the SPT-100, thruster measurements 5 cm downstream will yield consistent results. The longer distance for the MAI thruster is primarily due to a null in the amplitude pattern at approximately 7 cm. For a given plasma source and probe configuration, a limited axially characterization provides sufficient information necessary to determine a minimum acceptable detector distance.

Acknowledgments

The authors would like to thank several of the students at PEPL including S.W. Kim, J. Haas, M. Domonkos, C. Marrese, J. Foster, and L. King whose help was much appreciated. We also wish to thank M. Day of Space Systems/Loral for the loan of the Fakel thruster and Dr. S. Khartov of the Moscow Aviation Institute for the loan of the lab-model SPT.

Section V References

1. Marrese, C., *et al.*, An Investigation of Stationary Plasma Thruster Performance with Krypton Propellant, paper AIAA 95-2932 presented at *31st AIAA/ASME/SAE/ASEE Joint Propulsion Conference and Exhibit*, San Diego, CA, 1995.
2. Poissant, G. and M. Dudeck, Velocity Profiles in a Rarefied Argon Plasma Stream by Crossed Electrostatic Probes, *Journal of Applied Physics*, **58**, , 5, 1772-1779, 1985.
3. Johnson, B. and D. Murphree, Plasma Velocity Determination by Electrostatic Probes, *AIAA Journal*, **7**, , 10, 2028 - 2010, 1969.
4. Burton, R.L., S.G. DelMedico, and J.C. Andrews, Application of a Quadruple Probe Technique to MPD Thruster Plume Measurements, *Journal of Propulsion and Power*, **9**, , 5, 771-777, 1993.
5. Bufton, S., R. Burton, and H. Krier, Measured Plasma Properties at the Exit Plane of a 1 kW Arcjet, paper AIAA 95-3066 presented at *31st AIAA/ASME/SAE/ASEE Joint Propulsion Conference and Exhibit*, San Diego, CA, 1995.
6. Erwin, D.A., G.C. Pham-Van-Diep, and W.D. Deininger, Laser-Induced Fluorescence Measurements of Flow Velocity in High-Power Arcjet Thruster Plumes, *AIAA Journal*, **29**, , 8, 1298-1302, 1991.
7. Storm, P. and M. Cappelli, Laser-Induced Fluorescence Measurements Within an Arcjet Thruster Nozzle, paper 95-2381 presented at *31st AIAA/ASME/SAE/ASEE Joint Propulsion Conference and Exhibit*, San Diego, CA, 1995.
8. Manzella, D., Stationary Plasma Thruster Ion Velocity Distribution, paper 94-3141 presented at *30th AIAA/ASME/SAE/ASEE Joint Propulsion Conference*, Indianapolis, IN, 1994.

9. Diamant, K., *et al.*, MPD Thruster Exhaust Velocity Measurement Using Injected Plasma Waves, paper 91-049 presented at AIDAA/AIAA/DGLR/ JSASS 22nd International Electric Propulsion Conference, Viareggio, Italy, 1991.
10. Boyle, M.J., *Acceleration Processes in the Quasi-Steady Magnetoplasma dynamic Discharge*, Princeton University, 1974.
11. Hutchinson, I.H., *Principles of Plasma Diagnostics*, Cambridge University Press, New York, 1987.
12. Haddad, E., *et al.*, Spectroscopic Measurements of Tokamak Plasma Ion Temperature Using Doppler Broadening of Impurity Lines: Correction for Chordal Line-of-Sight Observations, *Journal of Applied Physics*, **69**, , 4, 1968-1973, 1990.
13. van Blokland, A.A.E., *et al.*, Ion Temperature Measurements in Tokamak Plasmas by Rutherford Scattering, *Review of Scientific Instruments*, **63**, , 6, 3359-3368, 1992.
14. Vickrey, J.F., *Incoherent Scatter Theory-- An Intuitive Approach*, Radio Physics Laboratory, SRI International, 1980.
15. Jones, W.D., *An Introduction to the Linear Theories and Methods of Electrostatic Waves in Plasmas*, Plasma Press, New York, 1985.
16. Chen, T. and L. Schott, *Excitation of Ion Acoustic Waves with Probes*, in *The Physics of Fluids*, p. 844-850, 1977.
17. Gould, R., *Excitation of Ion-Acoustic Waves*, *Physical Review*, **136**, , 4 A, 991-A997, 1964.
18. Nakamura, Y., T. Ito, and K. Koga, *Excitation and Reflection of Ion-Acoustic Waves by a Gridded Plate and Metal Disk*, *The Journal of Plasma Physics*, **49**, , 2, 331-339, 1993.
19. Schott, L., *Ion-Energy Measurements in a Double Plasma Device*, *Canadian Journal of Physics*, **70**, , 345-351, 1992.
20. Widner, M., *et al.*, Ion Acoustic Wave Excitation and Ion Sheath Evolution, *The Physics of Fluids*, **13**, , 10, 2532-2540, 1970.
21. Hong, M. and G. Emmert, *Two-Dimensional Fluid Modeling of Time-Dependent Plasma Sheath*, *Journal of Vacuum Science Technology B*, **12**, , 2, 889-896, 1994.
22. Gallimore, A., *et al.*, Near and Far-Field Plume Studies of a 1 kW Arcjet, paper 94-3137 presented at 30th AIAA/ASMA/SAE/ASEE Joint Propulsion Conference, Indianapolis, IN, 1994.
23. Absalamov, S.K., *et al.*, Measurement of Plasma Parameters in the Stationary Plasma Thruster (SPT-100) Plume and its Effect on Spacecraft Components, paper AIAA-92-3156 presented at 28th Joint Propulsion Conference and Exhibit, Nashville, TN, 1992.
24. Manzella, D.H., *Stationary Plasma Thruster Plume Emissions*, paper 93-097 presented at 23rd International Electric Propulsion Conference, Seattle, WA, 1993.
25. Manzella, D. and J. Sankovic, *Hall Thruster Ion Beam Characterization*, paper 95-2927 presented at 31st AIAA/ASME/ASEE Joint Propulsion Conference and Exhibit, San Diego, CA, 1995.

26. Myers, R.M. and D.H. Manzella, Stationary Plasma Thruster Plume Characteristics, paper 93-096 presented at *23rd International Electric Propulsion Conference*, Seattle, WA, 1993.
27. Ohler, S.G., B.E. Gilchrist, and A.D. Gallimore, Non-intrusive electron number density measurements in the plume of a 1 kW arcjet using a modern microwave interferometer, *IEEE Transactions on Plasma Science*, **23**, , 3, 428-435, 1995.
28. Fournier, G. and D. Pigache, Wakes in Collisionless Plasma, *The Physics of Fluids*, **18**, , 11, 1443-1453, 1975.
29. Chan, C., M.A. Morgan, and R.C. Allen, Electron Dynamics in the Near Wake of a Conducting Body, *IEEE Transaction on Plasma Science*, **PS-14**, , 6, 915-924, 1986.
30. Morgan, M., *et al.*, The Dynamics of Charged Particles in the Near Wake of a Very Negatively Charged Body - Laboratory Experiment and Numerical Simulation, *IEEE Transactions on Plasma Science*, **17**, , 2, 220-227, 1989.
31. Stone, N., The Plasma Wake of Mesosonic Conducting Bodies., *Journal of Plasma Physics*, **25**, , 3, 351-371, 1981.
32. Stone, N., W. Oran, and U. Samir, Collisionless Plasma Flow Over a Conducting Sphere, *Planet Space Sciences*, **20**, , 1787-1790, 1972.
33. Stone, N., U. Samir, and W. Oran, Laboratory Simulation of the Structure of Disturbed Zones Around Bodies in Space, *Journal of Atmospheric and Terrestrial Physics*, **36**, , 253-260, 1974.
34. Ohler, S., B. Gilchrist, and A. Gallimore, Microwave Plume Measurements of an SPT-100 Using Xenon and a Laboratory Model SPT Using Krypton, paper AIAA 95-2931 presented at *31st AIAA/ASME/SAE/ASEE Joint Propulsion Conference and Exhibit*, San Diego, CA, 1995.
35. Senbetu, L. and J. Henley, Distribution of Plasma Density and Potential Around a Mesothermal Ionospheric Object, *Journal of Geophysical Research*, **94**, , A5, 5441-5448, 1989.
36. Taylor, J., Disturbance of a Rarefied Plasma by a Supersonic Body on the Basis of the Poisson-Vlasov Equations - I, *Planetary Space Sciences*, **15**, , 155-187, 1967.
37. Konemann, B., The Collisionless Flow of Unmagnetized Plasmas Around Bodies, *Journal of Plasma Physics*, **20**, , 17-30, 1978.
38. Coggiola, E. and A. Soubeyran, Mesothermal Plasma Flow Around a Negatively Wake Side Biased Cylinder, *Journal of Geophysical Research*, **96**, , A5, 7613-7621, 1991.
39. Biasca, R. and J. Wang, Ion Current Collection in Spacecraft Wakes, *Physics of Plasmas*, **2**, , 1, 280-288, 1995.
40. Nakamura, Y., Y. Nomura, and K. Lonngren, Near Field and Damping Effects of the Radiation of Ion Acoustic Waves from Antennas, *Radio Science*, **14**, , 6, 1175-1181, 1979.
41. Christensen, T. and N. Hershkowitz, Near Field Diffraction Pattern of Ion Acoustic Waves, in *The Physics of Fluids*, p. 840-843, 1977.
42. Patterson, M.J., *et al.*, Experimental Investigation of a Closed-Drift Thruster, paper 85-2060 presented at *AIAA/DGLR/JSASS 18th International Electric Propulsion Conference*, Alexandria, VA, 1985.

43. Szabo, J. and J. Pollard, A Laboratory-Scale Hall Thruster, paper 95-2926 presented at *31st AIAA/ASME/SAE/ASEE Joint Propulsion Conference and Exhibit*, San Diego, CA, 1995.

Parameter	Parameter Set	Axial Spatial Mapping (cm)	Radial Spatial Mapping (cm)
General Propagation	NA	-3 to +3	0 to +25
Excitation Amplitude (V)	± 5 to ± 40	0 to +25	-3 to +3
Excitation Bias (V)	0 to -30	0 to +25	NA
Detector Probe Size (diameter, cm)	0.022 to 0.083	0 to 33	NA
Exciter Probe Size (diameter, cm)	0.046 to 0.26	0 to 25	-7 to +7
Excitation Frequency (kHz)	3.2 to 100	0 to +51	NA
Plasma Species	Ar, Kr, Xe	0 to +40	-5 to 3

Table 1. Summary of experiments to characterize ion acoustic wave excitation and propagation.

	Outer Diameter (cm)	Length (cm)
Probe 1	0.083	1.0
Probe 2	0.022	1.0
Probe 3	0.012	1.0
Probe 4	0.022	0.02
Probe 5	0.26	2.1
Probe 6	0.046	0.83

Table 2. Detector probe dimensions for first probe experiment.

Frequency (kHz)	Intercept (degrees)	Slope (degrees/cm)	Wavelength (cm)	Total Velocity (km/s)
3.2	119	0.65	554	17.7
12.6	90	2.1	171	21.6
25.1	83	4.0	90	22.6
50	102	9.2	39	19.7
100	117	19.7	18	18.3

Table 4. Curve fit coefficients, wavelength, and velocity found from the phase change over space for different excitation (SPT-100).

	Argon	Krypton	Xenon
Slope (degrees/cm)	4.6	6.2	9.2
θ (degrees)	6.0	4.9	6.0
V_{tot} (km/s)	38.8	29.0	19.6
V_{flow} (km/s)	35	27	18
V_{iaw} (km/s)	3.7	2.3	1.9
Te+3Ti (eV)	5.7	4.6	4.9

Table 5. Parameters found from spatial characterization of wave propagation (MAI Thruster).

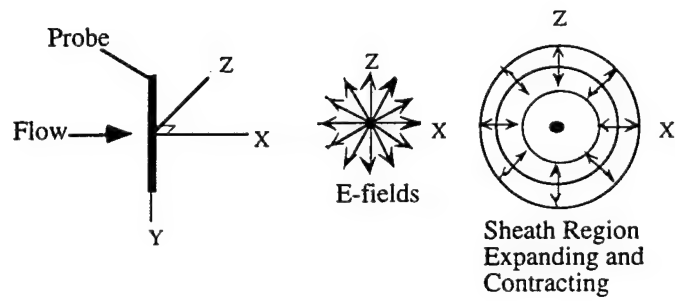


Figure 1. Coordinate system for discussion of propagation.

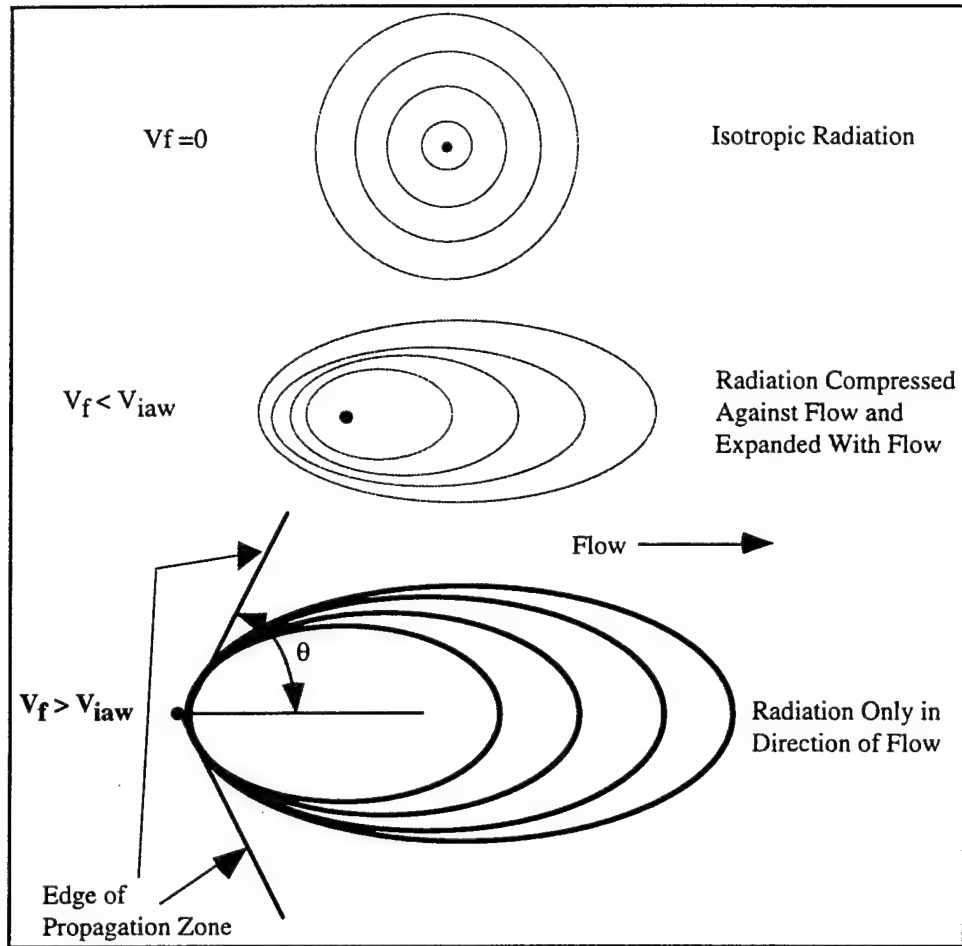


Figure 2. Qualitative comparison of electrostatic propagation in a flowing plasma for three levels of plasma flow velocity relative to the propagation velocity.

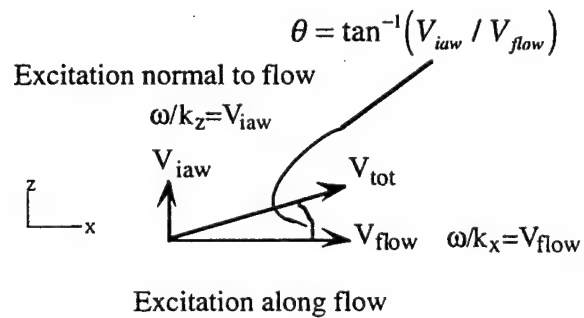


Figure 3. Velocity vector for excitation orthogonal to flow.

$$\begin{array}{c}
 \omega/k_z=0 \\
 \begin{array}{c} \xrightarrow{V_{\text{flow}}} \xrightarrow{V_{\text{iaw}}} \\ \xrightarrow{V_{\text{tot}}} \end{array} \\
 \omega/k_x = V_{\text{flow}} + V_{\text{iaw}} \\
 \downarrow \\
 \lambda = 2\pi(V_{\text{flow}} + V_{\text{iaw}}) / \omega
 \end{array}$$

Figure 4. Velocity vector for excitation parallel to flow.

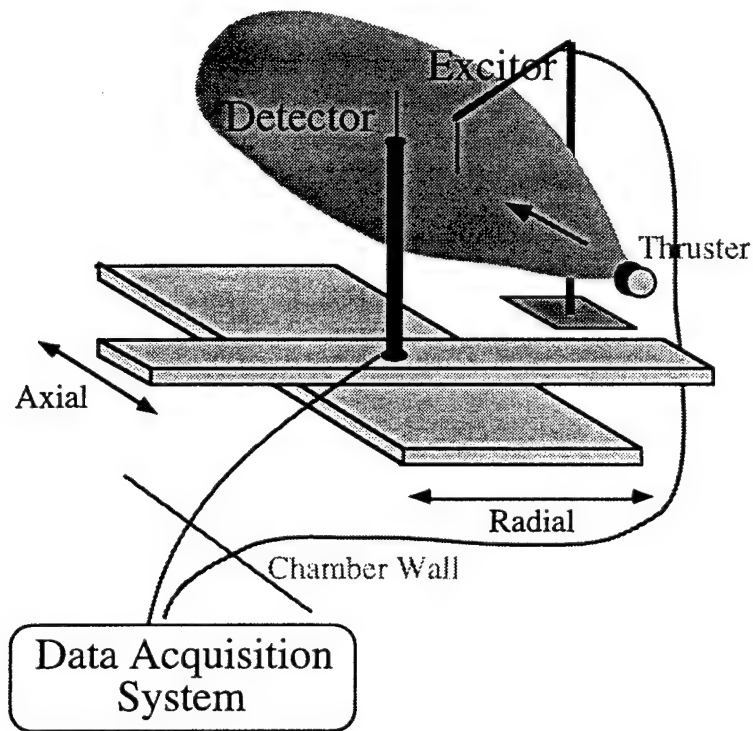


Figure 5. Schematic of probe system for detailed characterization of propagation characteristics.

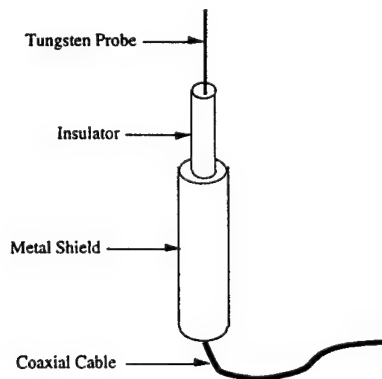


Figure 6. Schematic of probe assembly.

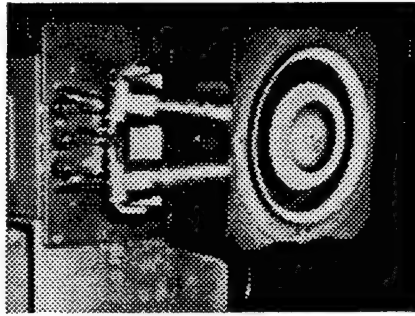


Figure 7. Photograph of the Fakel SPT-100.

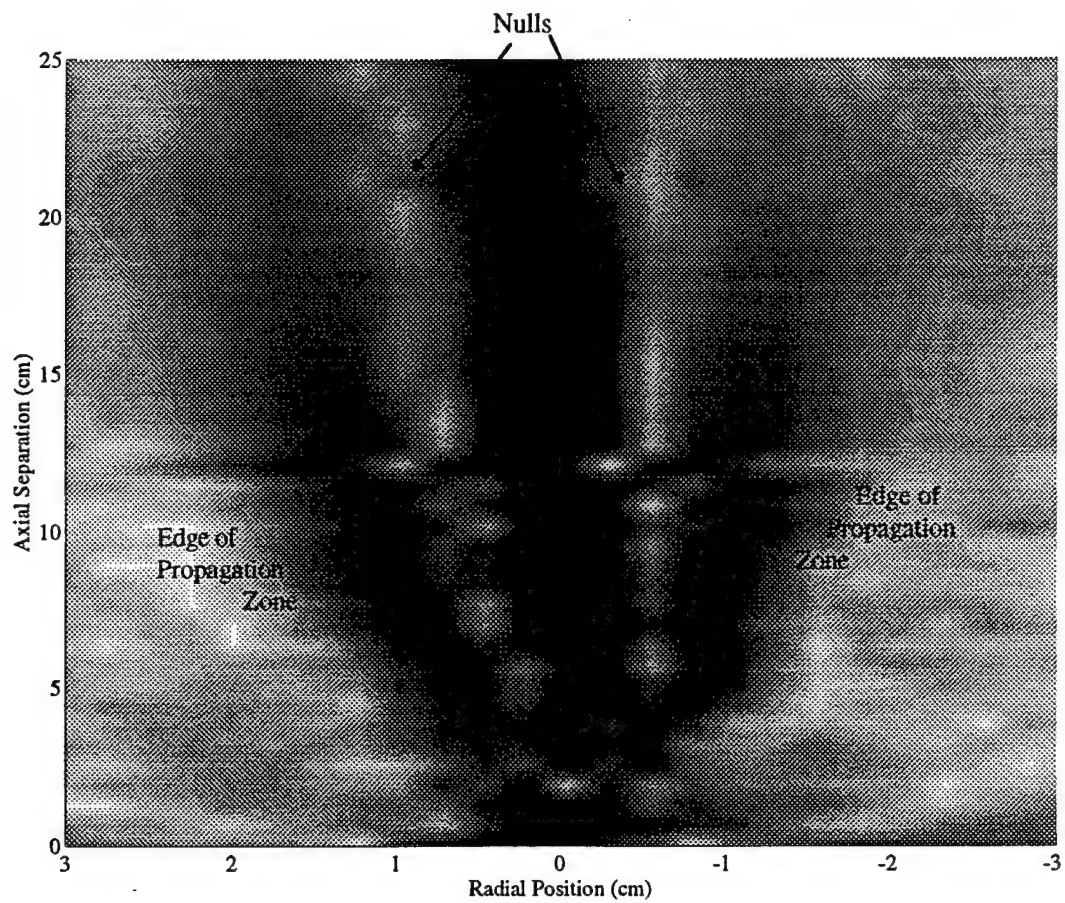


Figure 8. Amplitude variation of an ion acoustic wave (top view).

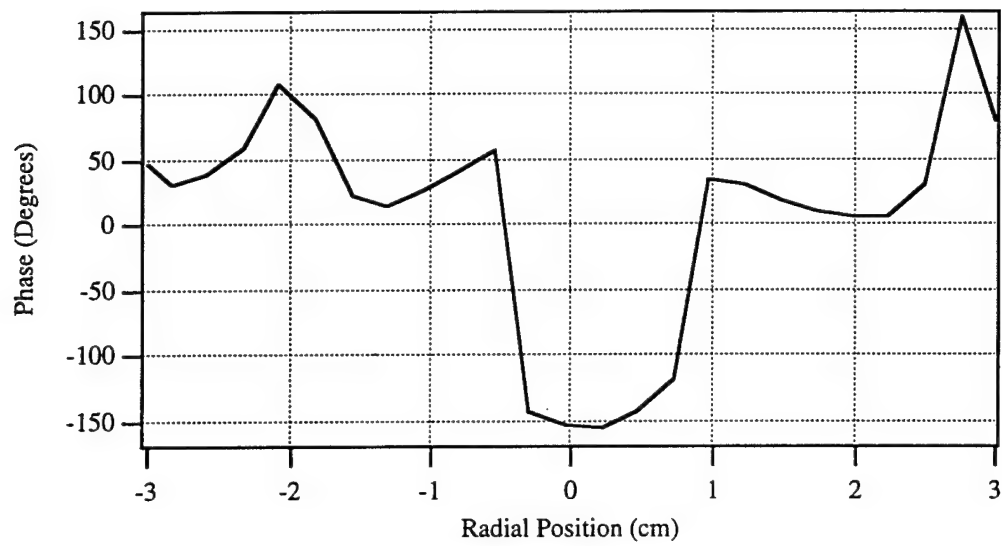


Figure 9. Radial phase variation of an ion acoustic wave in the MAI thruster plume (0.5 m downstream, 10 cm probe separation).

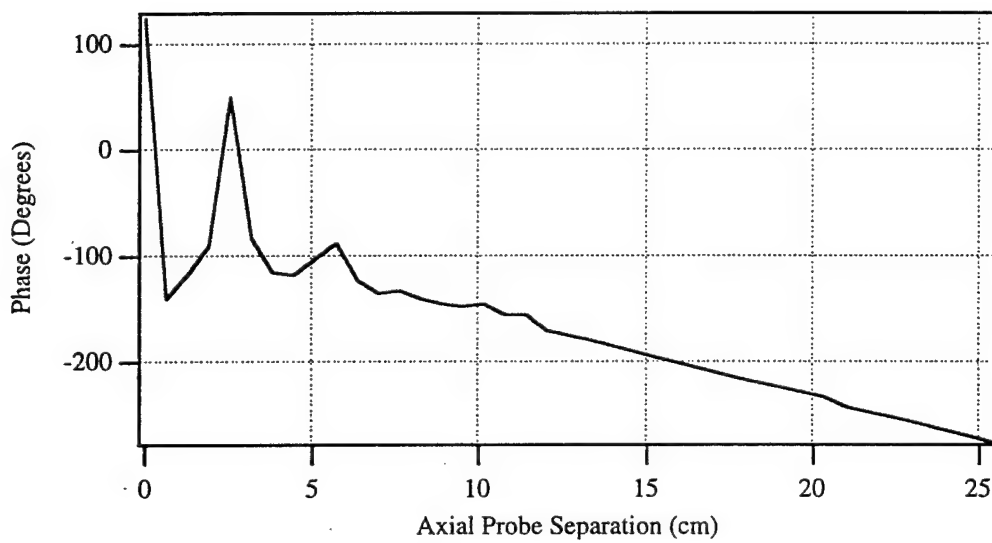


Figure 10. Axial phase variation of an ion acoustic wave in the MAI thruster plume.

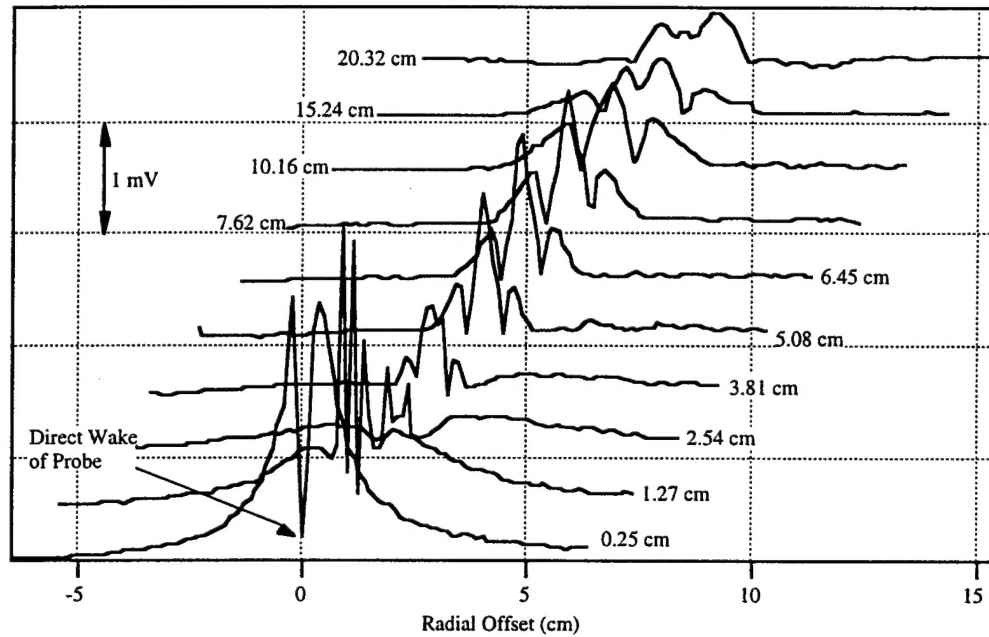


Figure 11. Radial profiles in axial planes for Probe 5 (large) in Experiment 2 with the SPT-100.

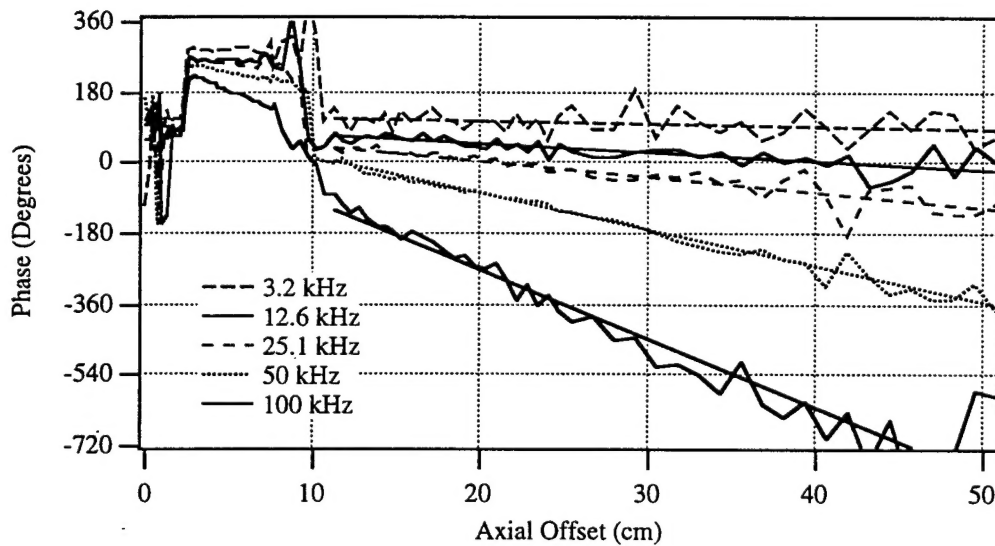


Figure 12. Experimental phase variation and the linear fit plotted with increasing axial separation for different excitation frequencies.

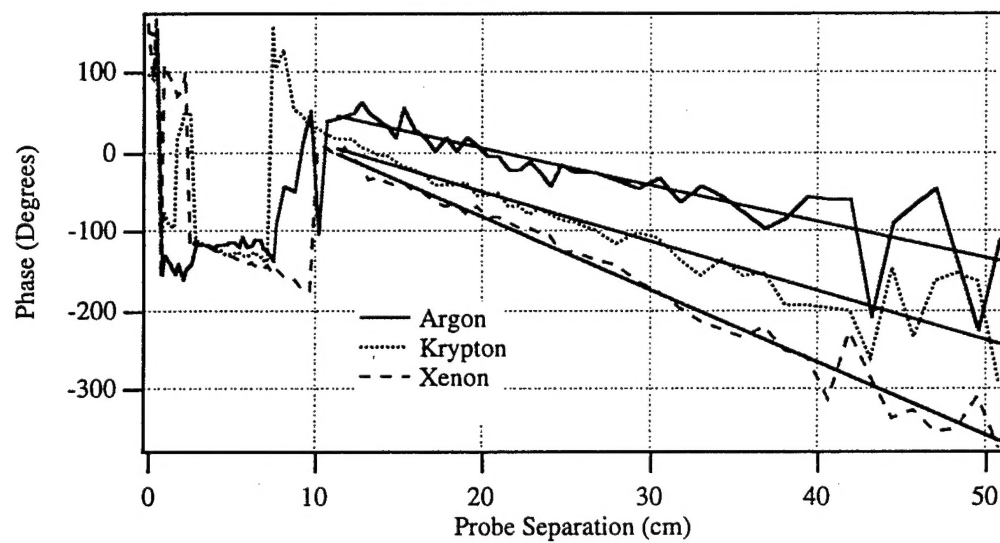


Figure 13. Ion acoustic wave phase progression at 50 kHz (argon, krypton, and xenon).

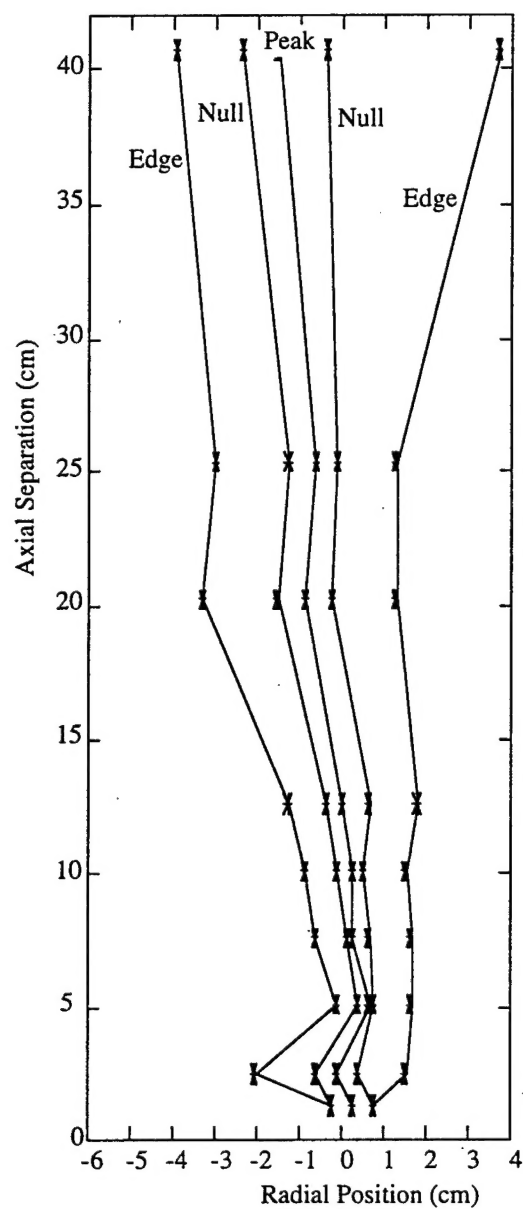


Figure 14. Contour of ion acoustic wave amplitude (xenon).

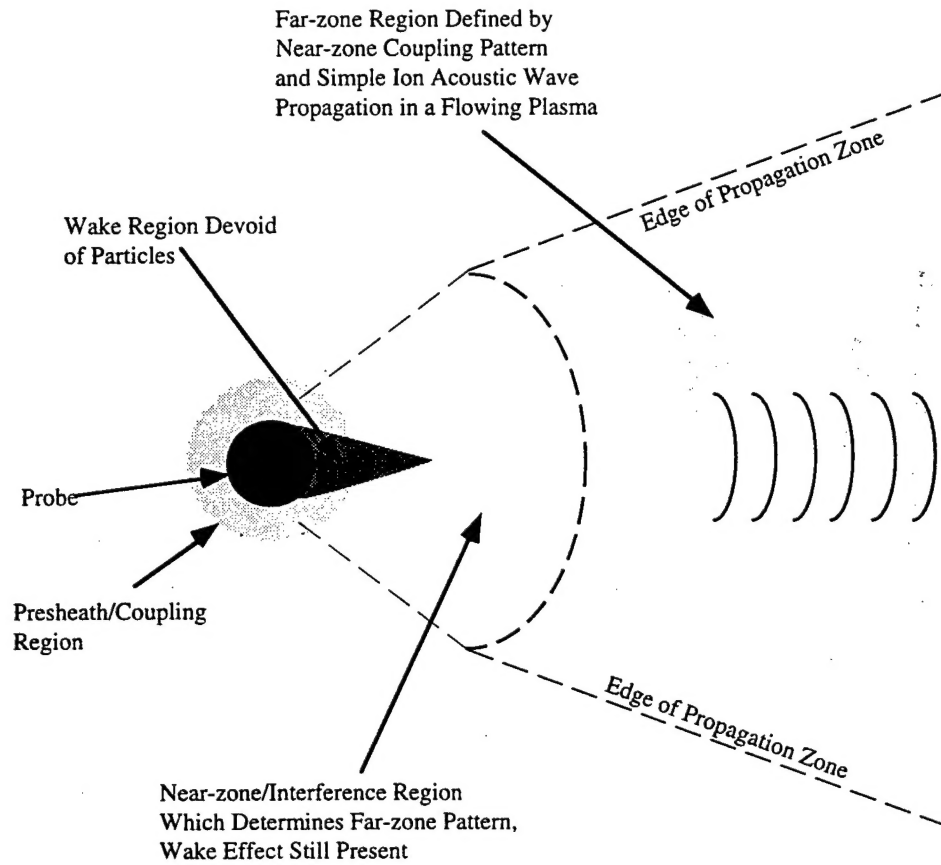


Figure 15. Schematic of excitation and propagation regions.